

JAERI - M
88-029

JAPANESE CONTRIBUTION TO INTOR WORKSHOP
PHASE IIA, PART 3
GROUP B : OPERATIONAL LIMITS AND CONFINEMENT

February 1988

Toshihide TSUNEMATSU, Masafumi AZUMI, Hiroshi MATSUMOTO
Toshiyuki NEMOTO*, Shogo SEKI, Yasuo SHIMOMURA
Masayoshi SUGIHARA, Norio SUZUKI, Tomonori TAKIZUKA
and Shinji TOKUDA

日 本 原 子 力 研 究 所
Japan Atomic Energy Research Institute

JAERI-Mレポートは、日本原子力研究所が不定期に公刊している研究報告書です。
入手の問合わせは、日本原子力研究所技術情報部情報資料課（〒319-11茨城県那珂郡東海村）あて、お申しこしください。なお、このほかに財団法人原子力弘済会資料センター（〒319-11 茨城県那珂郡東海村日本原子力研究所内）で複写による実費頒布をおこなっております。

JAERI-M reports are issued irregularly.

Inquiries about availability of the reports should be addressed to Information Division
Department of Technical Information, Japan Atomic Energy Research Institute, Tokai-
mura, Naka-gun, Ibaraki-ken 319-11, Japan.

©Japan Atomic Energy Research Institute, 1988

編集兼発行 日本原子力研究所
印刷 機高野高速印刷

Japanese Contribution to INTOR Workshop
Phase IIA, Part 3
Group B : Operational Limits and Confinement

Toshihide TSUNEMATSU, Masafumi AZUMI⁺, Hiroshi MATSUMOTO
Toshiyuki NEMOTO^{*}, Shogo SEKI⁺, Yasuo SHIMOMURA⁺
Masayoshi SUGIHARA⁺, Norio SUZUKI, Tomonori TAKIZUKA
and Shinji TOKUDA

Department of Thermonuclear Fusion Research
Naka Fusion Research Establishment
Japan Atomic Energy Research Institute
Naka-machi, Naka-gun, Ibaraki-ken

(Received January 29, 1988)

This report summarizes the data base on the confinement and the beta limit proposed by Japanese delegation to the INTOR workshop Phase IIA, Part 3 held from September 1985 to December 1987.

Keywords: INTOR, Tokamak, Fusion Reactor, Confinement, Beta Limit

⁺ Department of Large Tokamak Research

^{*} Kanazawa Computer Service Co. Ltd.

INTORワークショップ・フェーズⅡAパート3報告書
グループB：運転限界と閉込め

日本原子力研究所那珂研究所核融合研究部

常松 俊秀・安積 正史⁺・松本 宏・根本 俊行^{*}
関 省吾⁺・下村 安夫⁺・杉原 正芳⁺・鈴木 紀男
滝塚 知典・徳田 伸二

(1988年1月29日受理)

本報告書は、昭和60年9月から昭和62年12月迄にオーストリーのウィーンで行われた、INTORワークショップ・フェーズⅡA・パート3の作業会に、日本チームが提出した、トカマク・プラズマの閉込めデータをまとめたものである。

那珂研究所：〒311-01 茨城県那珂郡那珂町大字向山801-1

+ 臨界プラズマ研究部

* 金沢コンピュータ・サービス㈱

Contents

1. Confinement Study	1
1.1 Study on H-mode Discharge in JFT-2M Tokamak	1
1.2 FER Scaling (Mirnov-type Scaling)	7
1.3 Optimized-Confinement Scaling	8
2. Ideal MHD Beta Limit	11
2.1 Benchmark Calculation	11
2.2 Second Stability Access	20
2.3 Beta Limit of D-shaped plasma	23
3. Effect of Conducting Wall on Positional Instability of Elongated Plasma	28

目 次

1. 閉込め研究.....	1
1.1 JFT-2MにおけるHモード.....	1
1.2 FER比例則（ミルノフ型比例則）.....	7
1.3 最適閉込め比例則.....	8
2. 磁気流体的ベータ値限界.....	11
2.1 ベンチマーク計算.....	11
2.2 第2安定領域の利用.....	20
2.3 D型プラズマのベータ値限界.....	23
3. 楕円断面プラズマの位置下安定性.....	28

1. Confinement Study

1.1 Study on H-mode Discharge in JFT-2M Tokamak

1.1.1 Introduction

The JFT-2M tokamak has been operated by using a single-null and a double-null open divertor as well as a limiter. For various types of operations, high confinement regime (H-mode regime) is observed in NB (or ICRF)-heated discharges. The transition to the H-mode discharge, characterized by the decrease in H_α/D_α emission and the increase in the stored energy and density in time, is observed not only in divertor discharges{1} but also in the limiter discharge with a inward shift of plasma position. The transition occurs for both hydrogen and deuterium gases. Among these operations, the single-null divertor discharge shows the H-mode transition with less heating power. In this report, we study the dependence of the energy confinement time in the H-mode regime on the plasma current and the toroidal magnetic field for the case of a single-null divertor discharge. We also study the dependence of the power threshold for the H-transition on the plasma parameters and the plasma position. The results are expected to provide with promising data base for the design of a fusion reactor.

1.1.2 Machine Parameters and Plasma Shape

The machine parameters with heating apparatus are shown in Table.1.1 and the shape of the cross section with the poloidal field coil system is shown in Fig.1.1. The JFT-2M tokamak can be operated in various types of shapes as shown in Fig.1.2; divertor discharges with (1) single-null point and (2) double-null points, the limiter discharges with (3) a noncircular cross section and (4) a circular cross section. Limiters and divertor plates are made of carbon graphite. In this series of experiments, Ti-gettering is employed.

1.1.3 H-mode in a single-null divertor discharge

1.1.3.1 Hydrogen Plasma

Figure 1.3 shows the time evolution of plasma parameters for the hydrogen discharge with H^0 injection of 700KW. From top to bottom, the evolution of plasma current $I_p(KA)$, loop voltage $V_L(V)$, power of neutral beam(MW), line-integrated density $\bar{n}_e L(10^{19}m^{-2})$ with $L=0.77m$, radiation power $P_r(Arb.unit)$, the strength of H_α/D_α emission(Arb. unit), and stored energy($W_s(KJ)$) are shown. The emission of H_α/D_α is observed at the outer midplane of the torus. The stored energy is obtained from

$\Lambda = \beta_p + l_i/2 - 1/2$ in the magnetic fitting. The internal inductance, l_i , is evaluated by the density dependence of Λ at the Ohmic phase. The resultant β_p agrees with that obtained by using the diamagnetic measurement within 10% error. In this discharge, the transition from L-mode to H-mode occurs at $t \sim 715\text{ms}$ (25ms after the start of the neutral beam). In H-mode regime, the density and the stored energy increase in time with the decrease in H_α emission. However, the difference between L- and H- regime is not clear near the transition time in this discharge. At $t \geq 750\text{ms}$, the periodic bursts of the H_α emission appear and the stored energy gradually decreases. Figures 1.4(a) and (b) show the stored energy, W_s and the confinement time τ_E^G as the function of the total power input for $I_p = 240\text{KA}$ and $B_T = 1.2\text{T}$, respectively. The power of the neutral beam is varied by using co-injection system (700KW) and counter-injection system (450KW). These figures show that energy confinement is not degraded by the additional heating power from that in the ohmic discharge. The symbol X denotes the corresponding value in the L-mode regime. The L-mode is observed by the insertion of a limiter near the separatrix.

1.1.3.2 Deuterium Plasma

Figure 1.5 shows the evolution of plasma parameters in D plasma discharge ($I_p = 220\text{KA}$, $B_T = 1.2\text{T}$) with H^0 injection. The neutral beam is injected twice by using counter-injection of 450KW and co-injection of 700KW. The transition to H-mode occurs at $t \sim 610\text{ms}$ and the decrease in H_α/D_α emission without periodic burst is observed. However, the radiation loss increases followed by the saturation of the stored energy. After the saturation, the neutral beam of 700KW is injected and the stored energy begins to increase again. When the radiation power reaches a certain level, the stored energy saturates and then decreases a little followed by the transition to the L-mode regime. Figure 1.6(a) shows the profile of the electron temperature, T_e , measured by ECE (electron cyclotron emission) for the ohmic and the H-mode regimes. The temperature at $0.8a$ ($R - R_0 \sim -25\text{cm}$) is about 0.6KeV in H-mode regime. This value almost agrees with that observed in ASDEX(2). In H-mode regime, the line-averaged density near the edge cord and the plasma center cord, the electron and ion temperatures at the plasma center increase (Fig. 1.6(b) and (c)). However, the increase of the electron temperature seems to be more remarkable at the edge than at the center.

Figures 1.7(a) and (b) show the dependence of the global energy confinement time, τ_E^G , on I_p and B_T , respectively. The confinement time is linearly proportional to I_p and almost independent of B_T ; $\tau_E^G \sim 0.15 I_p (\text{MA})$ sec for these cases. The incremental energy confinement time, $\tau_{inc} = dW/dP$, depends on both I_p and B_T , and $\tau_{inc} \sim 0.115 I_p (\text{MA}) / \sqrt{B_T (\text{T})}$ (sec). This incremental energy confinement time is estimated for the case $P_{total} < 1 \text{ MW}$. The time, τ_{OH}^P , denotes the maximum energy confinement time in the ohmic discharge with respect to the density. The maximum confinement time, τ_{OH}^P , is linearly proportional to B_T and independent of I_p . The result shows that τ_E^G at minimum q_s (the safety factor near the plasma surface) is almost the same as τ_{OH}^P .

1.1.4 Power Threshold for the Transition to H-mode

Figure 1.8 shows the increment of the stored energy as the function of the neutral beam power for $I_p = 220 \text{ kA}$, $B_T = 1.2$ and $\bar{n}_e \sim 2 \times 10^{19} \text{ m}^{-3}$. The plasma current is oriented to the same direction as the toroidal magnetic field. The open and closed circle denote the discharges with upper and lower single-null divertors, respectively. The power threshold for the transition to the H-mode is about half for the case of the lower single-null divertor; $P_{th} \sim 250 \text{ kW}$ for lower single-null divertor and $P_{th} \sim 500 \text{ kW}$ for upper one. The tendency agrees with the experiment in ASDEX[3], but the power threshold is smaller than in ASDEX. Figure 1.9 shows the power threshold as the function of q_{cyl} , $q_{cyl} = 5\kappa a^2 B_T / R I_p$ (κ : ellipticity, a , R : m, B_T : T, I_p : MA). The power threshold is inversely proportional to the plasma current ($100 \text{ kA} < I_p < 300 \text{ kA}$) for a fixed toroidal magnetic field strength ($B_T = 1.2 \text{ T}$) and proportional to the toroidal magnetic field strength ($0.7 \text{ T} < B_T < 1.5 \text{ T}$) for a fixed plasma current ($I_p = 160 \text{ kA}$). Thus, the power threshold increases as q_{cyl} . The distance between the plasma surface and the outer movable limiter, δ_{out} , is $\delta_{out} \sim 10 \text{ cm}$. The triangle (Δ) denotes the power threshold for the case of hydrogen discharge. Figure 1.10 shows the dependence of the power threshold, P_{th} , on δ_{out} . As the outer limiter is moved closely to the plasma surface, the power threshold for the transition to the H-mode gradually increases for $\delta_{out} > 4 \text{ cm}$ and P_{th} becomes suddenly large for $\delta_{out} < 4 \text{ cm}$. As for the clearance of the top region, the H-mode transition is observed for smaller clearance, $\delta_{top} = 1 \text{ cm}$. The result shows that the clearance between the plasma surface and outer limiter is important factor for the H-mode discharge.

1.1.5 Burst of H_α/D_α Emission and Heating Power

The burst of the H_α/D_α emission is observed in the hydrogen plasma (Fig.1.3), where the threshold of the heating power for the H-mode transition is higher ($P_{NB} \geq 0.5MW$) than that in the deuterium plasma ($P_{NB} \geq 0.2MW$) for the case of the upper single-null point. When the burst appears, the stored energy saturates (or decreases) and the increase in the density is moderate. In the deuterium plasma, the burst disappears during the H-mode discharge. Figures 1.11(a) through 1.11(d) show the time evolution of the density (\bar{n}_e), the radiation power (P_{rad}), the stored energy (W_s) and the H_α emission of the hydrogen plasma with single-null divertor configuration for $P_{NB}=0.47MW$, $0.61MW$, $0.74MW$ and $1.21MW$, respectively. The threshold power for the H-mode transition, P_{th} , is about $0.5MW$. Figure 1.11(a) shows the case of $P_{NB} < P_{th}$, which is the L-mode discharge. When P_{NB} exceeds P_{th} , the transition to the H-mode occurs and the burst of H_α emission appears in the hydrogen discharge. As P_{NB} increases, the duration of the reduction of H_α emission becomes longer (Figs.1.11(b) and 1.11(c)), and finally the burst-free H-mode discharge is observed (Fig.1.11(d)). The power for the burst-free H-mode in a hydrogen plasma is more than twice of the threshold power for the H-mode transition. For the deuterium plasma, the threshold power is smaller, $P_{th} \sim 0.2MW$ and the burst of the D_α emission always disappears for $P_{NB} > 1.2P_{th}$ in the divertor configuration with the single-null point. The result suggests the possibility of the suppression of ELM by the heating power.

1.1.6 H-mode Discharge with Pellet Injection {4}

The pellet injector in the JFT-2M tokamak is the ORNL type of gas-propellant single pellet injector. The size of the pellet (design value) is $1.65mm^2 \times 1.65mm^L$ and the speed of the pellet is about $0.7km/s$. The size of the pellet sometimes changes. The pellet is injected before the transition to the H-mode ($t \sim 0.66sec$) in the deuterium plasma as shown in Figs.1.12, 1.13 and 1.14), where the neutral beam with $P_{NB}=0.7MW$ is injected from $t \sim 0.65sec$. In this experiment, three types of H-mode discharges are observed, i.e. Type1 (Fig.1.12), Type2 (Fig.1.13) and Type3 (Fig.1.14). In Type1 discharge, the size of the pellet is smaller than the designed one by chance and the increment of \bar{n}_e at the time of the injection is about $\Delta \bar{n}_e \sim 1.5 \times 10^{19} m^{-3}$. After this time, the density increases linearly in time such as the usual H-mode discharge of the deuterium plasma. For the Type2 and Type3, the increment of \bar{n}_e is about

$\Delta \bar{n}_e \sim 4.5 \times 10^{19} m^{-3}$. In Type2 discharge, the stored energy increases without the burst of D_α emission. The radiation power (0.25MW/div) is smaller than that of Type1 during the increase in the stored energy. For Type2 discharge, the stored energy suddenly decreases with the growth of the fluctuation of the poloidal magnetic field. The safety factor at the 5mm inner surface from the separatrix (which corresponds to about 95% surface), q_ψ , is about 2.5 and the Troyon factor is $g \sim 2.2$ at the peak point of the stored energy. For $g \sim 2.5$, the hard disruption occurs when $q_\psi \sim 2.5$. In Type3 discharge, the increment of \bar{n}_e is the same as that for the Type2, but the stored energy saturates in time when the fluctuation of the magnetic field appears ($t > 0.7s$ in Fig.1.14). After $t \sim 0.7s$, the radiation power increases with burst of D_α emission. Figures 1.15 and 1.16 show the ablation profiles for the cases of Type2 and Type3, respectively. The profile is rather broader for Type3. The broader ablation may affect the current profile near the plasma edge which causes the MHD activity. However the profiles of density and electron temperature are not precisely measured and the difference in two cases has not been clarified. Figure 1.17 shows the global confinement time, $\tau_G = W_s / (P_{total} - dW_s/dt)$, as the function of the density, \bar{n}_e . The confinement time of the H-mode discharge with pellet injection is longer than that of the Ohmic discharge, but the high confinement state is transient.

1.1.7 H-mode Discharge during ICRF Heating {5}

In the JFT-2M tokamak, three sets of high-field-side antennas are used to launch fast waves in a two-ion hybrid resonance heating. A mixture of deuterium and hydrogen gas is used with the ratio of hydrogen to deuterium density of approximately 40%. The plasma is heated via electron Landau damping of the ion-Bernstein wave converted from the fast wave in the thick mode-conversion layer at the center of the plasma. The high energy ion tail created by the heating is very small. The frequency of the launched wave is 16.8 MHz, which is the proton cyclotron frequency at 1.1T of the magnetic field. The toroidal magnetic field is 1.2-1.25T at the plasma center during the heating. The maximum RF power available at the generator is 4.5MW, while the power coupled to the plasma is 2.2MW in the D-shaped limiter discharge and 1.4MW in the single-null divertor configuration because of a small loading impedance

of the antenna.

Figure 1.18 shows an H-mode transition during ICRF heating in the single-null divertor configuration. The plasma parameters are : plasma current $I_p=255\text{kA}$, toroidal magnetic field, $B_T=1.26\text{T}$, surface q-value, $q_s=3.73$, ellipticity, $\kappa=1.43$, and triangularity, $\delta=0.19$. The time evolution of plasma parameters in the L-mode discharge with a similar condition is also shown in the figure, denoted by thin lines. The sudden drop in the H_α/D_α emission is accompanied by increasing the radiation loss, electron density and stored energy. During the H-mode phase, the increase in the stored energy, i.e. the improvement of the energy confinement time, is associated with an improvement in the particle confinement time. These parameters continue to increase until H_α/D_α emission increases suddenly. At the time of transition to the H-mode, the loop voltage initially drops and gradually increases. The time evolution of the ratio of two line-averaged electron densities measured at $R=110\text{cm}$ and $R=124\text{cm}$, shown in the second box from the bottom of Fig.1.18, indicates that the electron density profile broadens in the H-mode discharge.

The dependence of the radiation loss on the electron density is shown in Fig.1.19. The radiation loss increases linearly with the electron density in the H-mode discharges, while it is almost unchanged in the L-mode. Spectroscopic data indicate an accumulation of metallic impurities near the center of the plasma. The central electron temperature stays constant or decline slightly although the intensities of the higher-charge-states metallic impurities increase much more rapidly than those of lower charge states. While 70-80% of the total input power is lost through the radiation at the highest density in the H-mode, the global energy confinement time is close to the one in the Ohmic discharge. This indicates that the energy confinement through the conductive and convective diffusion in the H-mode is much better than in the Ohmic discharge.

Figure 1.20 shows the global energy confinement time as the function of the total heating power. The open and closed circles denote the confinement time in the L-mode and the H-mode, respectively. In the H-mode discharge with $P_{tot} \sim 500\text{kW}$ and $P_{RF} \sim 300\text{kW}$, the plasma is not always stationary and the maximum values are taken in Fig.1.20. In this figure, the cases of upper and lower single-null configurations are shown. For reference the confinement times derived by the Kaye-Goldstone scaling law are shown by crosses. The weak dependence of the energy confinement

time on the power is shown up to $P_{tot}=1.1\text{MW}$. Above this value, it is degraded with power and tends to that in the L-mode discharge. The time evolution of H-mode discharge with $P_{tot} \sim 1.5\text{ MW}$ is shown in Fig.1.21. The H_α/D_α emission at the highest power ($> 1.2\text{MW}$) drops at the transition, but it recovers almost to the level in the L-mode. The electron density does not increase as high a value as that in the H-mode with lower power. The total radiation power shown in Fig.1.22 is considerably lower for $P_{tot}>1.2\text{MW}$ and close to that in the L-mode, while it reaches 80-100% of the total heating power during the H-mode with lower heating power.

1.2 FER Scaling (Mirnov-type Scaling) {6}

The experimental data of the H-mode discharge during additional heating, obtained in medium-size tokamaks, indicate that the global energy confinement time linearly depends on the plasma current, relatively weak on the elongation and in some devices on the heating power, while it is almost independent of the density and the magnetic field strength. The normalized energy confinement time, $\tau_E/(I_p\sqrt{\kappa})$, obtained in ASDEX{7}, PDX{8}, Doublet-III{9,10} and JFT-2M{See 1.1}, are summarized as the function of the total heating power in Fig.1.23, where I_p and κ denote the total plasma current and the ellipticity. The confinement time in the H-mode discharges scatters in a wide range and seems to be continuously connected to the L-mode discharge. For example, in PDX, τ_E is strongly degraded by the heating power. The speculated reasons are; (1) the level of the edge relaxation might increase, (2) the excess gas-fuelling might prevent the transition to the H-mode. In Doublet-III, the normalized confinement time has the tendency that the divertor-discharges show better confinement time than the limiter-discharges, although the former cases overlap the latter ones. The confinement time decreases with the heating power and seems to be saturated in the high power region. Those data are fitted in two ways, $(a+b/P_T)$ or cP_T^{-d} , with $a=0.044$, $b=0.059$, $c=0.097$ and $d=0.35$. Both formulae fit the experimental data within the same accuracy. Assuming that the energy confinement time is saturated in a large heating power, the Mirnov-type scaling law can be derived,

$$\tau_E(s) = 0.155a(m)I_p(MA)\sqrt{\kappa} \quad (1)$$

Here the coefficient, 0.155, is obtained by using the minor radius of

Doublet-III. On the other hand, there is no or weak degradation in the confinement time by the heating power in ASDEX and JFT-2M{See 1.1}. The maximum confinement time in the best H-mode discharges reaches the level of that in an Ohmically heated plasma. The Mirov-type scaling described here is pessimistic one by about factor 3 smaller than ASDEX scaling.

1.3 Optimized-Confinement Scaling {11, 12}

In an optimized H-mode discharge, the global energy confinement time, τ_E , is as long as that of the Ohmically heated plasma, as shown in Doublet-III{9}, JFT-2M{See 1.1} and D-III-D{13} tokamaks. Therefore it is important to understand the scaling law of the Ohmic plasmas with optimized discharges (discharges with a maximum confinement time). The scaling law of the Ohmic plasmas,

$$\tau_E^{OH} \propto n_e^{-1} R^{-2} a^{-1} q_{cyl}^{-1} \kappa^{0.5}, \quad (2)$$

is valid only for relatively lower density. As the plasma density increases, τ_E^{OH} is saturated and gradually decreases as shown in Fig.1.24 except for the cases of the pellet injection. However, a steady-state plasma is not obtained in a pellet-dominated fuelling. Therefore, in a steady state, it is sufficient to obtain the scaling law without pellet injection. The "optimized" energy confinement time is defined as a saturated value of τ_E^{OH} in a high density plasma as shown in Fig.1.24. The critical density, $n_e^c(m^{-3})$, in Fig.1.24 is given by{14},

$$n_e^c = 6.7 \times 10^{19} q_{cyl}^{-1} B_T R^{-1} \sqrt{A_{D,H}} \quad (m^{-3}) \quad (3)$$

The "optimized" energy confinement time is obtained by using eqs.(2) and (3):

$$\tau_E^{OP} = 0.045 R a B_T \sqrt{\kappa} \sqrt{A_{D,H}} \quad (s) \quad (4)$$

The dependence on κ is suggested by the data for relatively low elongation ($\kappa \leq 1.6$) and the validity in the extrapolation to high κ ($\kappa \geq 2$) is not clear. The dependence on size, Ra , is not distinguished from a^2 within present data base. The scaling,

$$\tau_E^{OP} = 0.12 a^2 B_T \sqrt{A_{D,H}} \quad (s) \quad (5)$$

is also possible as more pessimistic one in INTOR-like plasma{11}. In

good H-mode discharges, the energy confinement time is almost independent of the heating power and proportional to the plasma current. In JFT-2M, the energy confinement time in the H-mode approaches to the optimized Ohmic confinement time, and $\tau_E^H \sim \tau_E^{OP}$ with $q_{cyl} \sim 2.2$ in deuterium plasmas. The optimized confinement times for both Ohmic and H-mode plasmas are summarized in Fig.1.25

References

- {1} S. Sengoku and JFT-2M team, J. Nucl. Mat. 145/146 (1986).
- {2} M. Keilhacker et al., "Confinement in ASDEX with neutral beam and RF heating", 13th EPS Budapest 1985.
- {3} "ASDEX Project", IPP Annual Report 1985 (1986).
- {4} Y. Miura et al., "Characteristic of Pellet and Neutral-Beam Injected Single Null Divertor Discharge of the JFT-2M Tokamak", JAERI-M Report 86-148 (1986).
- {5} H. Matsumoto et al., "H-mode phenomena during ICRF heating on JFT-2M," to be published in Nucl. Fusion.
- {6} Japanese Contribution to INTOR-Related Specialists' Meeting on Engineering Test Reactor National Design Concepts (March 23-27, 1987, Vienna).
- {7} A. Staber, et al., Proc. of the 4th Int. Symposium on Heating in Toroidal Plasmas, Rome, (ENEA, Frascati, 1984) Vol.1 (1984).
- {8} R. J. Fnock, et al., ibid., Vol.1 (1984).
- {9} J. C. DeBoo, et al., Nucl. Fusion, 26 (1986) 211.
- {10} A. Kitsunezaki, et al., in Plasma Physics and Controlled Nuclear Fusion Research, (10th Int. Conf., 1984, London) (IAEA, Vienna, 1985) Vol.1 (1985) 57.
- {11} Japanese Contributions to INTOR-Related Specialists' Meeting on Confinement in Tokamaks with Intense Heating, Kyoto (Nov. 21-22, 1986).
- {12} Y. Shimomura, et al., "Empirical Scaling of Energy Confinement Time of L-mode and Optimized Mode and Some Consideration of Reactor Core Plasma in Tokamak," JAERI-M 87-080 (1987).
- {13} J. Luxon, et al., in Plasma Physics and Controlled Nuclear Fusion Research, (11th Int. Conf., 1986, Kyoto).
- {14} S. Sengoku, et al., J. Nuclear Materials 145/147 (1987) 556.

2. Ideal MHD Beta Limit

2.1 Benchmark Calculation

2.1.1 Example of equilibrium

For the stability calculation, we use four kinds of up-and-down symmetric equilibria with $A=4$, $R_0=4m$, $a=1m$, $\kappa=1.6$, $\delta'=0.3$ ($\delta\sim 0.3$), $q_0=1.1$ and $q_s=3.12$ and 3.2 . The profile of the safety factor is obtained by using the algorithm of the nonlinear eigenvalue problem with the following profiles of $dP/d\psi$ and $F(dF/d\psi)$:

$$\frac{dP}{d\psi}(\bar{\psi}) = \beta_l(1 - \bar{\psi}^{j_1})^{j_2}, \quad 0 \leq \bar{\psi} \leq 1 \quad (1)$$

and

$$F \frac{dF}{d\psi}(\bar{\psi}) = R_0^2 \left(\frac{1}{\beta_l} - 1 \right) \mu_0 \frac{dP}{d\psi}(\bar{\psi}) . \quad (2)$$

The vacuum toroidal magnetic field is chosen as $B_{t0}=5.5T$ at the center of the horizontal midplane. By fixing $q(\bar{\psi})$ obtained from the profile (1) and (2) with $\beta_l=0.001$, the pressure is increased in FCT sequence. Table 2.1 shows the parameters (j_1, j_2) and the profile of $P(\bar{\psi})$ in the FCT sequence.

Table 2.1 (j_1, j_2) and pressure profile

	Data 1	Data 2	Data 3	Data 4
(j_1, j_2)	(2.3, 2.0)	(2.3, 2.0)	(1.15, 1.0)	(1.15, 1.0)
q_0	1.1	1.1	1.1	1.1
Calculated q_s	3.12	3.12	3.20	3.20
Pressure	P1	P2	P2	P3

P1 : $P(\bar{\psi}) = P_0(1 - 0.2\bar{\psi} - 2.6\bar{\psi}^2 + 1.8\bar{\psi}^3)$ (a given profile during FCT sequence)

P2 : The marginal pressure, $P(\bar{\psi})^* = - \int_{\psi_0}^0 (dP^*/d\psi) d\psi$, to the ballooning mode.

P3 : The marginal pressure with the form factor, $S_F(\bar{\psi}) = 2 / \{1 + \exp(\bar{\psi}/0.95)^{32}\}$, i.e. $P(\bar{\psi}) = P(\bar{\psi})^* S_F(\bar{\psi})$.

The pressure is increased by using the profiles shown in Table 2.1 with the increment of $\Delta\beta \sim 0.2\%$. In the cases of P2 and P3, the increment of the pressure is given by using the marginal pressure profile of the former step :

$$P^{n-1} \rightarrow (\psi^{n-1}, \beta^{n-1}) \rightarrow (P^{\infty, n-1}, \beta^{\infty, n-1}) \rightarrow P^n, \quad (3)$$

$$P^n(\bar{\psi}) = C_P P^{\infty, n-1}(\bar{\psi}), \quad (4)$$

and

$$C_P = \frac{\beta^{n-1} + \Delta\beta}{\beta^{\infty, n-1}}. \quad (5)$$

This procedure is not a complete optimization with respect to the ballooning mode but the FCT sequence by using the nearly marginal profile of the pressure. The iteration with $C_P=1$ in eq.(4) gives the optimized beta limit for a given q-profile. In Fig.2.1 to Fig.2.4 (which correspond to from Data 1 to Data 4, respectively), subfigures (a)-(j) show the following quantities:

- (a) Contour of equi- ψ . The symbol, *, denotes the position of a null point.
- (b) Contour of equi- J_ϕ .
- (c) Plasma pressure, $P(R, Z=0)$.
- (d) Safety factor, $q(R, Z=0)$.
- (e) Toroidal current density, $J_\phi(R, Z=0)$.
- (f) Safety factor, $q(\bar{\psi})$.
- (g) Pressure gradient $dP/d\psi$. The broken line shows the marginal pressure gradient, $dP^\infty/d\psi$.
- (h) Diamagnetic current density, $FdF/d\psi$.
- (i) Averaged parallel current density.
- (j) Stability diagram in S - α plane. The right side of the curve is a stable region of the ballooning mode. The broken line denotes the marginal line obtained by using $dP^\infty/d\psi$, where S is a global magnetic shear, defined by $S=2V(dq/dV)$ (V : volume surrounded by a magnetic surface), and α is proportional to $dP/d\psi$.

These figures show the quantities at the nearly beta limit due to the ballooning mode. In Table 2.2, the beta limit due to the ballooning mode, β_B , and other quantities are summarized. Here, $\beta_J = 8\pi\bar{P}/\mu_0 I_p(A)^2$ (poloidal beta value), $g_B = \beta_B(\alpha B_{t0}/I_p(MA))$ and $q_{J1} = 5\kappa\alpha^2 B_{t0}/(R_0 I_p(MA))$.

For Data 1 and 2, the shear is weak near the magnetic axis and the numbers of turns for the integration of the ballooning equation should

be increased. In the present calculation, the marginal pressure is obtained by using Mercier criterion when the local interchange modes become unstable. However, it does not affect the beta limit too much because of a small volume of this region.

Table 2.2 Beta limits and other related quantities.

	Data 1	Data 2	Data 3	Data 4
β_B (%)	3.0	4.3	4.1	3.5
β_J	1.2	1.6	1.7	1.5
I_p (MA)	5.5	5.6	5.4	5.3
g_B (%)	3.0	4.2	4.2	3.7
q_{J1}	1.97	1.92	2.02	2.04

2.1.2 Stability Calculation of Low-n Modes

In this section, the ideal MHD stability of the $n=1$ external kink mode is studied for the four cases of equilibria described in section 2.1.1

2.1.2.1 Basic Equation

The stability of the ideal MHD modes is studied by minimizing a Lagrangean {1},

$$L = W_p + W_V - \omega^2 W_K, \quad (6)$$

$$W_p = \frac{1}{2} \int_p d^3x [|Q + (n \cdot \xi)(J_0 \times n)|^2 + \Gamma P_0 |\nabla \cdot \xi|^2 - 2 |n \cdot \xi|^2 (J_0 \times n) \cdot (B_0 \cdot \nabla) n], \quad Q = \nabla \times (\xi \times B_0) \quad (7)$$

$$W_V = \frac{1}{2} \int_V d^3x |\nabla \times A|^2, \quad (8)$$

and

$$W_K = \frac{1}{2} \int_p d^3x \rho_0 |\xi|^2. \quad (9)$$

Here ξ is the displacement of the fluid element, n is the unit vector normal to the equilibrium magnetic surface ($n = \nabla\psi/|\nabla\psi|$), and ρ_0 is the mass density. The quantities with a subscript 0 denote ones in an equilibrium. The perturbation of the vacuum energy in eq.(8) is given by using the vector potential, A , and the boundary conditions for ξ and A are given by {1}

$$n \times A = -(n \cdot \xi) B_0 \quad \text{at plasma surface ,} \quad (10)$$

and

$$n \times A = 0 \quad \text{at conducting shell or infinity.} \quad (11)$$

The potential energy of the plasma motion, eq.(7), can be written in the other form {2},

$$W_p = \frac{1}{2} \int d^3x \left[|Q - \frac{\xi \cdot \nabla P_0}{B_0^2} B_0|^2 - \frac{J_0 \cdot B_0}{B_0^2} \xi \times B_0 \cdot Q + \Gamma P_0 |\nabla \cdot \xi|^2 - 2 \xi \cdot \nabla P_0 \xi \cdot \kappa_0 \right] , \quad (12)$$

where

$$\kappa_0 = \frac{(B_0 \times \nabla (2P_0 + B_0^2)) \times B_0}{2B_0^4} . \quad (13)$$

This form is used in the analysis of the driving mechanism of the instability. The first term in eq.(12) works as the stabilizing term due to the bending and the compression of a magnetic field. The second term and the fourth term are the destabilizing terms due to the current and the pressure gradient and they are called the kink and the ballooning terms, respectively. The weakly unstable MHD modes localize near the rational surface where $q(\psi)$ takes a rational number. For the accurate calculation of the eigenvalue, ω^2 , and the eigenvector, it is necessary to use a flux surface coordinate, (ψ, χ, ϕ) , where χ is the azimuthal coordinate. In the axisymmetric system, the equilibrium quantities are independent of ϕ and the Lagrangean can be written in the form of the single summation with respect to the toroidal mode number, n ,

$$L = \sum_n L_n , \quad (14)$$

and

$$\xi(\psi, \chi, \phi) = \sum_n \xi_n(\psi, \chi) e^{in\phi} . \quad (15)$$

The Fourier-component, $\xi_n(\psi, \chi)$, is written in the contravariant form :

$$\xi_n = R^2 X(\nabla \chi \times \nabla \phi) + R^2 U \nabla \phi \times \nabla \psi + R^2 Y B_0 . \quad (16)$$

2.1.2.2 Numerical Method

The details of the numerical methods of the stability code, ERATO, is described in Ref. [3]. Here, one of the most important procedures in the ERATO-J code is described, i.e. the mapping from the (R, Z, φ) coordinate to the flux coordinate, (ψ, χ, φ) . The azimuthal coordinate, χ , is defined by

$$\chi = \int_0^l \frac{dl}{\sqrt{g} B_p} \text{ with } 2\pi = \oint_{\psi} \frac{dl}{\sqrt{g} B_p}, \quad (17)$$

where \sqrt{g} is the Jacobian of the flux coordinate system. One of the typical coordinate systems is given by

$$\sqrt{g} = \frac{qR^2}{F}. \quad (18)$$

In this coordinate system, the angle between the toroidal and poloidal magnetic field lines is constant on a magnetic surface:

$$\frac{B^{\varphi}}{B^{\chi}} = \frac{\sqrt{g}F}{R^2} = q(\psi), \quad (19)$$

Where B^{φ} and B^{χ} are the contravariant components of the magnetic field. This coordinate system is called "a natural coordinate system".

For the mapping, the trace of the magnetic surface and the numerical derivatives with the high accuracy are inevitable. In the ERATO-J code, the 3rd order or the 5th order spline interpolation is used in the (R, Z) space. The magnetic surface is traced by solving the equation of the magnetic field line:

$$\frac{dR}{dl} = \frac{1}{|\nabla\psi|} \frac{\partial\psi}{\partial Z}, \quad \frac{dZ}{dl} = -\frac{1}{|\nabla\psi|} \frac{\partial\psi}{\partial R}, \quad (20)$$

where dl is the element of the arc length along the magnetic surface. The differential equations (20) are solved by using the 4th order Runge-Kutta method. Along the magnetic surface, the derivatives of $\psi(R, Z)$ are calculated by using the two dimensional spline function.

The mesh accumulation is efficient to describe the ideal MHD modes near the beta limit. In the ERATO-J code, the weight of the mesh accumulation is given by

$$\frac{dW}{ds} = 1 + \sum_i \frac{C_i}{1 + [(s-s_i)/w_i]^2}, \quad (21)$$

where $s = \sqrt{\psi}$. The accumulation point, s_i , is placed near a rational surface, and the weight, C_i , and the width, w_i , are adjusted to be suitable to the structure of the eigenmode. The mesh point in s is obtained by $W_j = W(s_j)$ (W_j : equi-distant mesh in W space).

2.1.2.3 Data set for benchmark calculation

In Table 2.3, the parameters used in the stability analysis are shown.

Table 2.3 Data set for ERATO-J

Parameter	Contents	Value
-	Coordinate	Natural in χ $s = \psi$
N_ψ	mesh numbers in s	101
N_χ	mesh numbers in χ (only upper half plane)	81
C_1	eq. (21)	1.0
W_1	eq. (21)	0.1
s_1	eq. (21)	0.9
ϵ_ω	Convergence of ω^2 in the eigenvalue solver	10^{-4}
n	Toroidal mode number	1
R_{wall}	Position of Conducting Wall	∞

2.1.2.4 Growth rate and beta limit

The stability of the $n=1$ external kink mode is studied for the four classes of equilibria (Data 1 - Data 4) described in section 2.1.1. Figs. 2.5 - 2.7 shows (a) the safety factor as the function of $s = \sqrt{\psi}$, (b) the eigenmode $X(s, \chi=0)$, (c) the eigenmode $U(s, \chi=0)$ and (d) driving terms averaged on a magnetic surface. The symbols A , K and B denote the bending of the magnetic field, the kink term and the ballooning term given in eq. (12), respectively. In Table 2.4, the growth rate and the beta value are summarized for Data 1. The growth rate is normalized by the Alfvén frequency, $\gamma^2 = -\omega^2/\omega_A^2$, where $\omega_A^2 = B_{t0}^2/(\mu_0 \rho_0 R_0^2)$.

Table 2.4 Squared growth rate and β_t for Data 1

β_t (%)	γ^2	β_J	I_p (MA)	q_{J1}	mode
4.80	3.28×10^{-3}	1.77	5.68	1.90	Fig.2.7
4.60	1.92×10^{-3}	1.71	5.66	1.91	
4.40	9.99×10^{-4}	1.65	5.63	1.92	
4.20	4.21×10^{-4}	1.59	5.60	1.92	
4.00	1.16×10^{-4}	1.52	5.58	1.93	Fig.2.6
3.80	1.45×10^{-5}	1.46	5.55	1.94	Fig.2.5

The operator in the ERATO code has a branch of a continuum spectrum in the vicinity of $\omega^2=0$. The eigenfunction of the continuum spectrum has the singularity at a rational surface. Due to the discrete space in $\bar{\psi}$ and χ , the continuum spectrum appears in the unstable side by a numerical reason. Therefore, when the sharp peak in the eignmode, U, localizes with a few meshes, a plasma is considered to be marginally stable. Figs.2.5 (c) and (d) show the structure for a nearly marginal state. The growth rate is $\gamma^2 = -\omega^2/\omega_A^2 = 1.45 \times 10^{-5}$. This result indicates the σ -stability criterion [4] with $\sigma^2 = 1.0 \times 10^{-5}$. For Data 2, 3 and 4, the squared growth rates and the beta values are shown in Tables 2.5, 2.6 and 2.7, respectively. The mode structures near the beta limit are also shown in Figs.2.8 to 2.13. The beta limits due to the ballooning mode and the kink mode are summarized in Table 2.8.

Table 2.5 Growth rate and β_t for Data 2

β_t (%)	γ^2	β_J	I_p (MA)	q_{J1}	mode
4.70	2.78×10^{-4}	1.75	5.66	1.91	Fig.2.9 Fig.2.8
4.50	8.13×10^{-5}	1.69	5.63	1.92	
4.31	2.24×10^{-5}	1.63	5.61	1.92	
4.12	8.91×10^{-6}	1.57	5.59	1.93	

Table 2.6 Growth rate and β_t for Data 3

β_t (%)	γ^2	β_J	I_p (MA)	q_{J1}	mode
3.92	8.06×10^{-4}	1.64	5.33	2.02	Fig.2.11 Fig.2.10
3.73	2.91×10^{-4}	1.57	5.30	2.03	
3.53	4.24×10^{-5}	1.50	5.28	2.04	
3.34	4.06×10^{-6}	1.44	5.25	2.05	

Table 2.7 Growth rate and β_t for Data 4

β_t (%)	γ^2	β_J	I_p (MA)	q_{J1}	mode
3.72	8.06×10^{-4}	1.57	5.38	2.03	Fig.2.13 Fig.2.12
3.53	2.91×10^{-4}	1.50	5.28	2.04	
3.34	4.53×10^{-5}	1.43	5.25	2.05	
3.14	9.45×10^{-6}	1.36	5.23	2.06	

Table 2.8 Beta limit due to ballooning mode and kink mode

Data	β_B (%)	β_B (%)	β_K (%)	β_K (%)
Data 1	3.0	3.0	3.8	3.8
Data 2	4.3	4.2	4.2	4.1
Data 3	4.1	4.2	3.4	3.5
Data 4	3.5	3.7	3.2	3.4

2.1.3 Summary

In this report, we used four classes of equilibria. In Data 1 and Data 2, the shear is weak near the magnetic axis and is strong near the plasma surface. In Data 1, the pressure is increased by fixing the profile which is close to the optimized one near the magnetic axis. The kink limit is greater than the ballooning limit. In Data 2, the pressure is increased by using the marginal pressure at each iteration step. The two limits coincide with each other. In this case the toroidal current density has a finite value at the plasma surface, but the averaged parallel current density is small. For Data 3, the kink limit is smaller than the ballooning limit mainly due to the weaker shear near the plasma surface. By the reduction of the pressure gradient near the plasma surface, two limits become closer. For the data base

assessment in the international collaboration, it is necessary to compare the results in wider range of parameters and to summarize them from the physical point of view.

2.2 Second Stability Access {5, 6}

2.2.1 Optimization of plasma pressure profile

The ideal MHD beta limit due to $n=\infty$ ballooning modes (n : toroidal mode number) is obtained by optimizing the plasma pressure for a given profile of the safety factor, $q(\psi)$. The $n=\infty$ ballooning mode equation {7} with zero growth rate and the Grad-Shafranov equation are solved iteratively to obtain the pressure of a marginally stable state by fixing the safety factor (FCT sequence with optimized pressure). The profile of the safety factor is given by following profile of the toroidal current density at a low beta state:

$$j_\phi = -r \frac{dP}{d\psi} - \frac{1}{\mu_0 r} F \frac{dF}{d\psi} \quad , \quad (22)$$

$$\frac{dP}{d\psi} = \beta_J (1 - \bar{\psi}^{j_1})^{j_2} \quad (\beta_J = 0.1) \quad , \quad (23)$$

and

$$F \frac{dF}{d\psi} = R_0^2 \left(\frac{1}{\beta_J} - 1 \right) \mu_0 \frac{dP}{d\psi} \quad , \quad (24)$$

where $\bar{\psi}$ is the normalized poloidal flux to $0 \leq \bar{\psi} \leq 1$ ($\bar{\psi}=0$ at the magnetic axis and $\bar{\psi}=1$ at the plasma surface, and R_0 denotes the major radius of a plasma center. We choose $\beta_J=0.1$ to determine $q(\psi)$.

2.2.2 Direct access to second stability region

The effect of the magnetic shear on the beta limit is studied by using different profiles of $q(\psi)$. We choose $j_2=1.0$ (case1) and 8.0 (case2) in eq.(23). The parameter j_1 is adjusted so that $q_0=1.2$ and $q_s \sim 3.1$ for $A=3$, $\kappa=1$ and $\delta=0$, where q_s , A , κ and δ are the safety factor at the plasma surface, the aspect ratio, the ellipticity and the triangularity of the cross section, respectively. For the case 1 the shear is moderate in whole region of a plasma (Fig.2.14(a)). The shear is weak near the magnetic axis and strong near the plasma surface for the case 2 (Fig.2.14(b)). We define the flatness of the q profile by $S_w = (q(\bar{\psi}=0.5) - q_0) / (q_s - q_0)$. For the cases 1 and 2 this parameter takes $S_w=0.23$ and 0.05, respectively. A small S_w corresponds to a broad toroidal current profile in a low beta state. Figures 2.15(a) and 2.15(b) show the increase of beta as the function of the iteration in

the equilibrium and the marginal stability calculations of the ballooning modes for the cases 1 and 2, respectively. For the case 1 the beta value saturates at the beta limit, whereas it increases unlimitedly as the iteration for the case 2. The pressure gradient, $dP/d\psi$, at the final stage of the iteration is shown in Fig.2.16(a) and 2.16(b) for the cases 1 and 2, respectively. The broken line denotes the marginal pressure gradient to the ballooning modes. For the case 1, $dP/d\psi$ is almost marginal everywhere in a plasma. However, Fig.2.16(b) indicates that $dP/d\psi$ can be increased unlimitedly or plasma enters the second stability region of the ballooning modes in a low shear region, $S \leq 0.2$, where $S = 2V(dq/dV)/q$ and $V(\bar{\psi})$ is the volume surrounded by a magnetic surface.

The mechanism of the access to the second stability region is shown in Figs.2.17(a) and 2.17(b). Due to the outward shift of the magnetic axis, the negative local shear $\{8\}$, $S_\psi < 0$, appears in the region of negative curvature of the magnetic field line, $\kappa_\psi < 0$, where

$$S_\psi = -\frac{\vec{B} \times \nabla \psi}{|\nabla \psi|^2} \cdot \nabla \times \frac{\vec{B} \times \nabla \psi}{|\nabla \psi|^2}, \quad (25)$$

and

$$\kappa_\psi = \nabla \psi \cdot \frac{\vec{B}}{B} \cdot \nabla \frac{\vec{B}}{B} \quad (26)$$

When the region of $S_\psi < 0$ stays only in the region of $\kappa_\psi < 0$ (Fig.2.17(a)), the pressure gradient reaches the marginal one everywhere in a plasma.

If the negative local shear region extends across the line of $\kappa_\psi = 0$, a plasma locally enters the second stability region on the magnetic surfaces which are included in the region of $S_\psi < 0$. The local negative shear is produced more easily in a low shear region than in a high shear region.

We define a "transition beta value", β_c , as the beta value where the tip of $S_\psi = 0$ reaches the line, $\kappa_\psi = 0$. Above β_c , a plasma has the capability to maintain unlimited pressure. Dependency of β_c on q_0 and κ is shown in Fig.2.18. The parameters j_1 and j_2 in eq.(23) are chosen so that $q_s = 3.1$ and $S_w \sim 0.15$ for $A = 3$. In the shaded region in Fig.2.18, the beta limit is smaller than the transition beta value (no direct access). The broken lines in Fig.2.18 show the boundary flux surface within which a plasma enters the second stability region. The transition beta value is smaller for smaller elongation. As κ increases, the value tends to increase as q_0 (Fig.2.19). In Fig.2.20, κ_ψ and S_ψ are shown as the function of the field line for (a) $\beta_J = 0.1$, $\beta = 0.15\%$ and $\kappa = 1$, (b) $\beta_J = 1.5$, $\beta = 3.16\%$ and $\kappa = 1$, (c) $\beta_J = 0.1$, $\beta = 0.36\%$, $\kappa = 1.6$ and $\delta = 0.3$, (d) $\beta_J = 1.4$, $\beta = 7.4\%$, $\kappa = 1.6$ and $\delta = 0.3$, respectively.

The length of the field line, $l=0$ and $l=1$ correspond to the outside and inside of the torus. In a D-shaped plasma, the local shear is modulated along the field line even in a low beta plasma and it takes the maximum value near the top of D, while it takes the maximum value inside of the torus in a circular cross section. Then the larger shift of the magnetic axis is required to enter the second stability region in a D-shaped plasma. In Fig.2.21, the example of the equilibrium in the second stability region is shown. Figs.2.21(a) to 2.21(c) show the profiles of the plasma pressure, safety factor and toroidal current on the horizontal midplane, respectively. The broken line shows the averaged current density, $\langle \vec{J} \cdot \vec{B} \rangle / \langle B_T \rangle$, which is slightly hollow.

2.2.3 Stability of low- n modes

For the stability analysis of low- n modes the pressure gradient is obtained by using the ballooning mode equation with zero growth rate. The pressure gradient is increased by $C dP_\infty / d\psi$, where $dP_\infty / d\psi$ is the marginal pressure gradient to the $n=\infty$ ballooning instability at each step of equilibrium calculation. In the FCT sequence, the constant, C , is adjusted to be $\Delta\beta=0.2\%$, where $\Delta\beta$ is the increment of the volume-averaged beta value. The profile of the safety factor is chosen as $S_w = (q(\psi=0.5) - q_0) / (q_s - q_0) \sim 0.05$ and $q_s = 3.1$. Above the critical q_0 (Fig.2.19), the direct access to the second stability region is possible. For such an equilibrium the profile of the current parallels to the magnetic field becomes hollow (Fig.2.21) which deteriorates the stability of the external kink modes. Figure 2.22 shows the beta limit of the external kink modes for $\kappa=1.6$ and $\delta=0.3$. The upper and lower lines denote the cases for $a_w/a = 1.2$ and ∞ , where a_w and a are the horizontal radii of a conducting wall and a plasma, respectively. Due to the reduction of the global shear, the beta limit decreases as q_0 for the case of no conducting walls. When the conducting wall is placed close to the plasma surface, $a_w/a=1.2$, $\beta \sim 11\%$ possible for $q_0=1.5$. The beta limit due to the $n=1$ external kink modes is close to Troyon's beta limit, $\beta = g I_p / a B_t \sim 4\%$ for $g=3$, without a conducting wall. The conducting wall placed at $a_w/a=1.2$ increases the beta limit up to $\beta \geq 8\%$ and Troyon's factor g becomes $g=6 \sim 8$. For the case of $\kappa < 1.6$, the factor g takes almost the same value. Above the beta limit, the dominant mode is $m/n=4/1$ for the case of no conducting wall and the mode is localized near the plasma surface (Fig.2.23). When the conducting wall is placed at $a_w/a=1.2$, the dominant component become $m/n=1/1$, which has no rational

surface (Fig.2.24).

When the conducting wall is placed close to the plasma surface, low- n internal modes becomes unstable. Figure 2.25 shows the beta limits of the internal modes as the function of the toroidal mode number. The minimum beta limit is for $n=3$. As n increases the contribution of the driving term changes from the current-driven (kink) term to the pressure-driven (ballooning) one (Fig.2.26-Fig.2.28): (a) q as the function of $\sqrt{\psi}$, (b) radial eigenmode $X(\sqrt{\psi}, \chi=0)$, (c) poloidal eigenmode $U(\sqrt{\psi}, \chi=0)$, and (d) potential energy (K ; kink term, B ; ballooning term). In the low- n region, the dominant mode has low- m (low-poloidal mode number) component which has no rational surface and is localized in a low shear region. This means that the unstable modes are driven by the mode coupling due to the large deformation of the magnetic surfaces. For the enhancement of the beta limit due to the ballooning modes, the low shear region near the magnetic axis is required, whereas the low- m current-driven modes becomes unstable in the low shear region.

2.2.4 Summary

By using the control of current profiles the direct access to the second stability region of the ballooning modes is shown for a plasma with a circular and D-shaped cross section and $q_0 > 1$. The ballooning modes do not limit the beta value but low- n external and internal kink modes determine the beta limit. Further optimization of q -profile is necessary to attain high beta stable state $\beta > 10\%$.

2.3 Beta Limit of D-shaped Plasma

2.3.1 Beta Limit due to the Ballooning Mode {9, 10}

The alternative iteration of the Grad-Shafranov equation and the ballooning equation with zero growth rate gives the marginal pressure derivative in a whole region of the plasma column, from which the beta limit for the "optimized pressure profile" to the ballooning mode is obtained. The FCT algorithm is used to obtain the optimized pressure profile for a fixed profile of the safety factor, $q(\psi)$. The q -profile is given by following profile of the toroidal current density at a low

beta state:

$$J_\varphi = -\mu_0 R \frac{dP}{d\psi} - \frac{1}{R} F \frac{dF}{d\psi}, \quad (27)$$

$$\frac{dP}{d\psi}(\bar{\psi}) = \beta_l (1 - \bar{\psi}^{j_1})^{j_2} \quad (28)$$

and

$$F \frac{dF}{d\psi}(\bar{\psi}) = R_0^2 \left(\frac{1}{\beta_l} - 1 \right) \mu_0 \frac{dP}{d\psi}(\bar{\psi}). \quad (29)$$

The parameters, j_1 and j_2 in eq.(28) determine q_s/q_0 and the flattness of $q(\psi)$ near the magnetic axis. In this study, we take $j_1=1$.

We summarize the dependence of the beta limit on q_0 and q_s , and the geometrical parameters, A , κ and δ . Figures 2.29(a) and (b) show the beta limit as the function of q_s by fixing $q_0=1$ for $\delta=0$ and 0.4, respectively. The aspect ratio, A , is fixed to 3.37 and κ is changed from $\kappa=1$ to 1.6 in these figures. The result shows the enhancement in the beta limit due to the elongation coupled with the triangularity. The calculated data fit the formula,

$$\beta(\%) = \frac{30\kappa^{1.5}}{Aq_s} \left[1 + 0.9(\kappa-1)\delta - 0.6 \frac{\kappa^{0.75}}{q_s} + 14(\kappa-1)(1.85-\kappa) \frac{\delta^{1.5}}{q_s^4} \right]. \quad (30)$$

The range of parameters are $1 \leq q_s \leq 6$, $2 \leq A \leq 6$, $1 \leq \kappa \leq 1.8$, $0 \leq \delta \leq 0.5$ and $q_0=1$. The solid lines in Fig.2.29 denote the values obtained by using the formula (30). The 3rd and the 4th terms of eq.(30) are effective in the lower q_s region, $q_s < 3$. There appears the degradation from the scale in $1/(q_s A)$ for $q_s < 3$ (the 3rd term) and it is improved by δ (the 4th term). The sign of the 4th term changes from positive one to negative one for $\kappa \geq 1.85$. However it should be noticed that the data used in this analysis are limited within $\kappa \leq 1.8$. It should be also noticed that the formula (30) may be applicable for the moderate current profile (i.e. we take $j_1=1$). The flat and hollow current-profiles are excluded. The beta limit can be summarized by using the normalized current, $I_N = I_p(\text{MA})/\alpha(m)B_T(T)$, where the toroidal magnetic field, B_T , is measured at the center of the plasma. The beta limit is roughly proportional to the plasma current, $\beta(\%) = g I_N$. In the low current region (high q_s ; $q_s > q_{sc}$, q_{sc} depends on κ), g takes about 4 it becomes smaller as I_N increases (Fig.2.30). The degradation in g can be improved to some extent by increasing δ . There appears the degradation in g with κ for a given q_s . Figure 2.31 shows β and g as the function of κ for $q_s=3$, $A=4$, $\delta=0.3$ and $j_2=2$. The beta limit tends to be saturated as κ and g -value decreases. As κ increases, the q -profile given by eqs.(28) and (29)

becomes flat near the magnetic axis and the marginal pressure gradient becomes small in the flat- q region. The competition between the flat and steep- q regions causes the saturation in the beta limit. The dependence of the beta limit on q_0 is shown in Fig.2.32. The beta limit is enhanced for larger q_0 and δ , and for smaller q_s/q_0 . This indicates the access to the second region of the stability for the ballooning mode [See 2.2].

2.3.2 Beta Limit due to External Kink Modes [10, 11]

To obtain the beta limit due to the external kink modes, the pressure gradient is increased by $CdP_\infty/d\psi$, where $dP_\infty/d\psi$ is the marginal pressure gradient to the ballooning mode. In the FCT sequence, the constant, C , is adjusted to be $\Delta\beta=0.2\%$, where $\Delta\beta$ is the increment of the volume-averaged (toroidal) beta value. The profile of $q(\psi)$ is given by using eqs.(28) and (29) with $j_1=1$, $\beta_1=0.1$ and $q_0=1$. The stability of the sequence of the FCT equilibria is studied by using the ERATO-J code and the beta limit is obtained from the marginal equilibrium with $\gamma^2 \leq 10^{-5}$, where γ is the growth rate in the ERATO-J code. The characteristic time in γ is $\omega_A^{-1} \sim 1\mu\text{sec}$ for the INTOR parameters. The squared growth rate of $\gamma^2=10^{-5}$ gives the marginal mode structure in this analysis [12, also see 2.1]. Figures 2.33(a) and (b) show the beta limit as the function of q_s for the case without and with a conducting wall, respectively. For the case with a conducting wall, the wall is placed at $a_w/a=1.5$, where a_w is the horizontal minor radius of the wall. The broken lines in Fig.2.33 denote the beta limit due to the ballooning mode described in section 2.3.1. The beta limit due to the $n=1$ external kink mode is smaller than that due to the ballooning mode for the case without a conducting wall. Two limits coincide each other for $a_w/a \leq 1.5$. The sequence of the equilibria used in this analysis is optimized for the ballooning mode but not optimized the external kink mode. The optimization for the external kink mode can be carried out in the q -profile (or the parallel current density to the magnetic field line, $J_\parallel = \vec{J} \cdot \vec{B}/B$ rather than the pressure profile. The external kink mode is stabilized by reducing J_\parallel near the plasma surface and increasing it near the plasma center. This rearrangement in J_\parallel gives a large magnetic shear ($S=(V/q)(dq/dV)$, V : the volume surrounded by a magnetic surface) near the plasma surface, which stabilizes the $n=1$ external kink mode.

There appears a steep degradation in the beta limit near $q_s=\text{integer}$

for $\alpha_w = \infty$. The degradation is usually largest near $q_s = 3$. We study the effect of the current profile by changing j_2 in eqs.(28) and (29). For larger j_2 , the resultant equilibrium has a larger shear near the plasma surface. Figure 2.34 shows the beta limits as the function of q_s for $j_2 = 1.0$ and 1.5, (in this calculation, the equilibrium with high beta tokamak ordering is used and the beta value is normalized to β/ϵ for a circular cross section). For $j_2 = 1.0$, there appears the unstable window below $q_s = 3$. For $j_2 = 1.5$, the beta limit has a finite value, although there remains the degradation in $q_s < 3$. For a given J_\parallel -profile, the shear becomes stronger near the plasma surface and weaker (sometimes negative) near the magnetic axis with the increase in the elongation and triangularity. The degradation for $q_s < 3$ is improved for a large elongation. However the weak shear causes an $m=1$ mode near the magnetic axis [14, See also 2.2].

The beta limit due to the $n=1$ external kink mode is approximately summarized in the Troyon's formula (Fig.2.35),

$$\beta(\%) = (3.2 \pm 0.5) I_p(\text{MA}) / (a(m) B_T(T)) \quad (35)$$

The modulation near the integer q_s is included in the coefficient.

References

- {1} I. B. Bernstein et al., Proc. Roy. Soc. (London) 244 (1958) 17.
- {2} J. M. Greene and J. L. Johnson, Plasma Phys. 10 (1968) 729.
- {3} R. Gruber et al., Comput. Phys. Commum. 21 (1981) 323.
- {4} P. H. Sakanaka and J.P. Goedbloed, Phys. Fluids 17 (1974) 919.
- {5} S. Seki et al., "Beta enhancement of tokamak plasma with nearly circular cross section", submitted to Nucl. Fusion (1986).
- {6} T. Tsunematsu et al., "Second stability access in tokamak plasmas, Part B" in Proc. 11th International Conf. on Plasma Physics and Controlled Nuclear Fusion Research (Kyoto), IAEA-CN-47/E-I-2-1 (1986).
- {7} J. W. Connor, R. J. Hastie, J. B. Taylor, Phys. Rev. Lett. 40 (1978) 396.
- {8} J. M. Greene, M. S. Chance, Nucl. Fusion 21 (1981) 453.
- {9} M. Azumi, et al., "Scaling of Beta Limit in a Tokamak for Infinite-n Ballooning Mode," in proc. of Int. Conf. on Plasma Physics (Lausanne, Switzerland) Vol.1 (1984) 200.
- {10} T. Tuda, et al., "Accessible Beta Value of Takamaks," in Proc. of Int. Conf. on Plasma Physics and Controlled Nuclear Fusion Research 1984 Vol.2 (IAEA, Vienna) (1985) 173.
- {11} T.Tsunematsu, et al., "Stability of External Kink Modes of Tokamaks," in Proc. 12th European Conf. on Controlled Fusion and Plasma Physics, Vol.9F PartII (Budapest, Hungary) (1985) 433.
- {12} T. Tsunematsu, et al., "Data Set for Benchmark Calculation on Ideal MHD Beta Limit of INTOR plasma," JAERI-M 86-172 (1986).
- {13} R.M.O. Galvao, et al., "Global Kink and Ballooning Modes in High Beta Systems and Stability of Toroidal Drift Modes," in Proc. of Int. Conf. on Plasma Physics and Controlled Nuclear Fusion Research 1982, Vol.3 (IAEA, Vienna) (1983) 3.
- {14} T. Tsunematsu, et al., "Stability of Ideal MHD Modes in Low Shear Plasma," in Proc. of Int. Conf. on Plasma Physics, Vol.3 (Kiev, USSR) (1987) 114.

3. Effect on Conducting Wall on Positional Instability of Elongated Plasma

As shown in the sections 1 and 2, an elongated cross section is favourable to enhance both the energy confinement time and the beta limit through the enhancement of the plasma current for a given safety factor at the plasma surface. On the other hand, the positional instability with $n=0$ (n : toroidal mode number) plays important role for the formation of elongated tokamak plasmas. The limit of the elongation for the case of no conducting wall is given by using a rigid model as the function of the aspect ratio, A , {1};

$$\kappa < \kappa_c = 1 + \frac{1}{A^2} \left(\frac{3}{4} \ln 8A - \frac{17}{16} \right) \quad (1)$$

The critical value, κ_c , is about 1.1 for $A=4$. However, the positional instability is suppressed by a conducting wall and κ_c can be increased.

We estimate the critical position of the conducting wall for a given elongation, κ , by using the ideal linearized ideal MHD model. The equilibrium used in this analysis is for $q_0=1$, $q_s \sim 3$, $\beta_J=1.5$ and $A=4$ in up and down symmetry (double-null divertor configuration) where q_0 , q_s and β_J denote the safety factors at the magnetic axis and at the plasma surface and the poloidal beta value, respectively. The toroidal current density is given by

$$J_\phi = -\mu_0 R \frac{dP}{d\psi} - \frac{1}{R} F \frac{dF}{d\psi} \quad (2)$$

$$\frac{dP}{d\psi}(\bar{\psi}) = P_0 \beta_J (1 - \bar{\psi}^{j_1}) \quad (3)$$

and

$$F \frac{dF}{d\psi}(\bar{\psi}) = R_0^2 \left(\frac{1}{\beta_J} - 1 \right) \mu_0 \frac{dP}{d\psi}(\bar{\psi}) \quad (4)$$

The parameters P_0 and j_1 are used to adjust q_0 and q_s to prescribed values. The shape of the cross section is specified by using the functional form:

$$R = R_0 + a \cos(\theta + \delta \sin \theta) \quad (5)$$

and

$$Z = \kappa a \sin \theta \quad (6)$$

where κ , δ and a_p denote the ellipticity, triangularity and the horizontal minor radius. Figure 3.1 shows the equilibrium for $\kappa=2.0$ with $\delta=0.3$: (a) contour of poloidal flux function, (b) contour of toroidal current density, (c) plasma pressure, (d) safety factor and (e) toroidal current on the horizontal midplane.

The analysis with a closed conducting wall at the equi-distant position from the plasma surface shows that $b_w/b_p \sim 1.3$ for $\kappa=2.0$ to suppress the positional instability. The parameter, b_w/b_p , specifies the position of the conducting wall, where b_w and b_p are the radii of the conducting wall and the plasma at the top of the cross section, respectively. The European contribution[2] shows the partial wall is sufficient to stabilize the instability by using the rigid model. In this report, we evaluate the effect of the poloidal cut of the conducting wall by using the shape of the wall shown in Fig.3.2. The shape of the wall is specified by using the parameters, $\rho_w(0)/\rho_p(0)$, $\rho_w(\pi)/\rho_p(\pi)$, b_p and d_w , where $\rho_w(0)$, $\rho_w(\pi)$, $\rho_p(0)$, $\rho_p(\pi)$ and b_p ($b_p = \kappa a_p$, $a_p = (\rho_p(0) + \rho_p(\pi))/2$) denote the outer horizontal radius of the wall of the torus, the inner radius of the wall, the outer radius of the plasma, the inner radius of the plasma measured from the magnetic axis and the radius of the plasma in the vertical direction, respectively, and d_w denotes the width of the cut. The choice of the origin at the magnetic axis is only for the numerical reason in the ERATO-J code. The horizontal radii, a_w and a_p can be used in stead of ρ_w and ρ_p without essential difference. In this analysis, we take $\rho_w(0)/\rho_p(0) = \rho_w(\pi)/\rho_p(\pi) = 2.0$ and d_w is changed. Figure 3.3 shows the flow pattern of the plasma motion projected to the poloidal plane for the case without conducting wall. The Fourier analysis of the eigenmode shows that the dominant modes are $m=\pm 1$ and $|m| \geq 2$ modes are included near the plasma surface. Figure 3.4 shows the case with conducting wall for $d_w/a_p = 2.5$. The large motion at the right shoulder of the cross section in Fig.3.3 is suppressed by the conducting wall. The squared growth rate, γ^2/ω_A^2 , is shown as the function of d_w/a_p for the cases of $\delta=0.1$ and 0.3 in Fig.3.5. The case of the smaller triangularity is more unstable. However, the critical width of the cut is almost the same, i.e. $d_w/a_p \sim 1.9$. The closest distance of the wall from the plasma surface is about 60cm for the INTOR size of plasma ($a_p=1.2\text{m}$, $R=4.9\text{m}$ and $\kappa=2.0$). The critical width of the cut is almost independent of $\rho_w(0)/\rho_p(0)$ for $\rho_w(0)/\rho_p(0) > 1.5$. The result of the preliminary analysis shows the conducting wall placed at the shoulder of the cross section can suppress the positional instability. The result agrees with that shown in the European contribution. The quantitative comparison with the rigid model is not carried out.

Acknowledgement

The authors would like to express their sincere thanks to Drs. S. Mori, K. Tomabechi, M. Tanaka, Y. Yoshikawa, T. Takeda and M. Funahashi for continuous encouragements.

Reference

- {1} J. A. Wesson, Nucl. Fusion 18(1978) 87.
- {2} European Contribution to the Data Base Assessment for the INTOR Workshop, session XIV, Group D (1986).

Table 1.1 Parameters of JFT-2M Tokamak.

JFT-2M TOKAMAK

Tokamak Parameters	
•Major radius R_0	1.31 m
•Minor radius $a \times b$	0.35×0.53 m
•Plasma shape	
Ellipticity	1 - 1.7
Triangularity	0 - 0.7
•Div. configuration	double & single
•Plasma current	550 kA, 1 sec.
•Toroidal field	1.5 T
•Flux swing (Iron core)	2 V.sec
•Limiter (Carbon)	Fixed & Movable
•1-Pellet Injector	
Speed	800 m/sec
Mass	$1.6 \text{ mm} \phi \times 1.6 \text{ mm}$
Heating Apparatus	
•ICU	15 - 38 MHz
•NB	40 kV
•LH	750 MHz
•ECH	60 GHz
•FW	200 MHz
	4.5 MW
	2.0 MW
	0.6 MW
	0.4 MW
	0.1 MW
	Loop Antenna x3
	Co & Ctr
	4 Grille Launcher
	Gyrotron x2

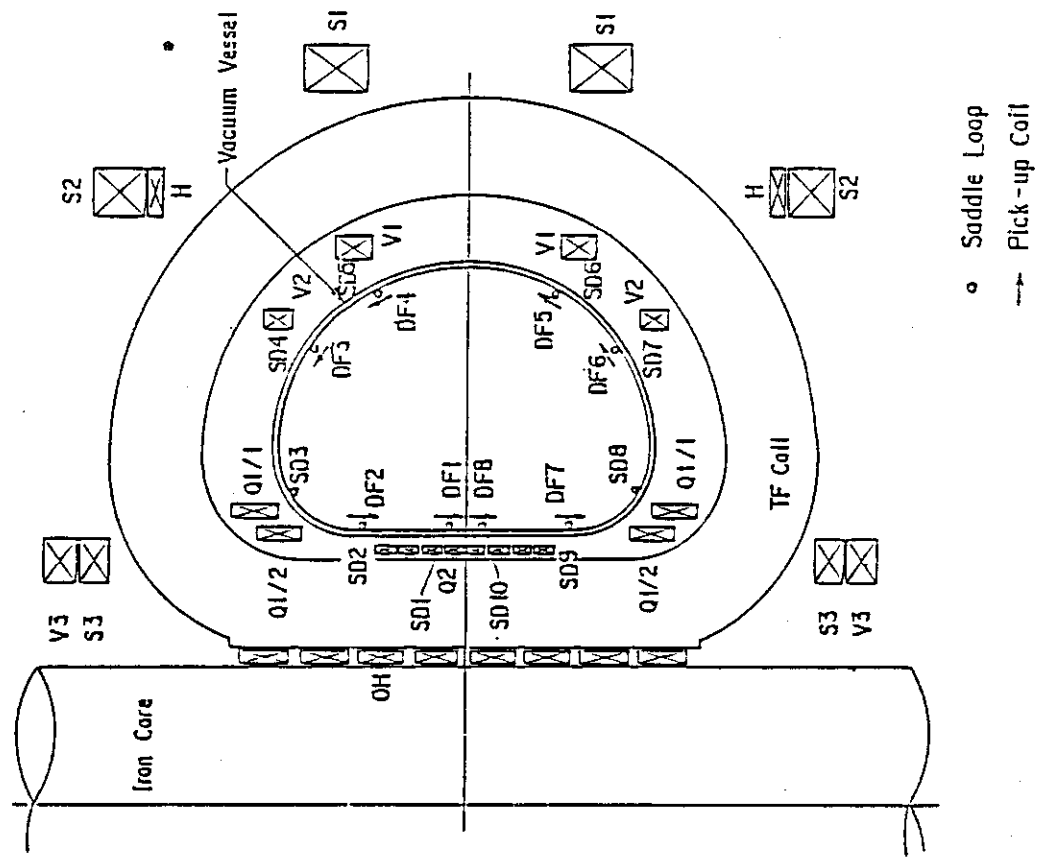
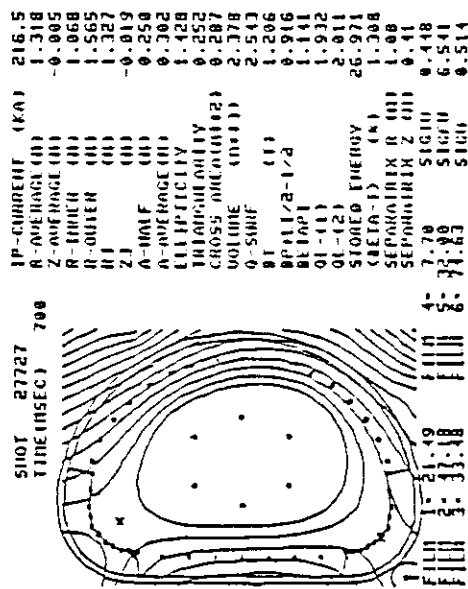
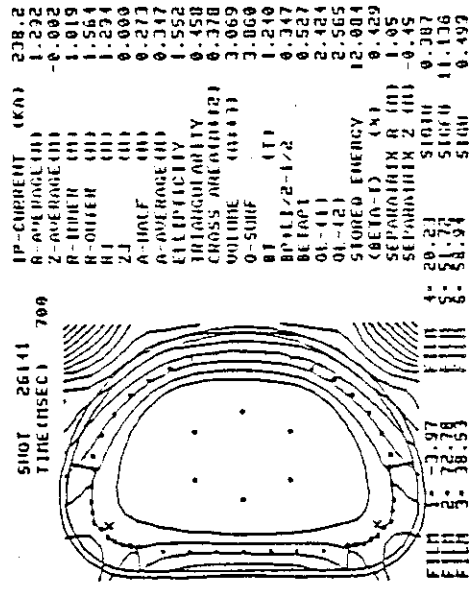


Fig.1.1 Poloidal coils and magnetic probes

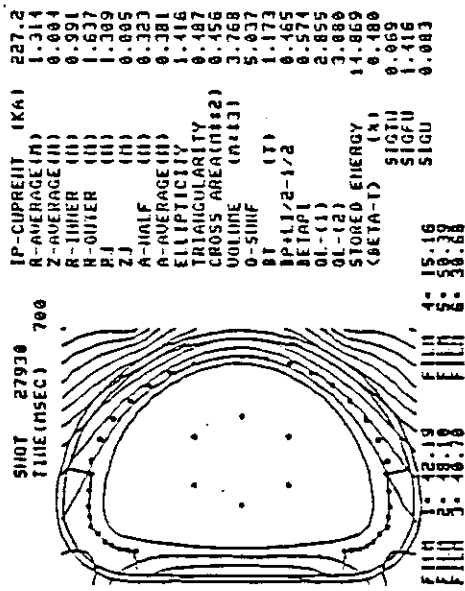
(1) SINGLE HULL DIV.



(2) DOUBLE HULL DIV.



(3) D-SWEE LHA.



(4) CIRCULAR LHA.

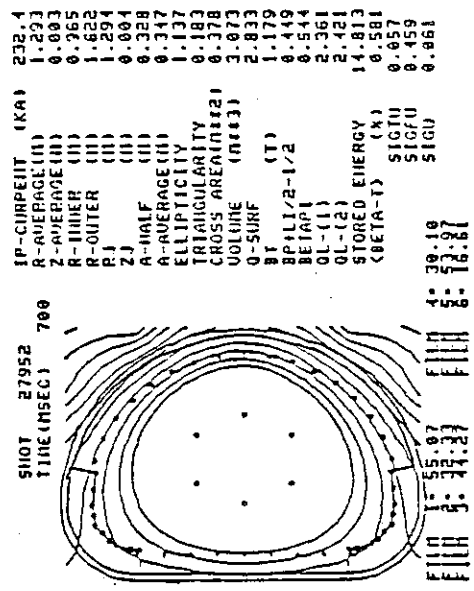


Fig.1.2 Typical plasma shapes obtainable in JFT-2M tokamak.

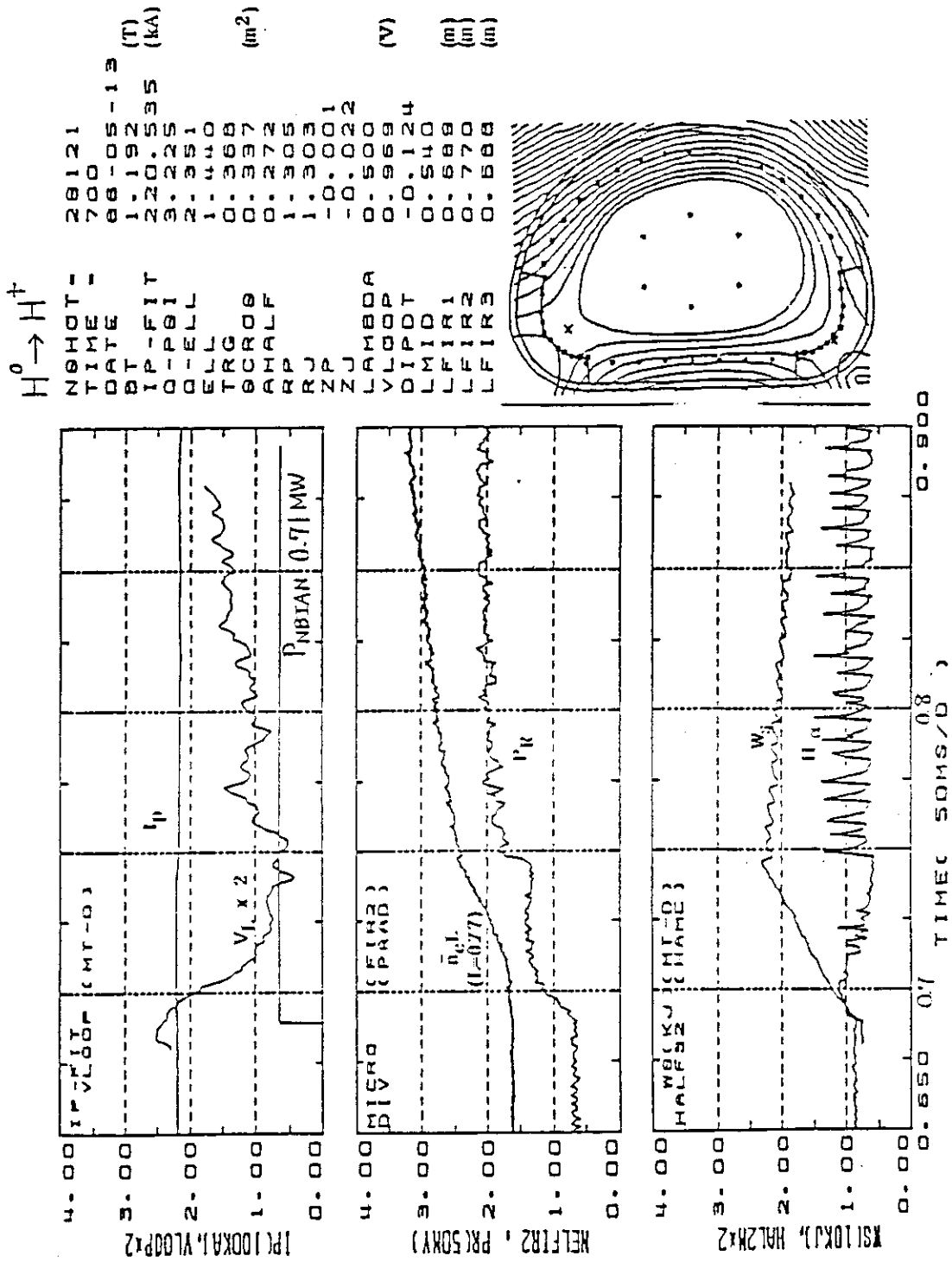


Fig.1.3 Typical H mode with H_0/D_a burst ($H^0 \rightarrow H^+$).

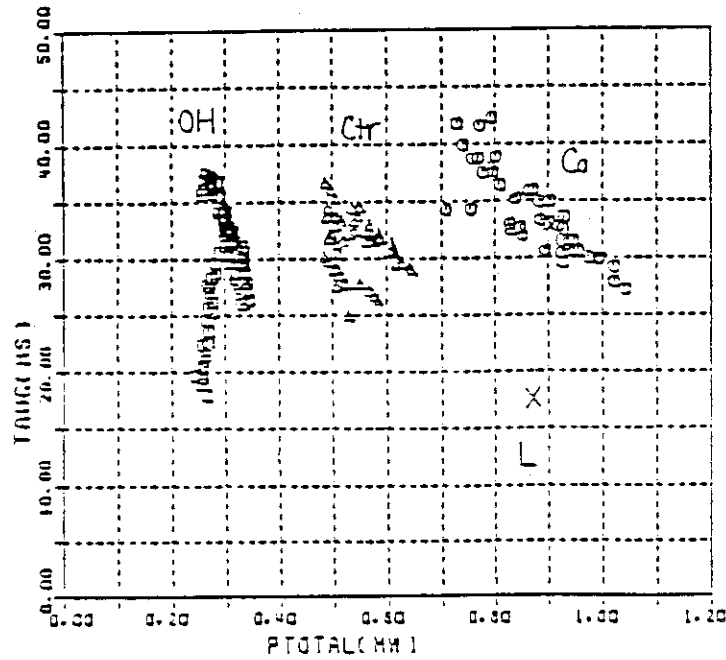
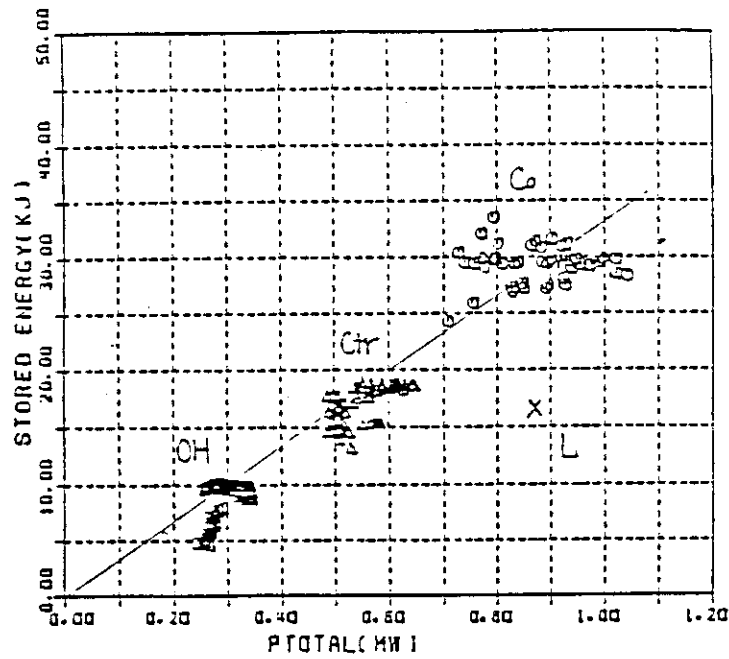


Fig.1.4(a) Stored energy W_s vs. total input power P_T , where

$$P_T = P_{OH} + P_{NB} - dW_s/dt \quad |dW_s/dt| \leq 100 \text{ KW}.$$

(b) Global energy confinement time vs. P_T , where $\tau_E^G \equiv W_s/P_T$.

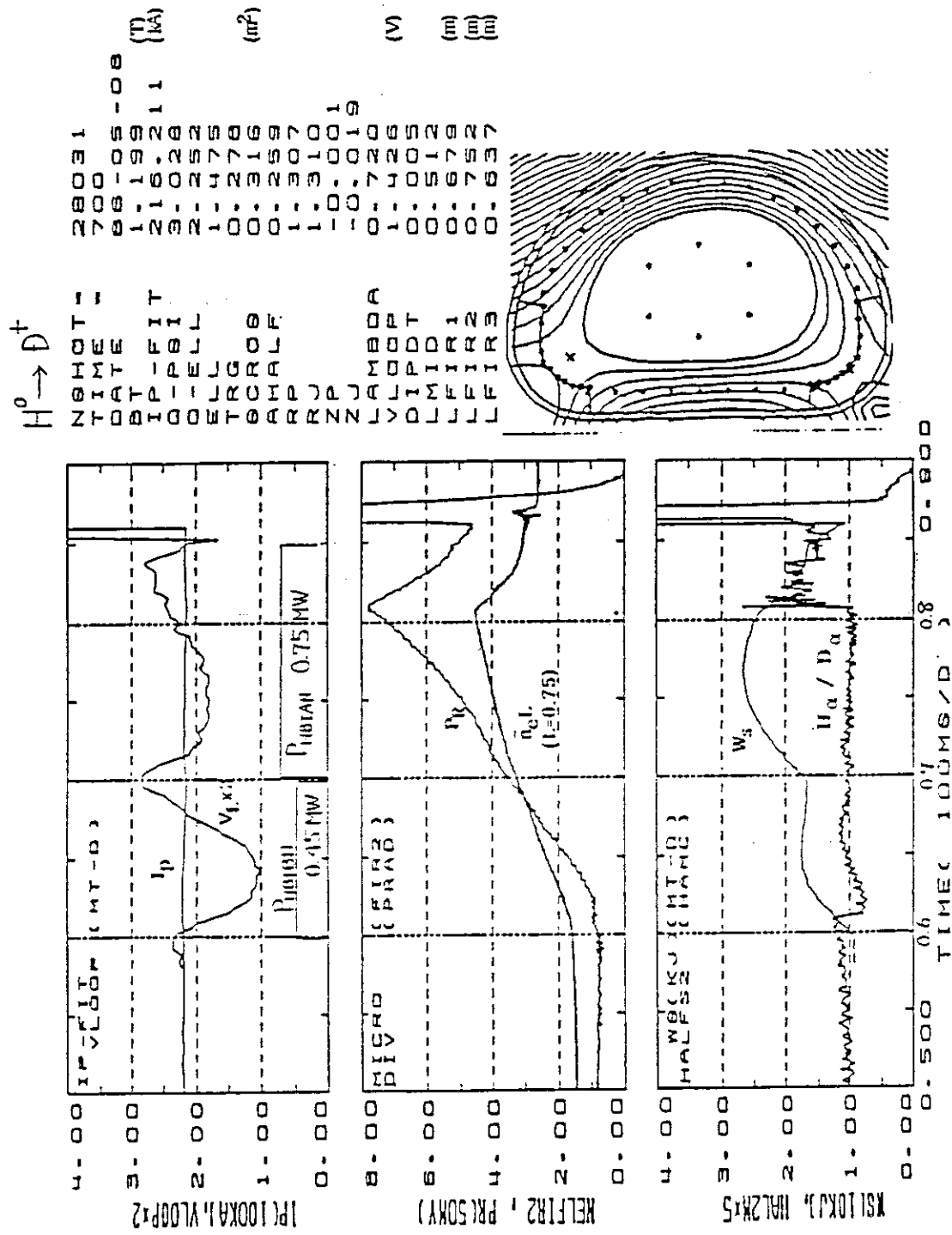


Fig.1.5 Typical H mode without H_a/D_a burst ($H^0 \rightarrow D^+$). Radiation loss with a Bolometer increases with time followed by the H-L transition at a critical P_H level.

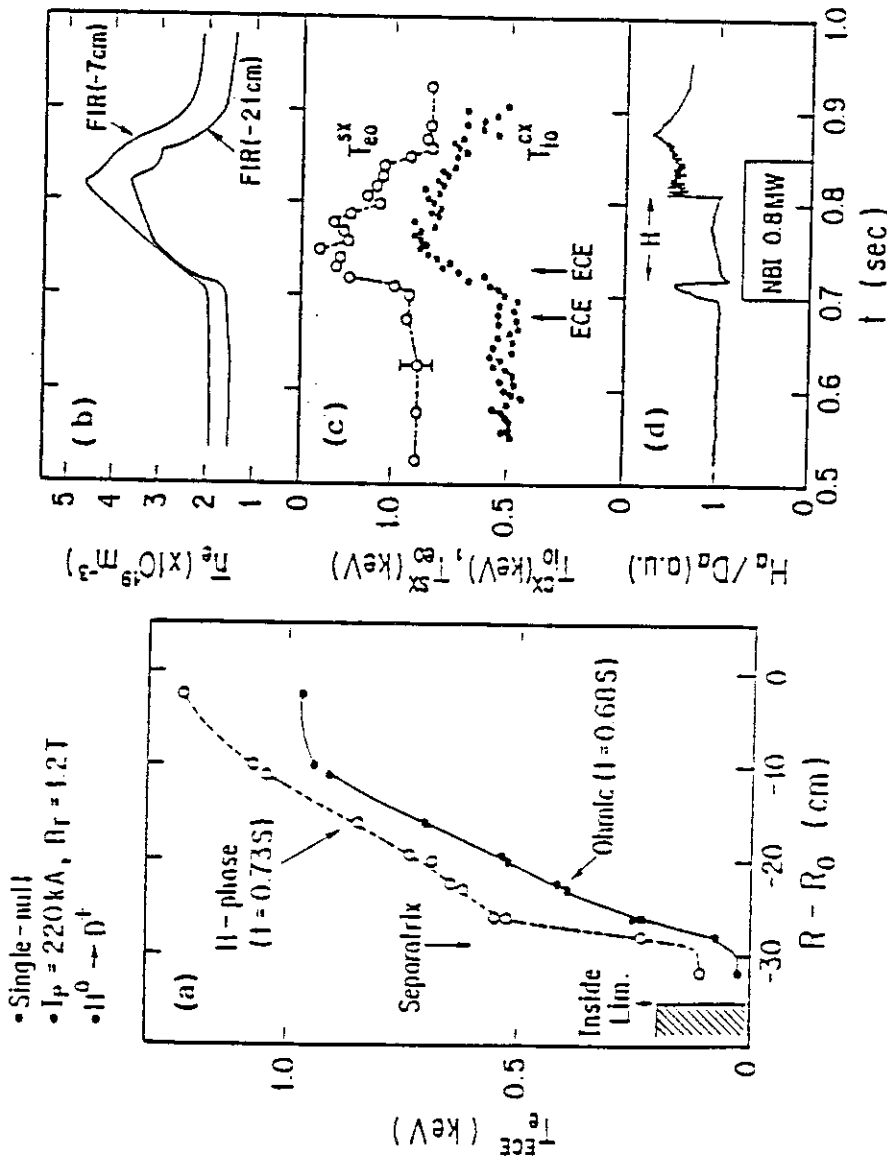


Fig1.6 Typical plasma parameters in the case of H-mode without the burst. (a) electron temperature profile measured by ECE, temperature pedestal is formed in the H-phase. (b) line-averaged density near the central cord and peripheral cord, (c) central T_{e0} obtained by SX and T_{e0}^{CX} , (d) time evolution of H_e/D_e emission and

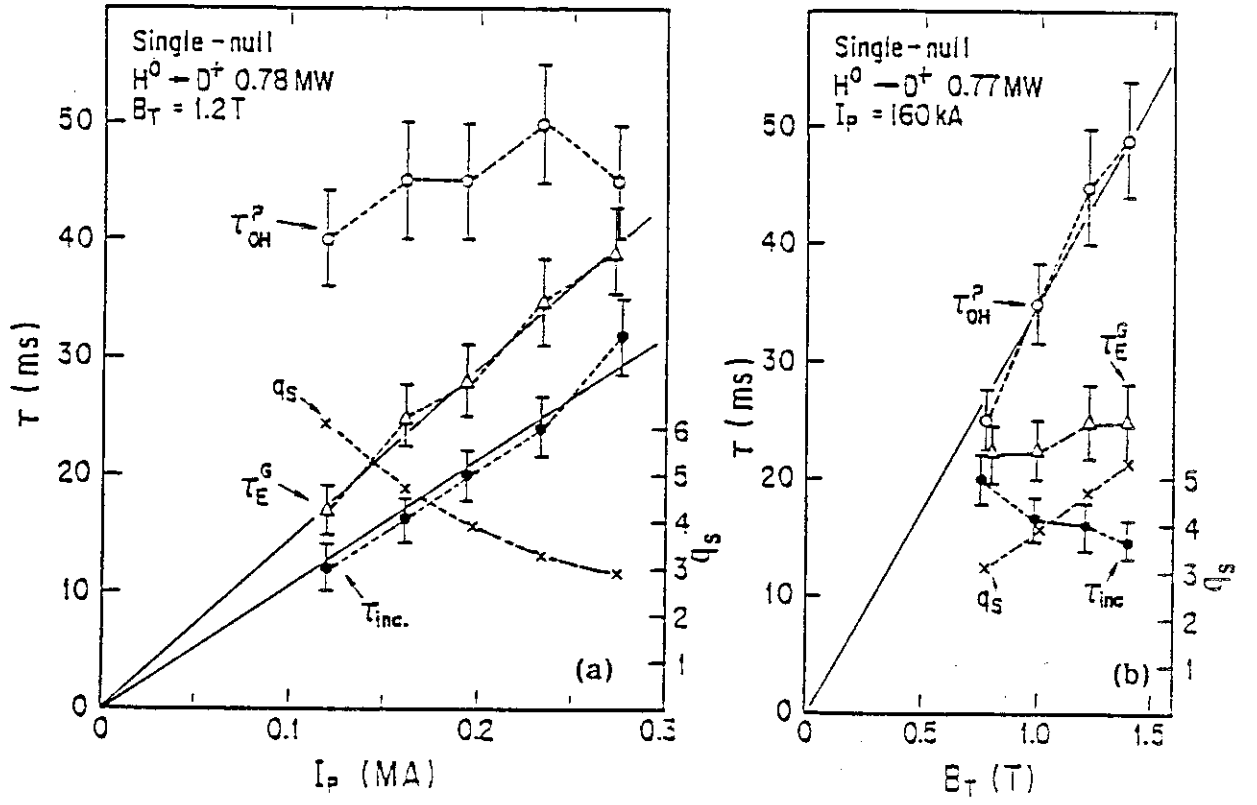


Fig.1. (a) I_p -dependence of global energy confinement time in the H-mode without H_α/D_α burst.

τ_{OH}^p : peak confinement time at OH-phase.

τ_E^G : global energy confinement time near the W_s peak.

$$\tau_E^G \equiv W_s / P_T.$$

τ_{inc} : incremental energy confinement time defined by

$$\tau_{inc} \equiv \Delta W_s / \Delta P_T.$$

(b) B_T -dependence of confinement time.

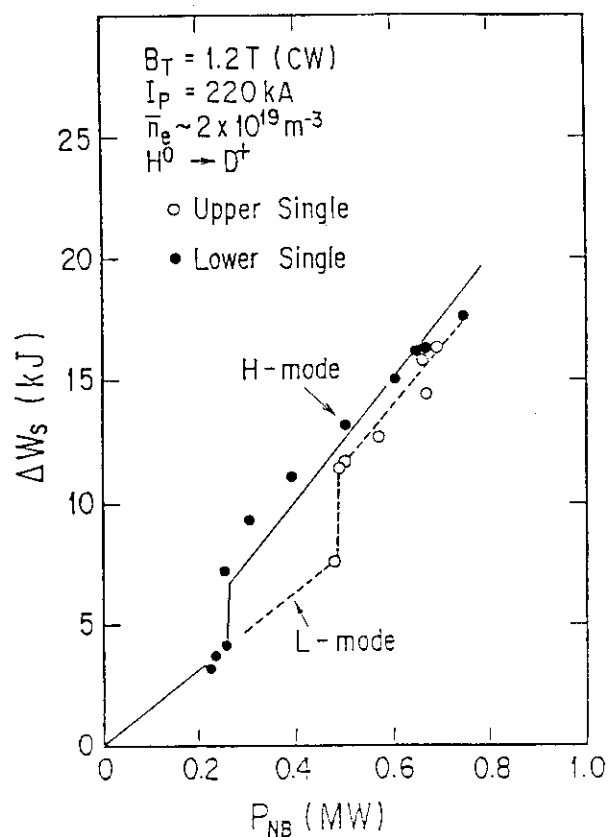


Fig.1.8 Up-down asymmetry of the threshold power P_{th} for the H-transition. ∇B toward the null point affects P_{th} . Minimum P_{th} is about 0.2 MW.

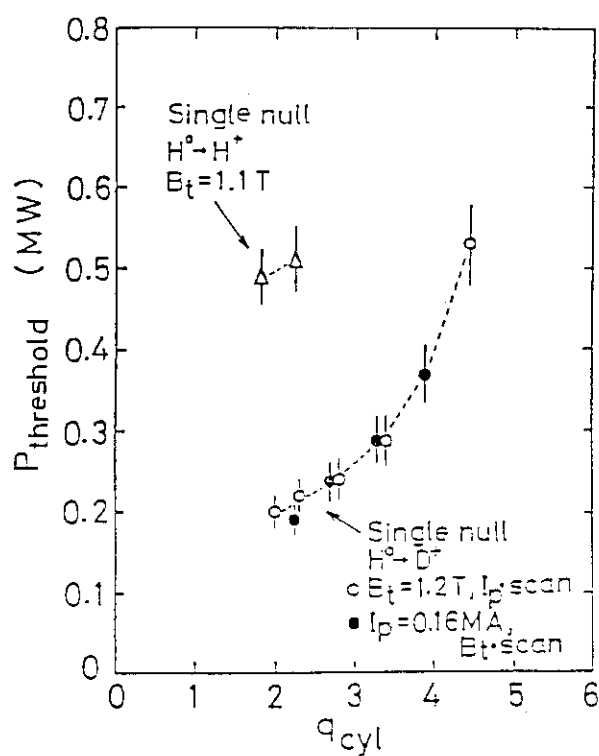


Fig.1.9 P_{th} dependence on q_{cyl} . P_{th} increases as q_{cyl} . P_{th} for $\text{H}^0 \rightarrow \text{H}^+$ case is also plotted (Δ). P_{th} in H_2 is 2 - 3 times larger than one in D_2 .

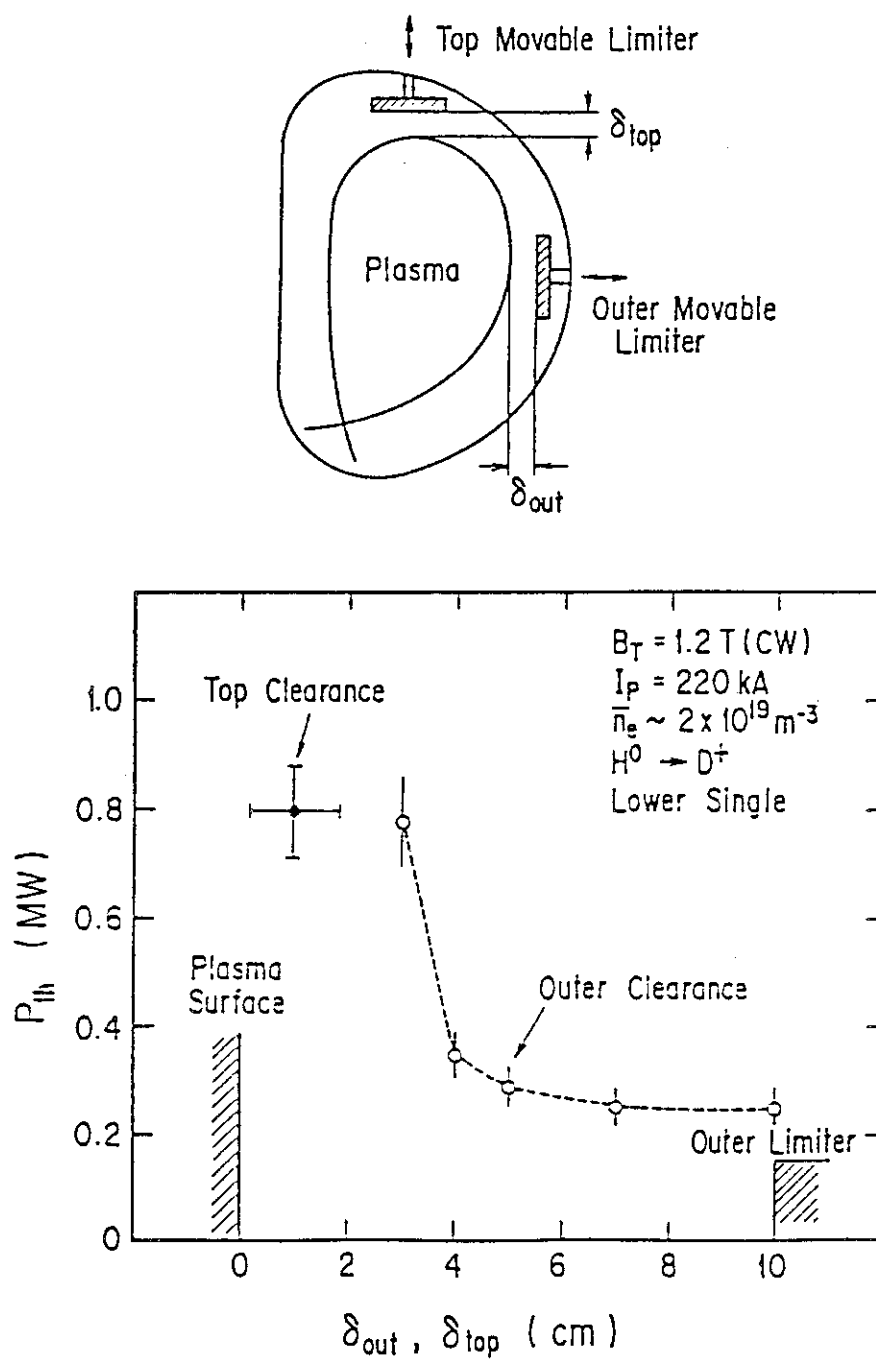


Fig1.10 P_{th} vs. clearance(δ). The closed circle denotes P_{th} for the top clearance.

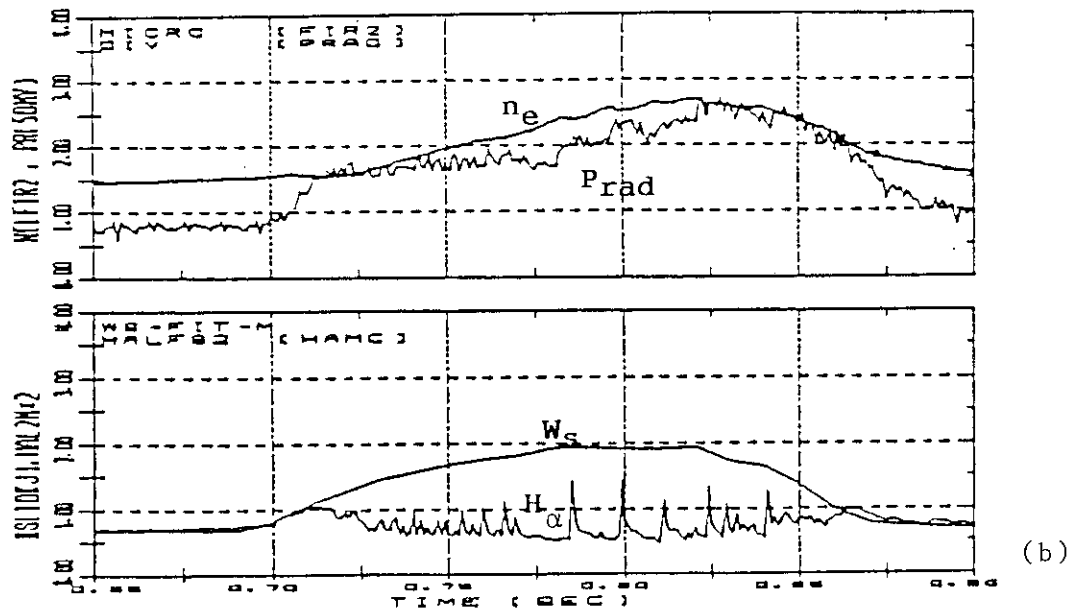
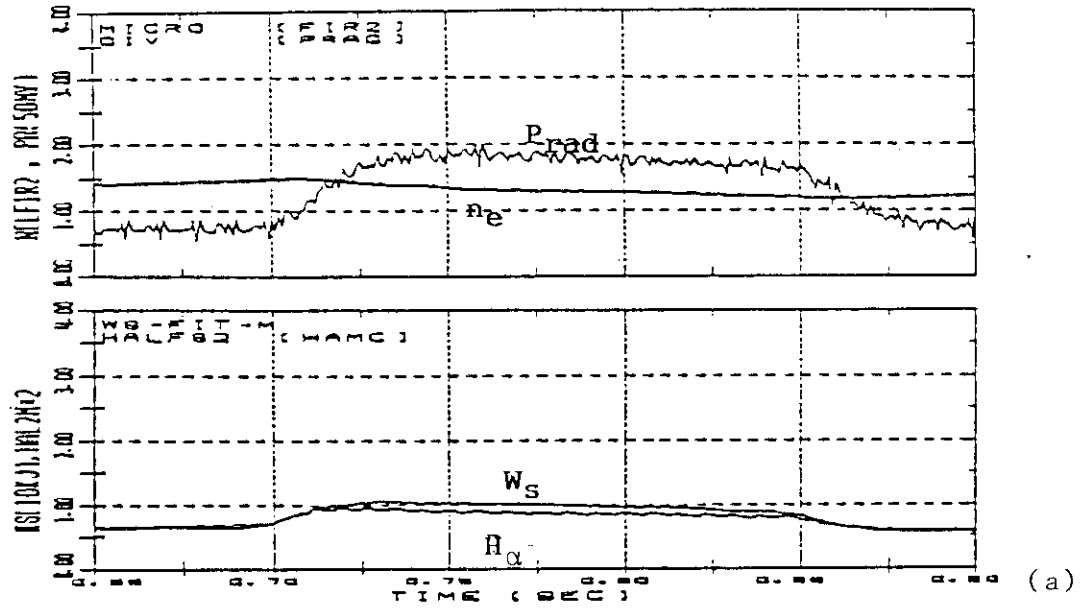


Fig. 1.11 The time evolution of the density, radiation power, stored energy and H emission in the hydrogen discharge for (a) $P_{NB} = 0.47 \text{ MW}$ (below threshold power for H-mode transition) and (b) $P_{NB} = 0.61 \text{ MW}$ (slightly above the threshold power).

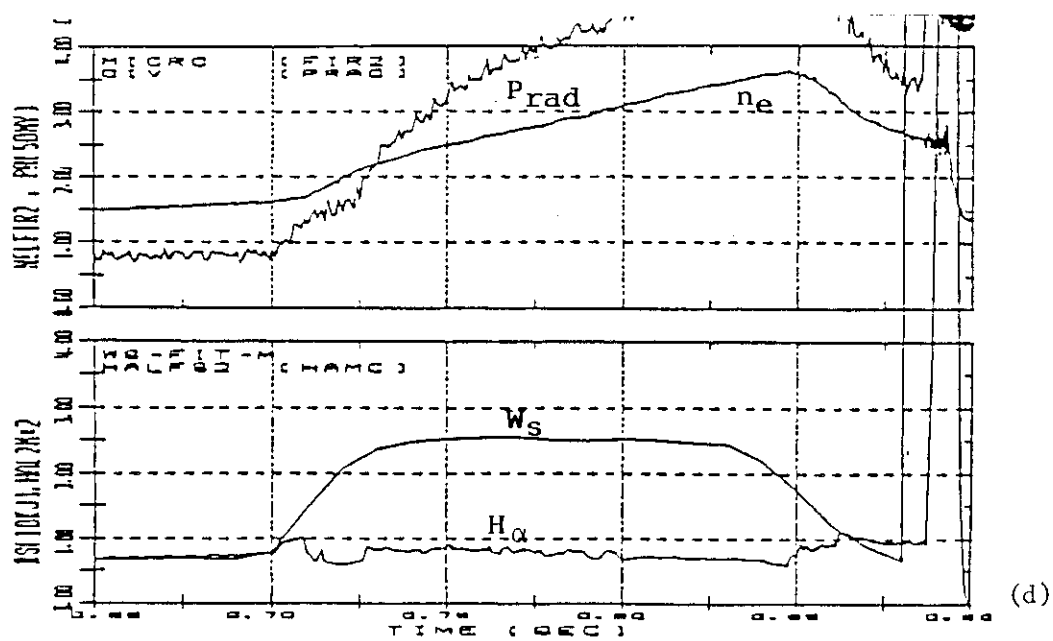
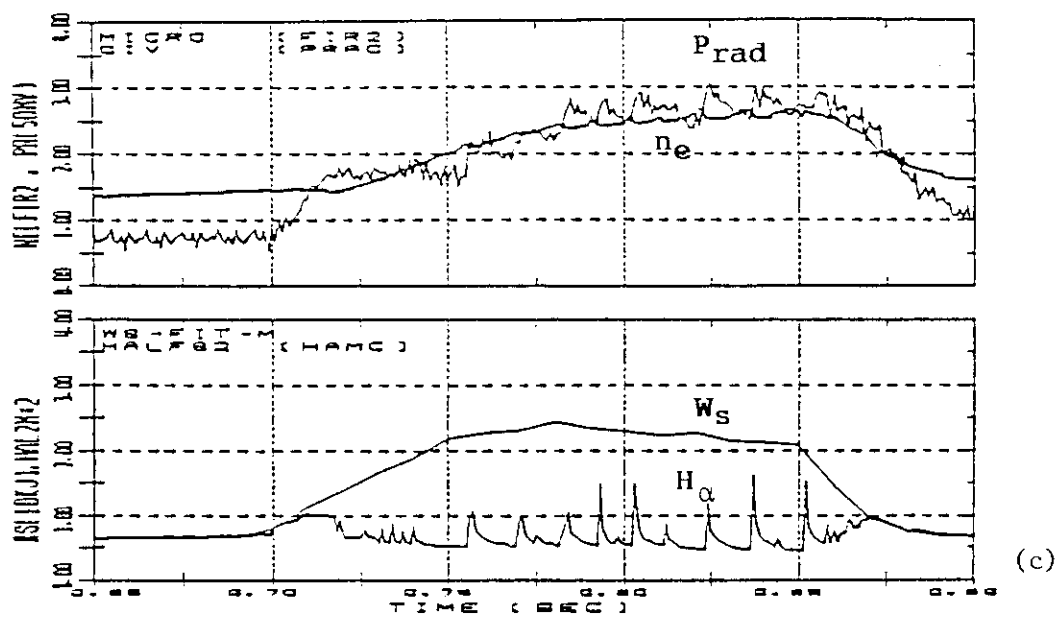


Fig.1.11 The same figures as in Figs.1.11(a) and (b) for
 (c) $P_{NB}=0.74\text{MW}$ and (d) $P_{NB}=1.21\text{MW}$.

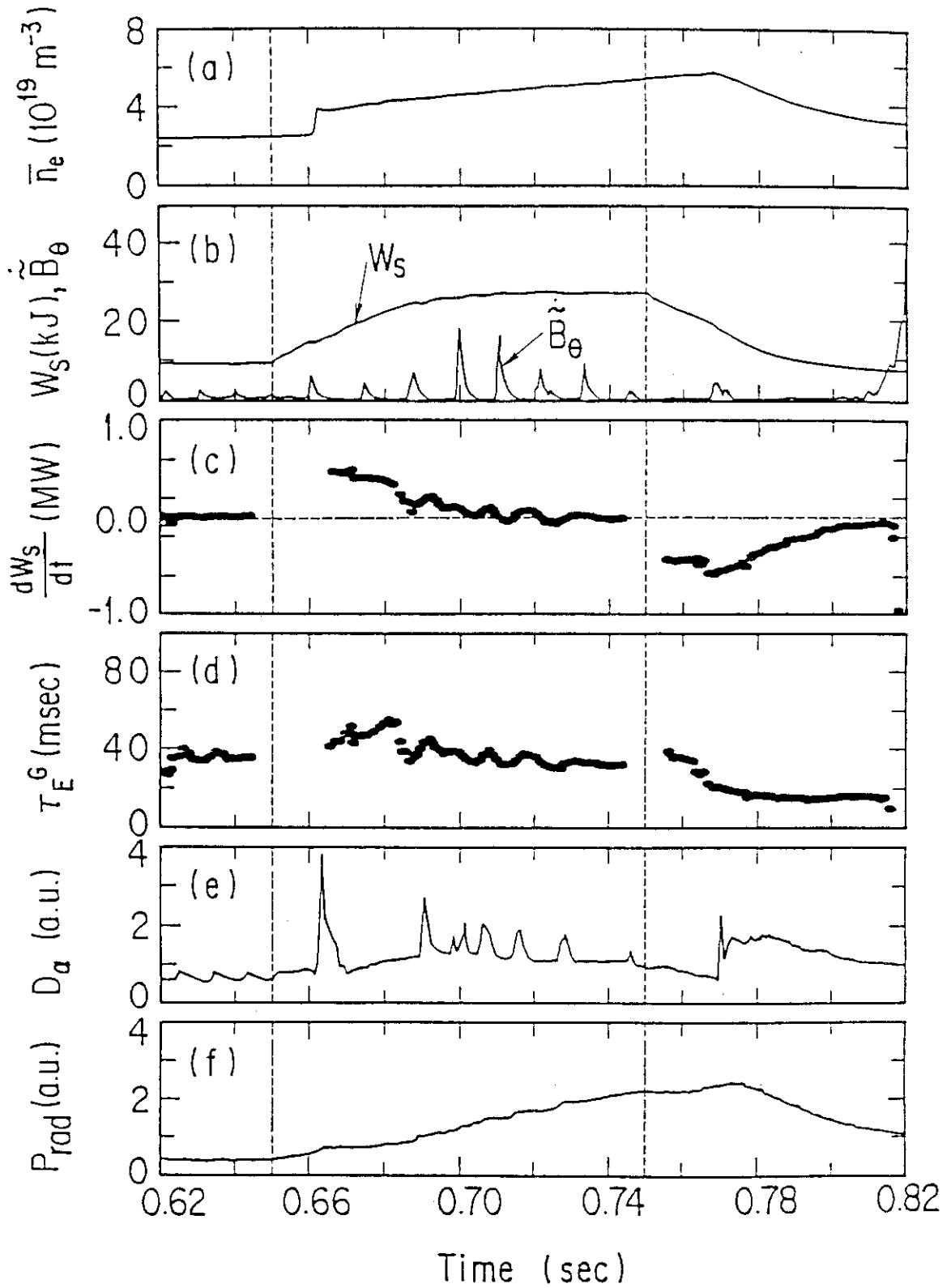


Fig.1.12 Time evolution of various plasma parameters of type 1:
 (a) line-averaged electron density (\bar{n}_e), (b) stored energy (W_s) and half envelope of \tilde{B}_θ signal, (c) differential of W_s determined by fitting 5 points (5 msec) of W_s to cubic function, (d) global energy confinement time (τ_E^G), (e) D_α -intensity apart from the singular point, (f) sum of radiation and charge exchange loss power from lower half of plasma measured by the bolometer.

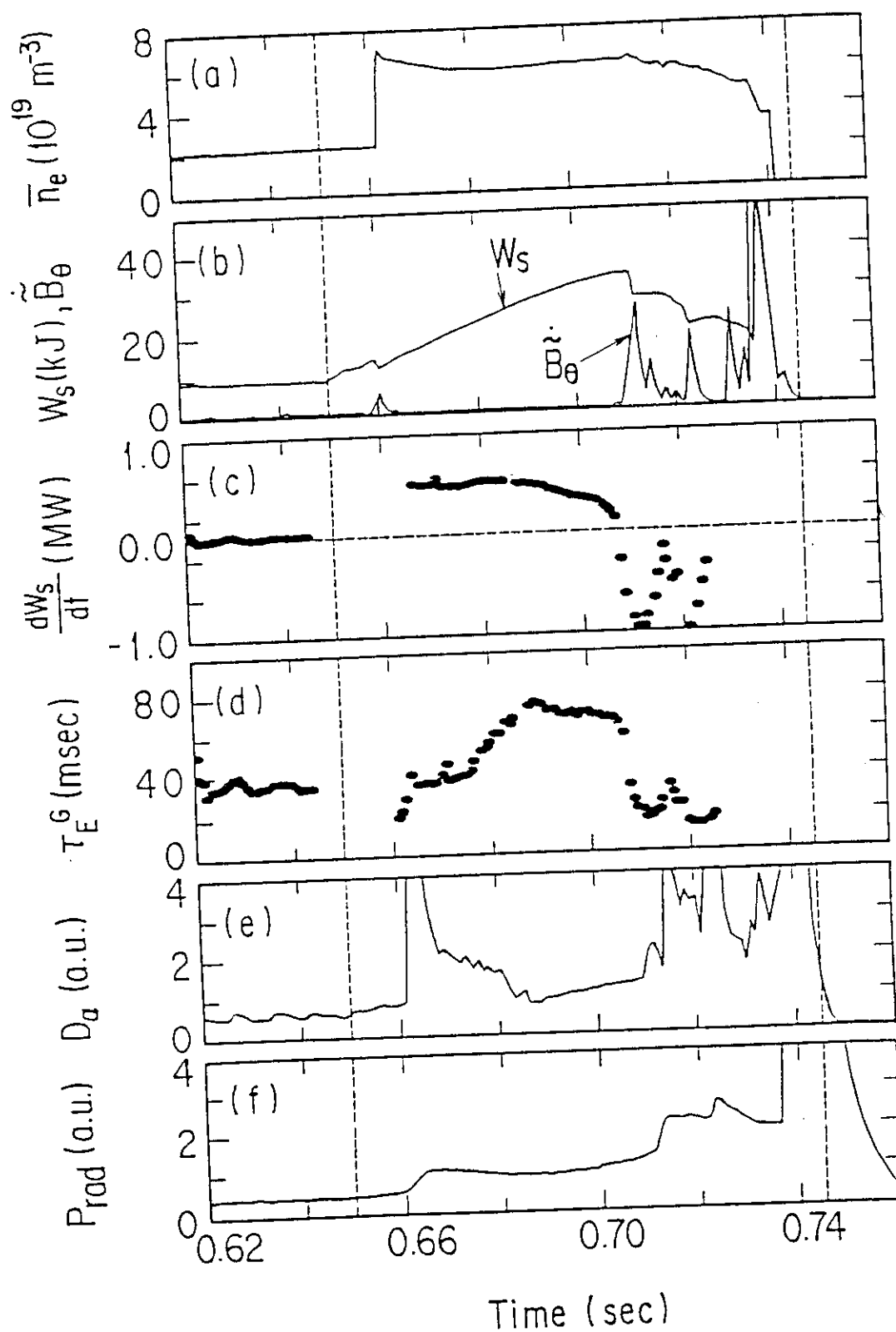


Fig.1.13 Time evolution of various plasma parameters of type 2: columns from (a) to (f) are the same as Fig. 4(a) to Fig. 4(f), respectively.

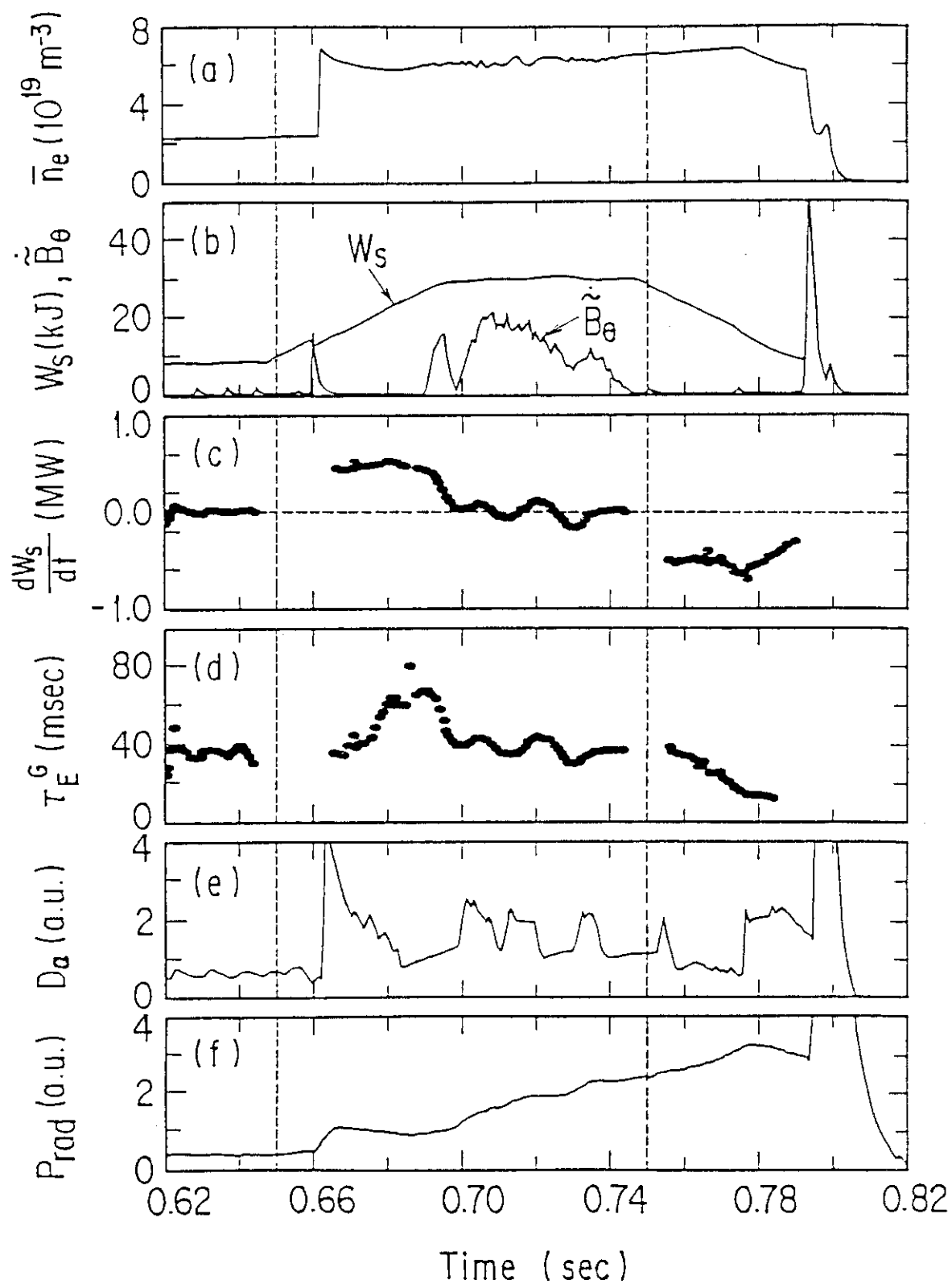


Fig. 1.14 Time evolution of various plasma parameters of type 3: columns from (a) to (f) are the same as Fig. 4(a) to Fig. 4(f), respectively.

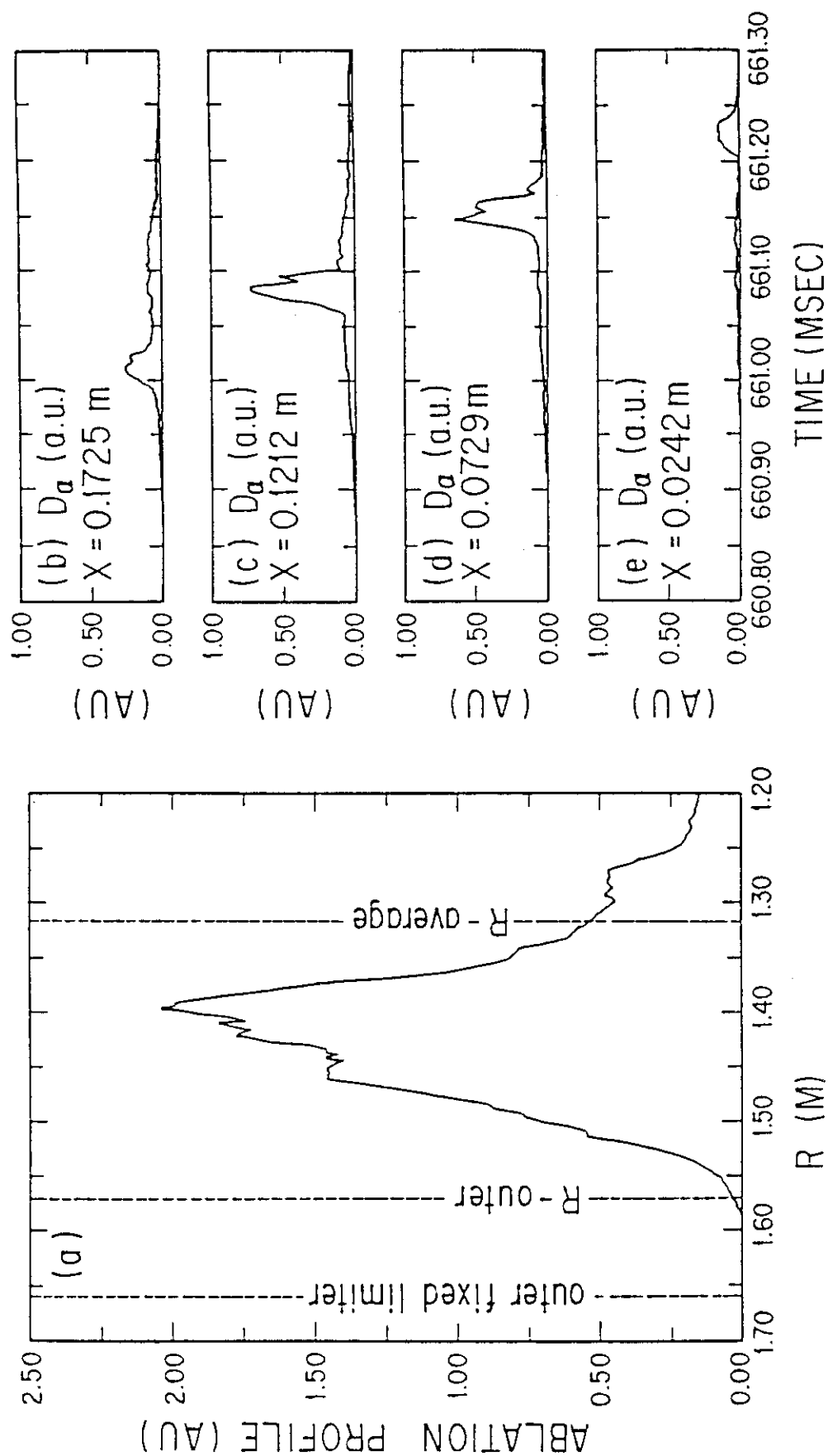


Fig. 1.15 Ablation profiles of the pellet of type 2 discharge: (a) ablation profile measured horizontally by a single H_{α}/D_{α} detector, (b), (c), (d) and (e) are measured vertically by H_{α}/D_{α} detector array. X in (b), (c), (d) and (e) are the length from the center of the vacuum vessel ($R=1.31$ m) on the mid-plane.

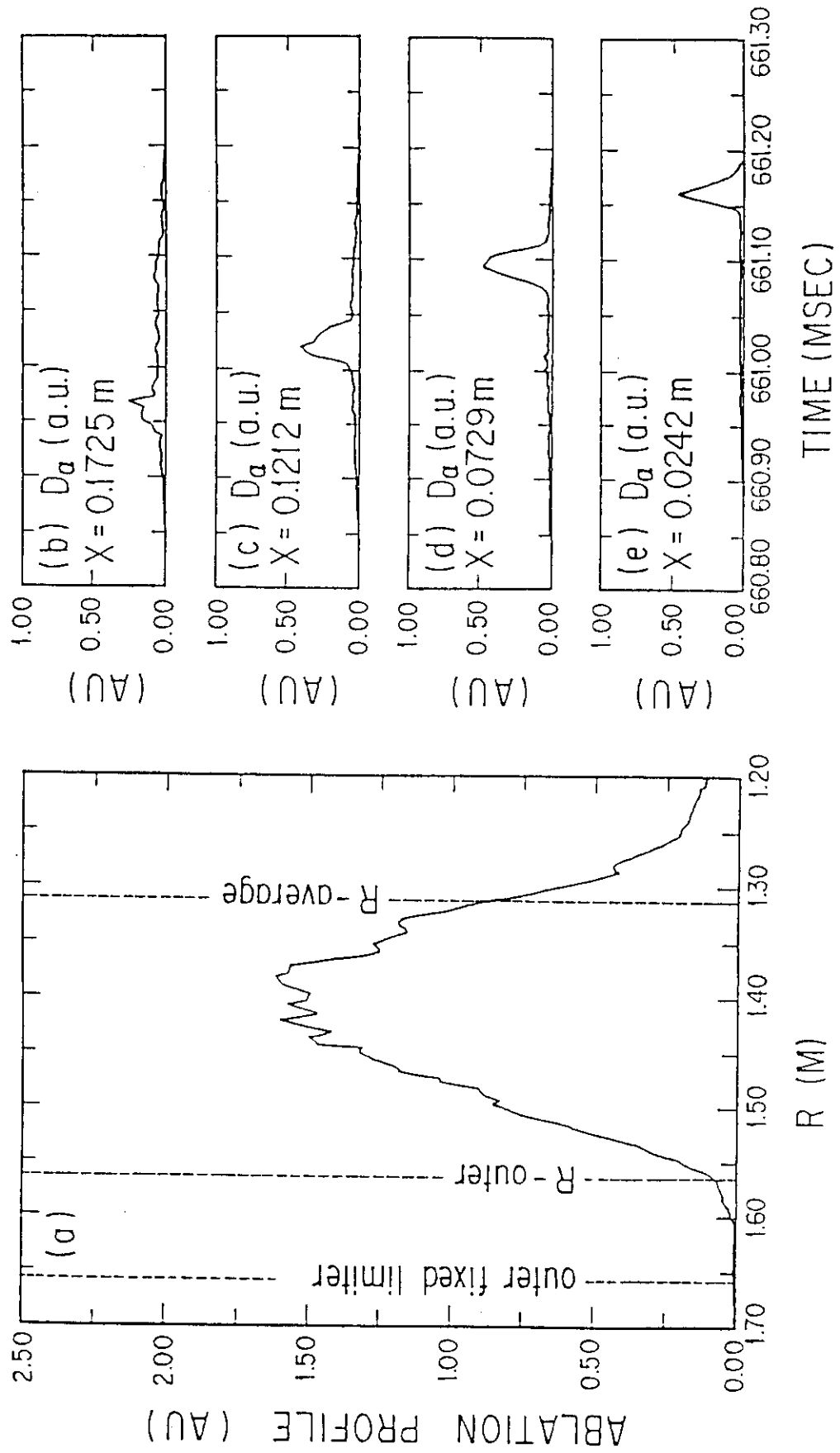


Fig.1.16 Ablation profiles of the pellet of type 3 discharge: columns from (a) to (e) are the same as Fig. 7(a) to Fig. 7(e), respectively.

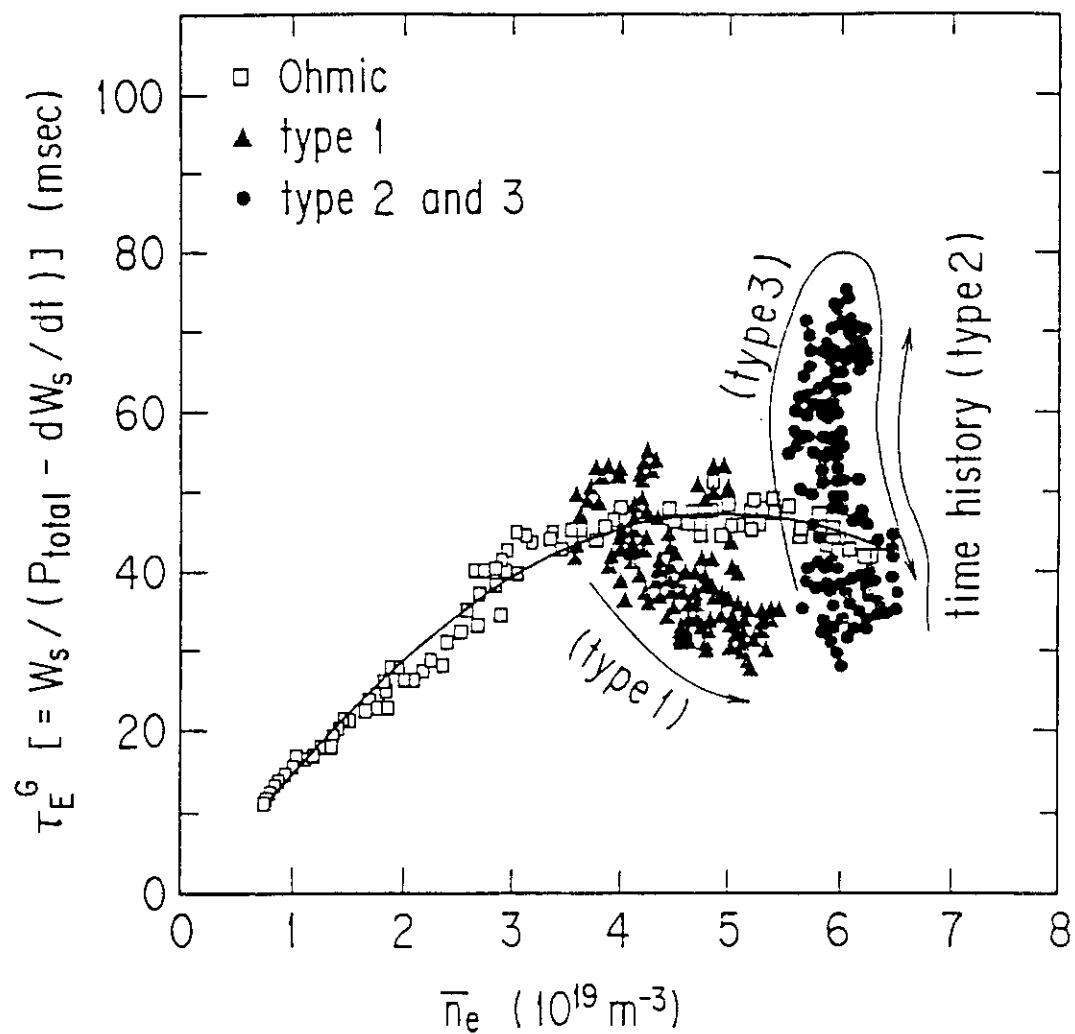


Fig. 1.17 Line-averaged electron density (\bar{n}_e) versus global energy confinement time (τ_E^G). Squares (\square) are τ_E^G of ohmically heated discharges, closed triangles (\blacktriangle) are τ_E^G of type 1 discharges, closed circles (\bullet) are τ_E^G of type 2 and type 3 discharges. Arrows show the time history of τ_E^G in type 1, 2 and 3 discharges.

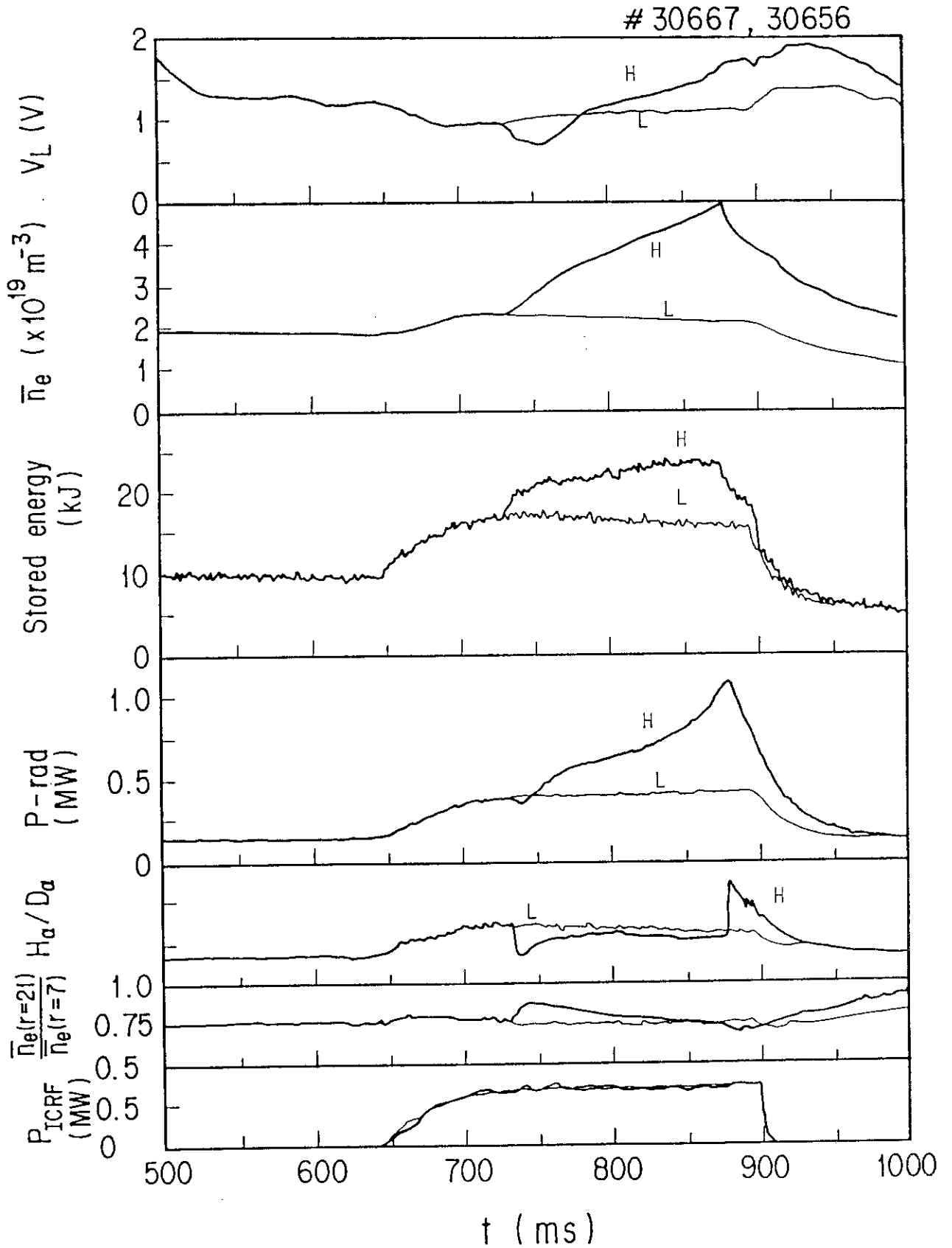


Fig.1.18 Time evolution of H-mode discharge during ICRF heating.
Thin lines denote the case of L-mode discharge.

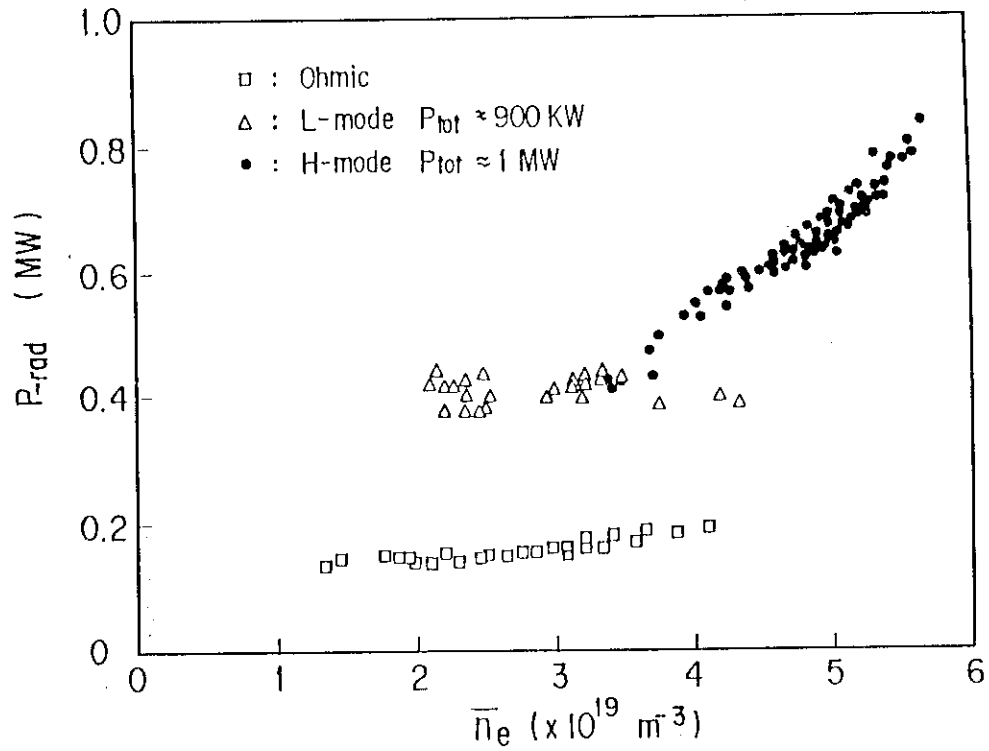


Fig.1.19 Radiation power vs. density. Solid circles denote the case of H-mode discharge.

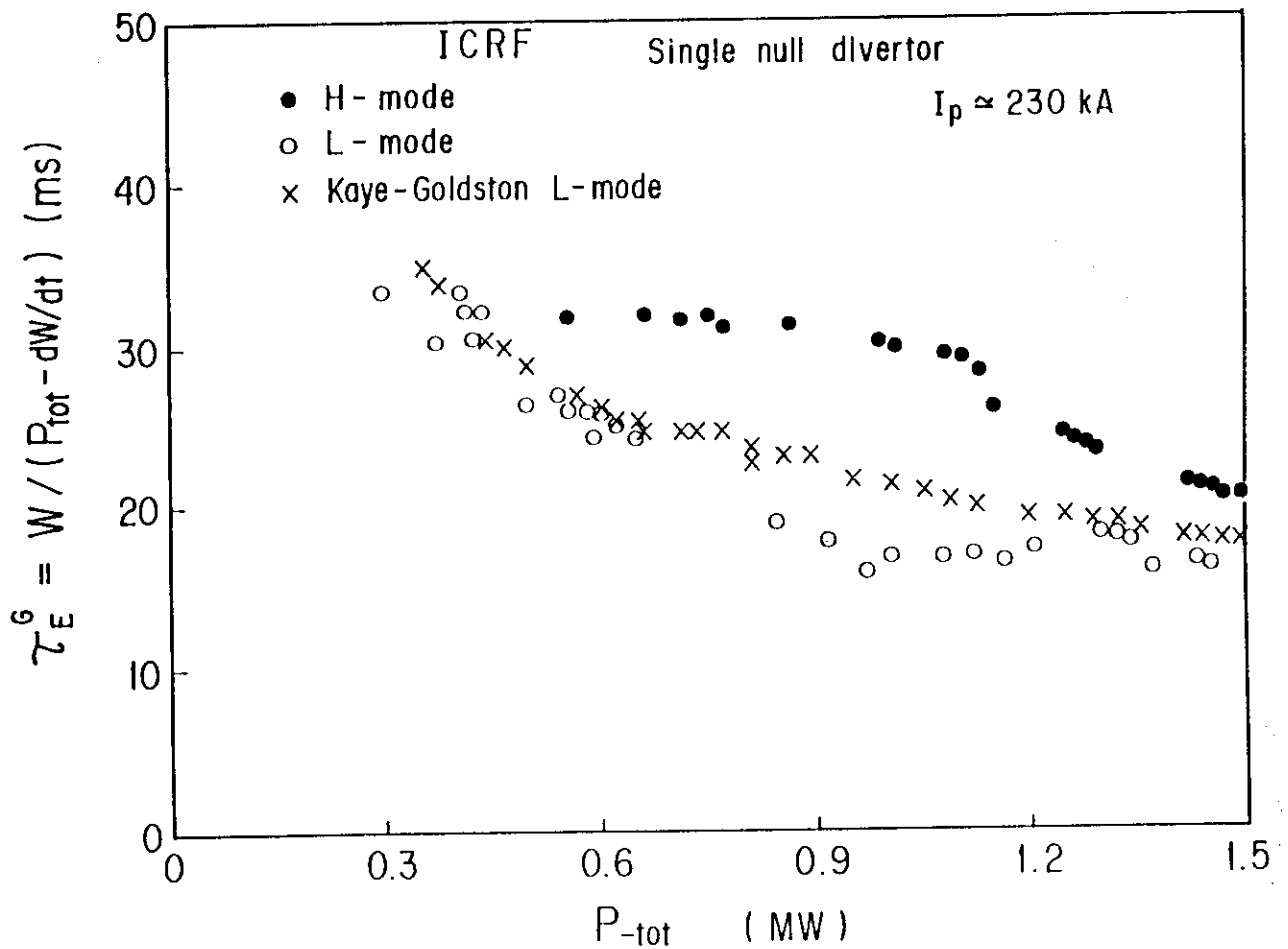


Fig. 1.20 Energy confinement time vs. total power for ICRF heating.

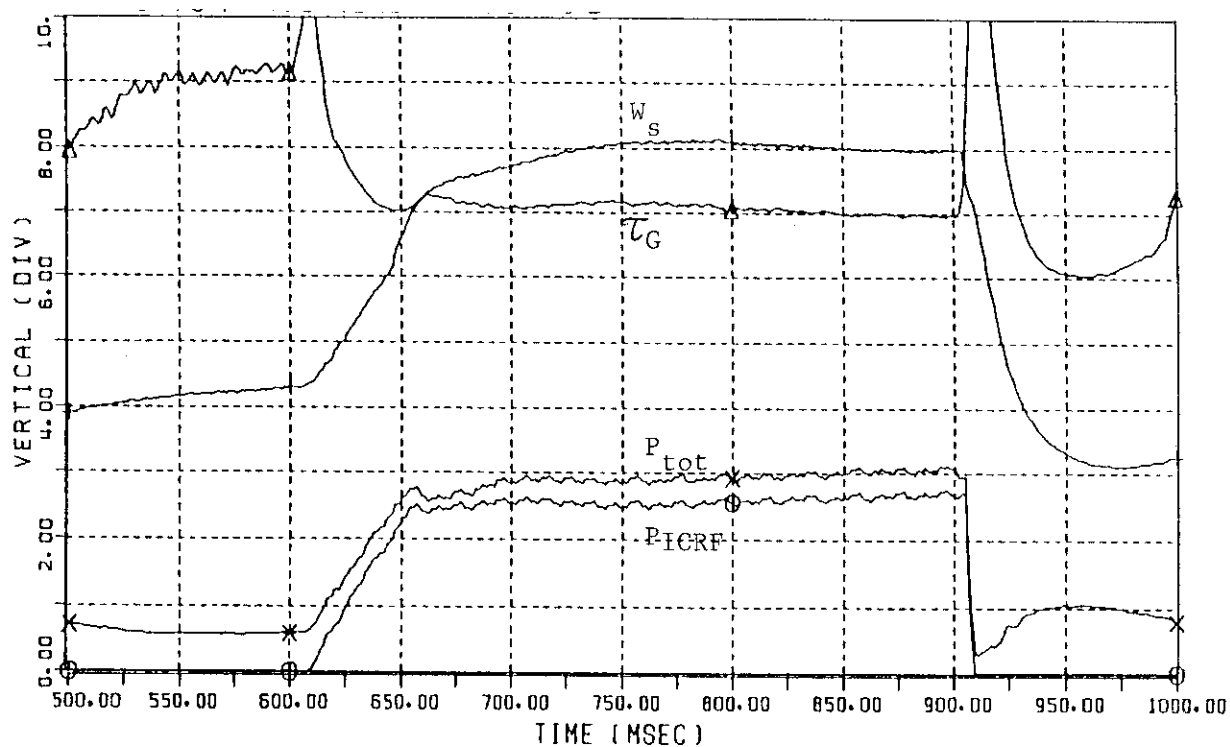
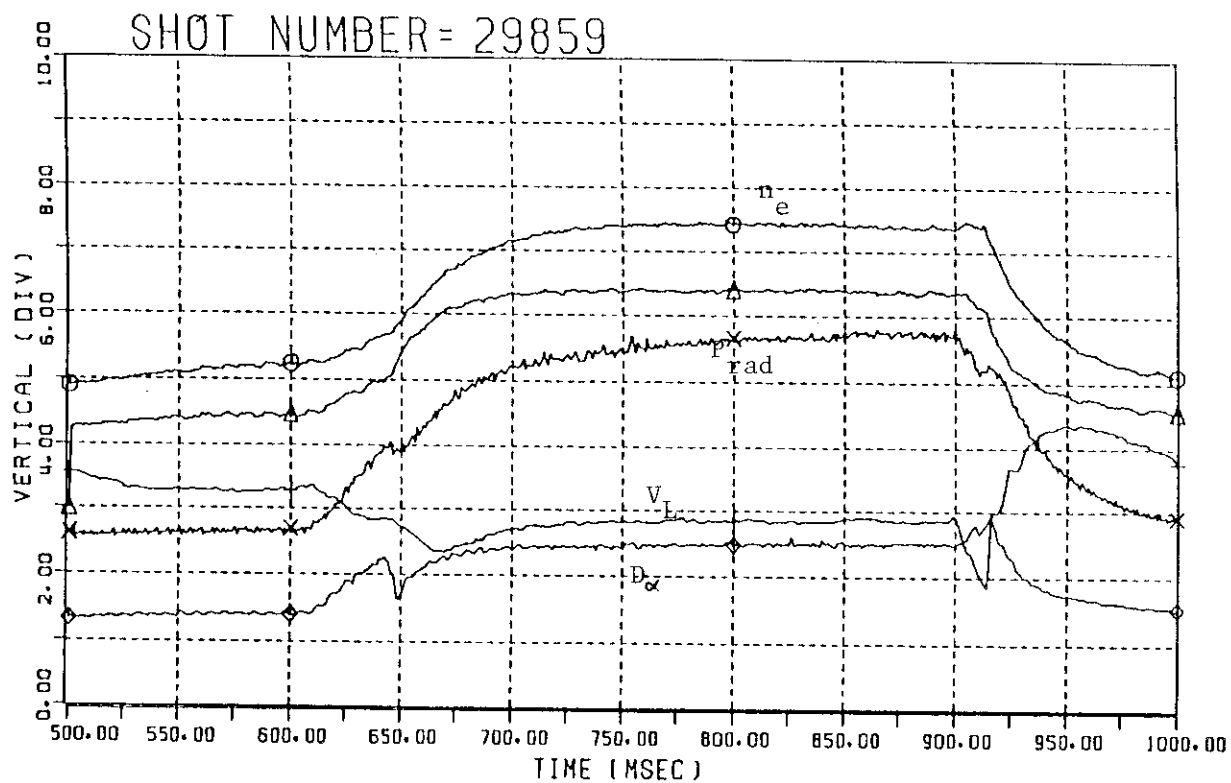


Fig. 1.21 Discharge with ICRF heating for $P_{tot} = 1.5\text{MW}$.
The increase of D_α emission is close to the L-mode discharge.

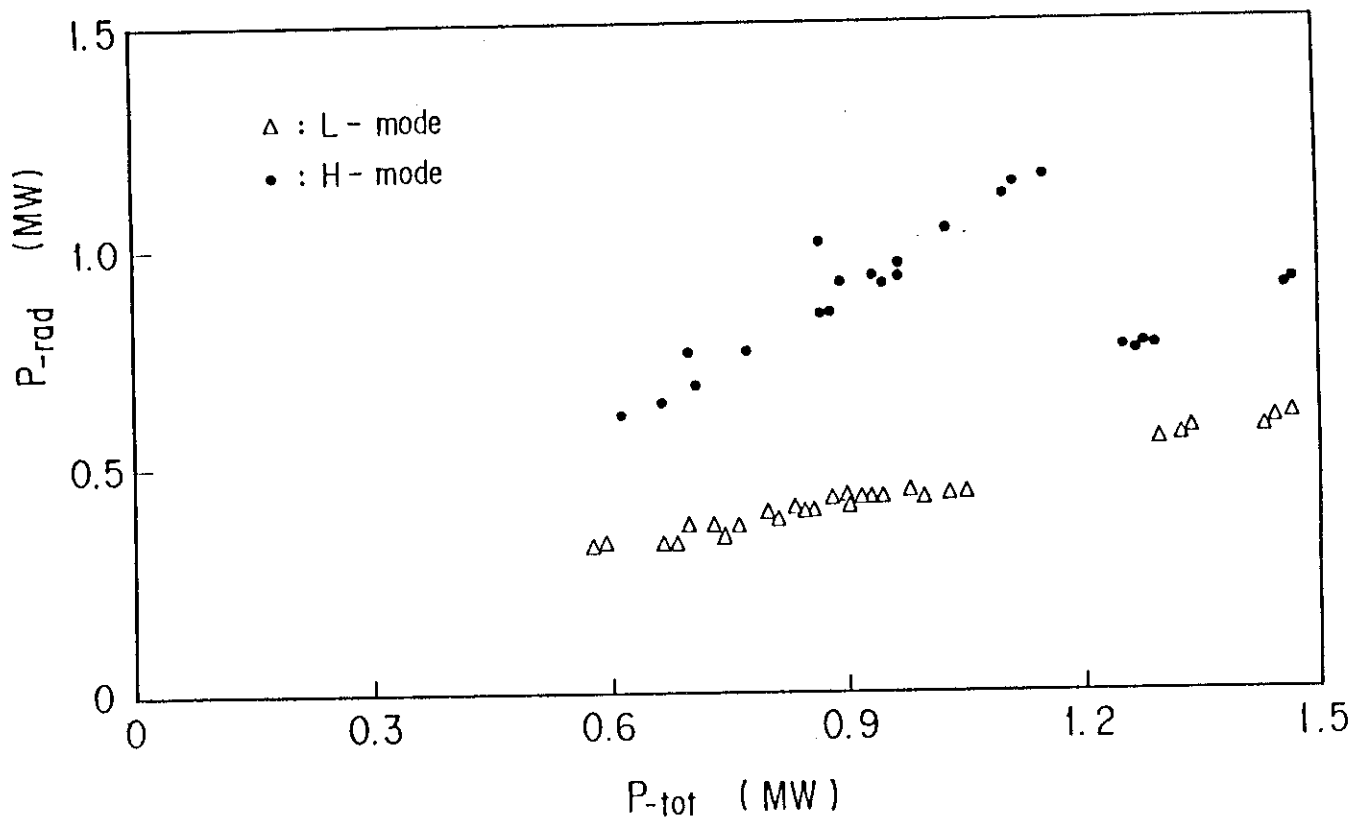


Fig. 1.22 Radiation power vs. total heating power for ICRF heating.

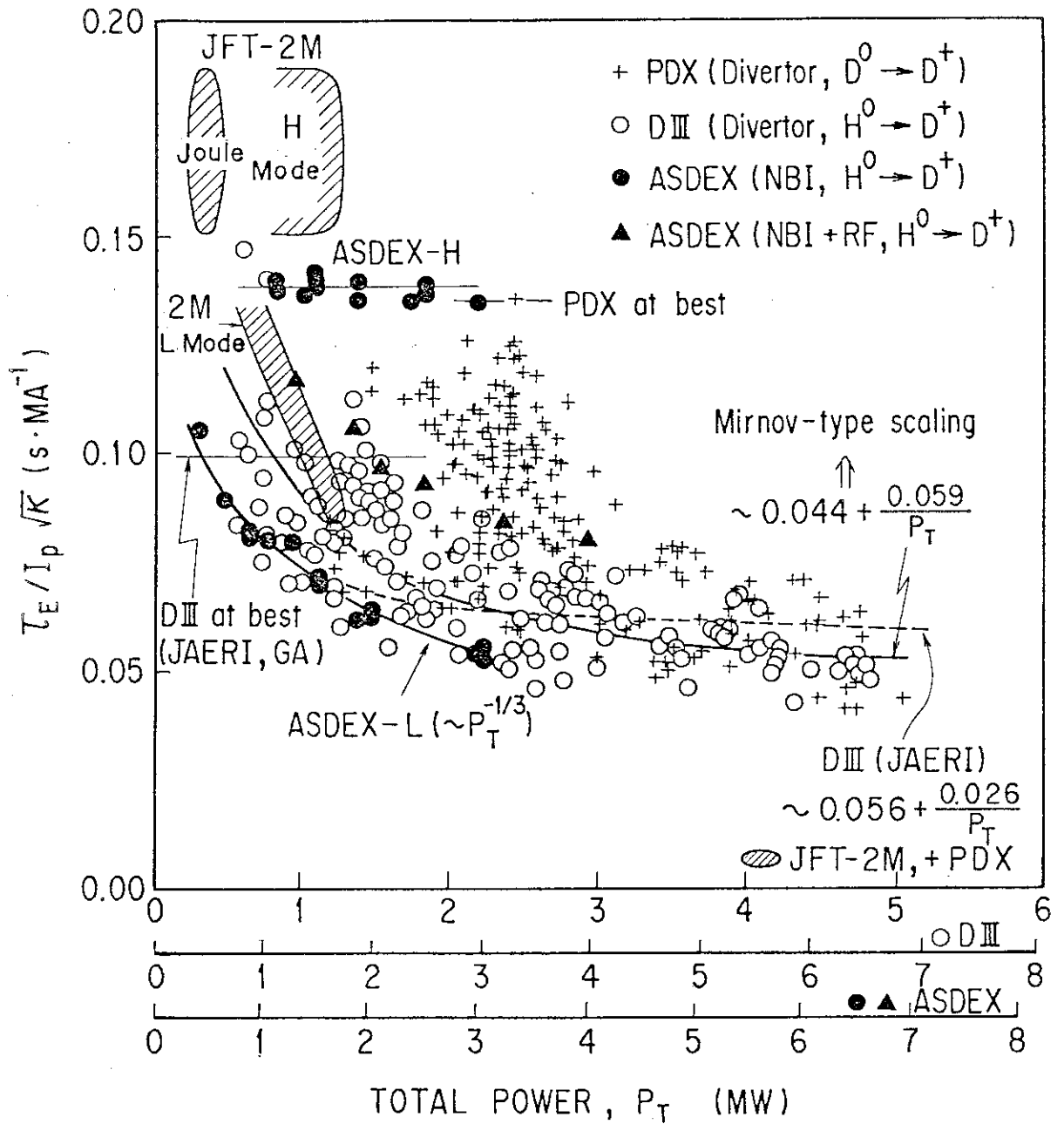


Fig. 1.23 Normalized energy confinement time vs. total heating power. A Mirnov-type scaling is obtained from the tendency of the Doublet-III data at high power region.

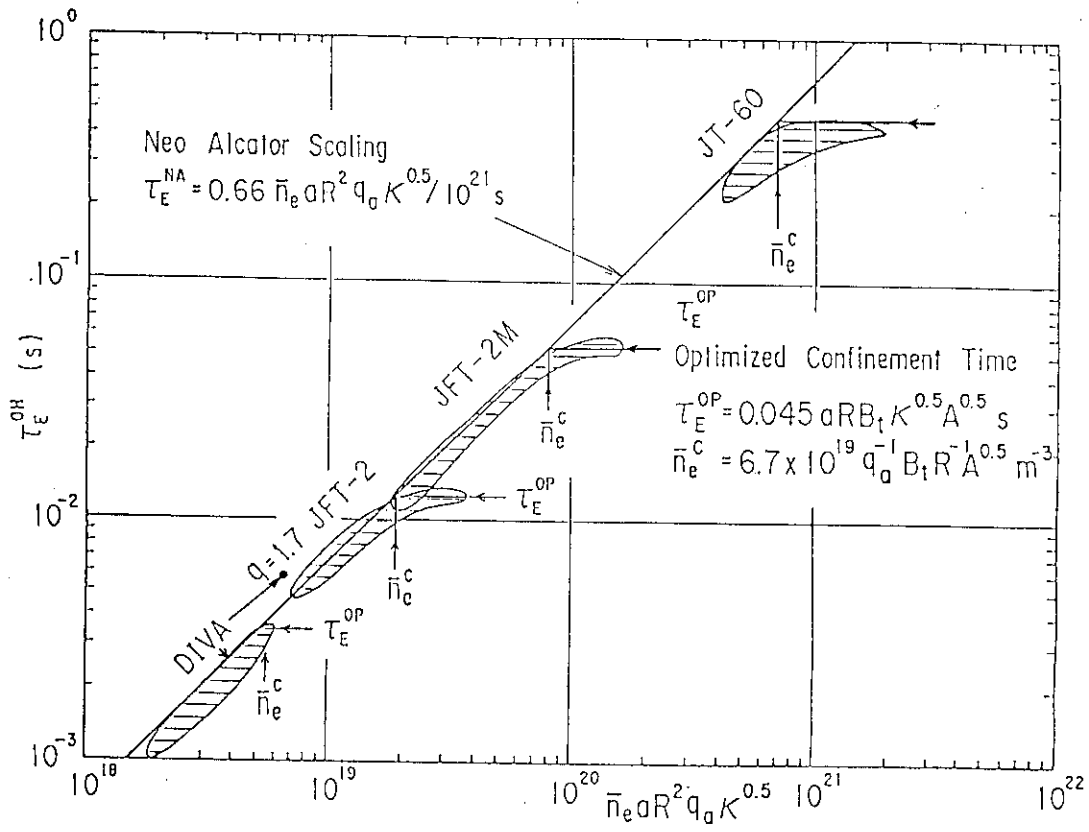


Fig.1.24 Energy confinement time of ohmic discharges.

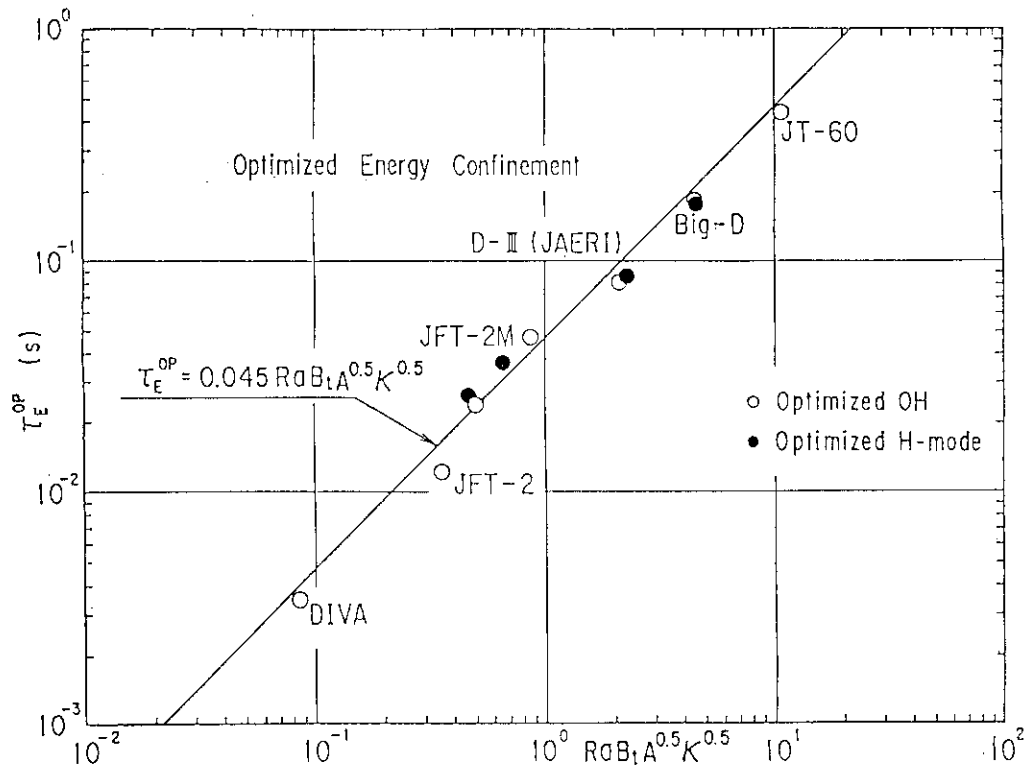


Fig.1.25 Empirical scaling of optimized confinement time in ohmic and H-mode discharges.

```

ITIME=      15
BETA-M=    3.90033
BETA-T=    3.01317
BETA-J=    1.19897
TCU       =    5.45177
BTU       =   22.00000
Q-AXIS=    1.08956
O-SURF=    3.12853
TOT-PR=   44.77979
COIL-0=    5.85694
COIL-1=    1.74113
COIL-2=   -0.29161
COIL-3=   -0.07881
COIL-4=   -0.09763
COIL-5=    0.0
RMAJ      =    4.00000
R-AXIS=    4.10627
S-AXIS=   -3.03798
VOLUME=   123.46952
ELIP      =    1.62691
TRIG      =    0.30189
PBLMIN=   9.8830-01

```

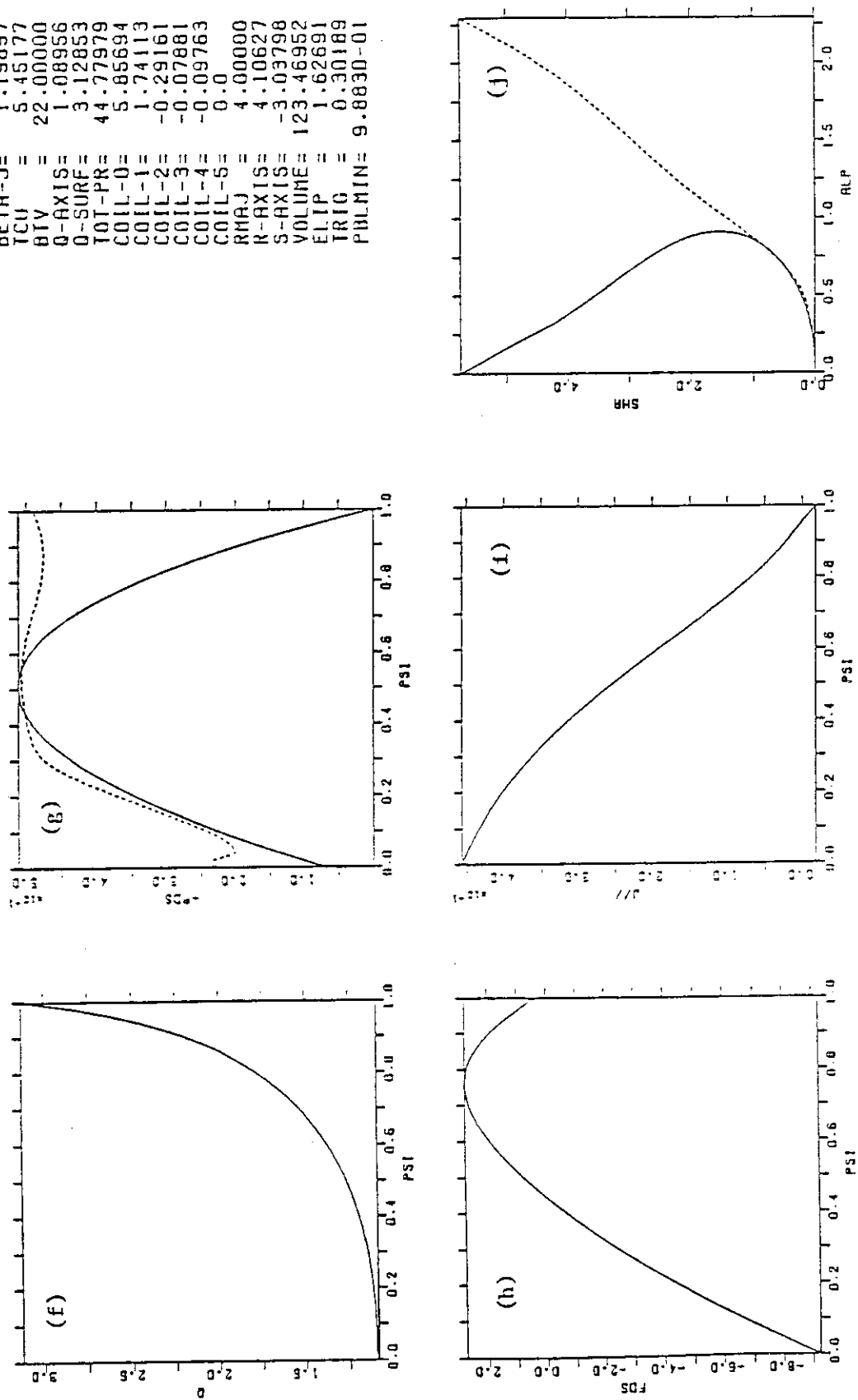


Fig.2.1 Profiles in equilibrium Data 1. $\beta_1=3.01\%$.

```

ITIME=      22
BETA-X=    5.14433
BETA-T=    4.31146
BETA-J=    1.62635
TCU       =    5.61044
BTV       =   22.00000
Q-AXIS=    1.09463
Q-SURF=    3.12327
TOT-PR=    64.32872
COIL-0=    6.07882
COIL-1=    1.96453
COIL-2=   -0.27820
COIL-3=   -0.08000
COIL-4=   -0.08620
COIL-5=    0.0
RMAJ      =    4.00000
R-AXIS=    4.10774
S-AXIS=   -3.04085
VOLUME=   123.93968
ELIP      =    1.61458
TRIG      =    0.30841
PBLMIN=   4.7580-03
  
```

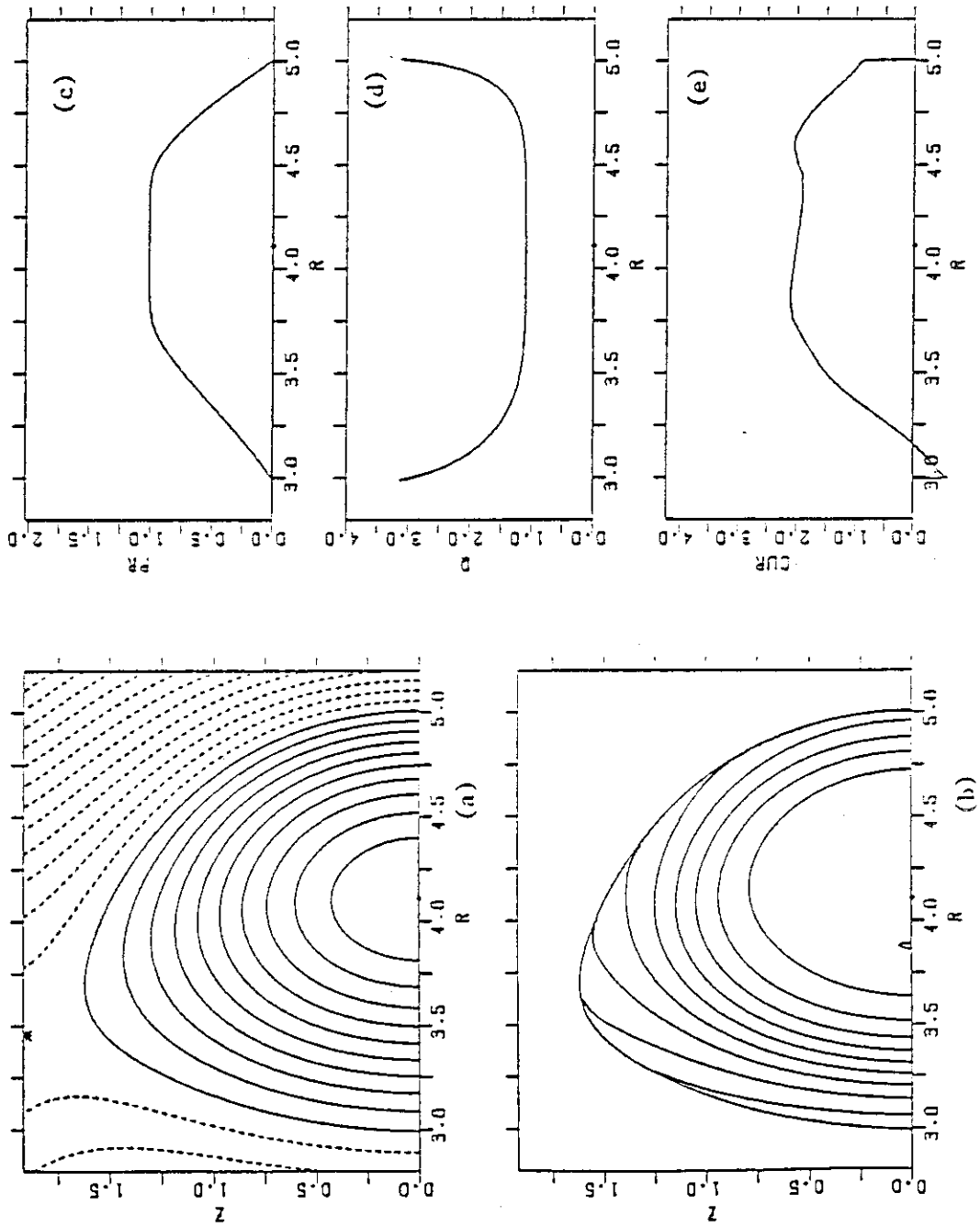


Fig. 2.2 Profiles in equilibrium Data 2. $\beta_t=4.31\%$.

```

ITIME=      22
BETA-X=    5.14433
BETA-T=    4.31146
BETA-J=    1.62635
TCU =      5.61044
RTV =      22.00000
O-AXIS=    1.09463
O-SURF=    3.12327
TOT-PR=    64.32872
COIL-0=    6.07882
COIL-1=    1.96453
COIL-2=   -0.27820
COIL-3=   -0.08000
COIL-4=   -0.08620
COIL-5=    0.0
RHAJ =     4.00000
R-AXIS=    4.10774
S-AXIS=   -3.04085
VOLUME=   123.93968
ELIP =     1.61458
TRIG =     0.30841
PBLMIN=   4.7580-03

```

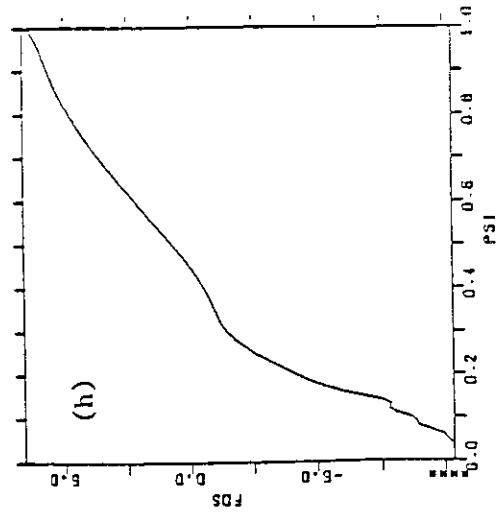
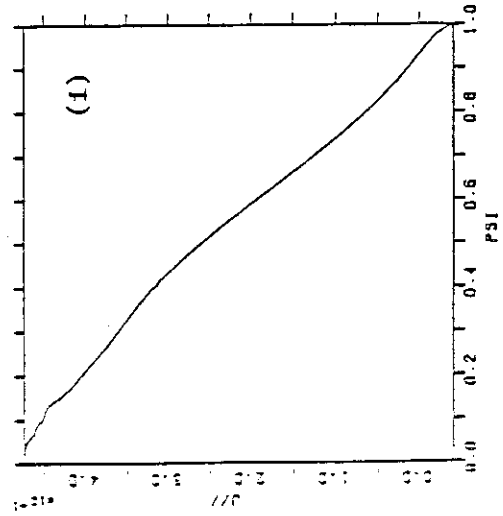
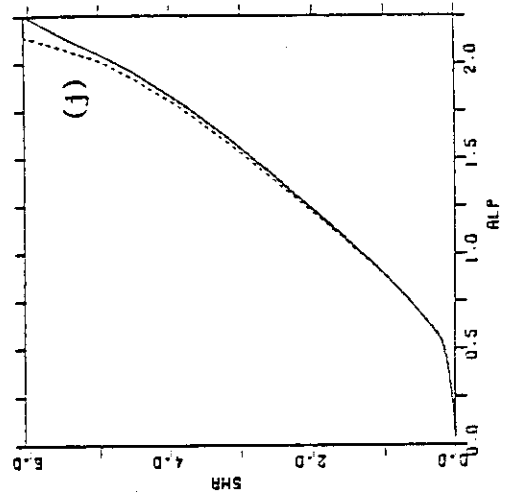
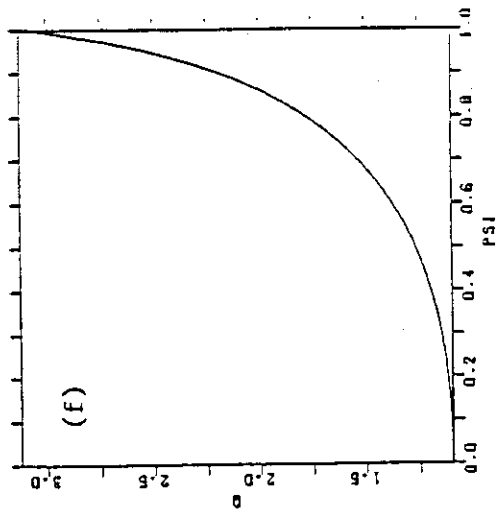
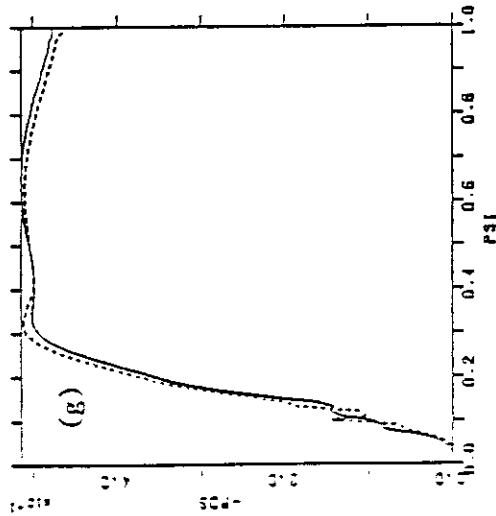


Fig.2.2.2 Profiles in equilibrium Data 2. $\beta_t=4.31\%$.

I TIME= 21
 BEI A-M= 5.02848
 BETA-T= 4.11110
 BETA-J= 1.70117
 TCU = 5.35631
 BTU = 22.00000
 A-AXIS= 1.09417
 O-SURF= 3.19673
 TOT-PR= 61.33061
 COIL-0= 5.79489
 COIL-1= 1.89423
 COIL-2= -0.24881
 COIL-3= -0.07182
 COIL-4= -0.07715
 COIL-5= 0.0
 RMRJ = 4.00000
 R-AXIS= 4.14929
 S-AXIS= -2.77145
 VOLUME= 123.93123
 ELTP = 1.61168
 TRIG = 0.29907
 POLMIN= 9.6480-01

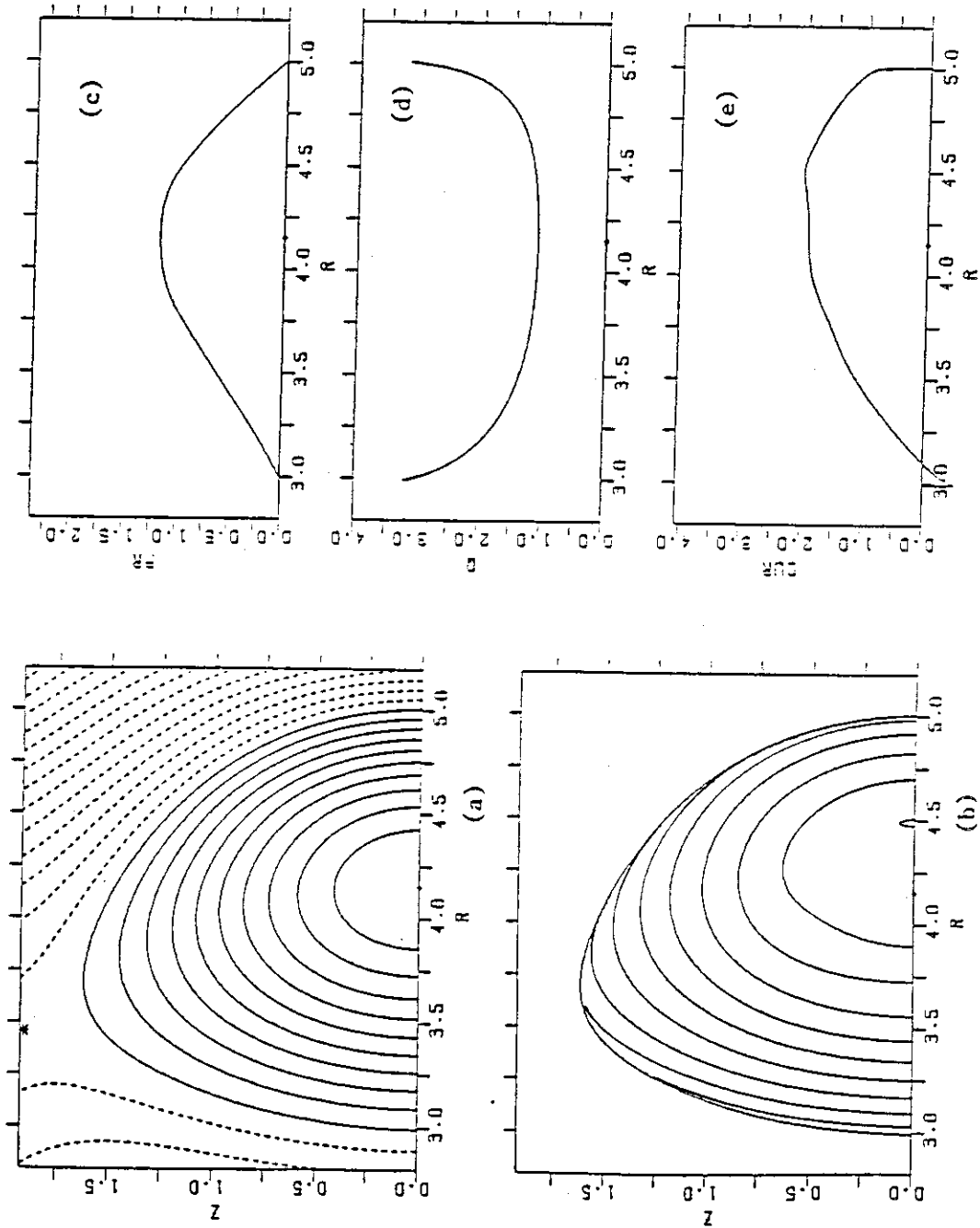


Fig. 2.3 Profiles in equilibrium Data 3. $\beta_t=4.11\%$.

```

21
ITIME= 5.02848
BETA-M= 4.11110
BETA-T= 1.70117
BETA-J= 5.35631
TCU= 22.00000
BTV= 1.09417
O-AXIS= 3.19673
O-SURF= 61.33061
TOT-PR= 5.79489
COIL-0= 1.89423
COIL-1= -0.24881
COIL-2= -0.07182
COIL-3= -0.07715
COIL-4= 0.0
COIL-5= 4.00000
RMAJ= 4.14929
R-AXIS= -2.77145
S-AXIS= 123.93123
VOLUME= 1.61168
ELIP= 0.29907
TRIG= 9.6480-01
PBLMIN=

```

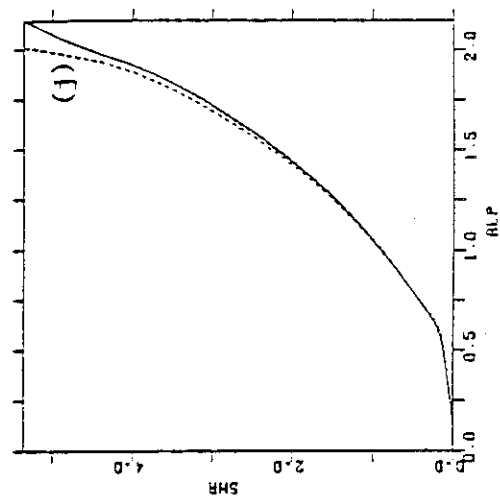
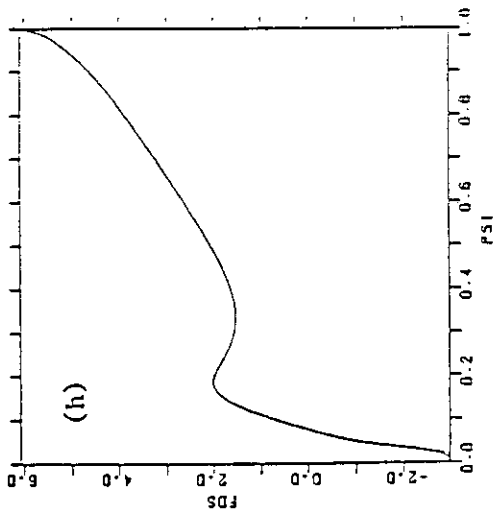
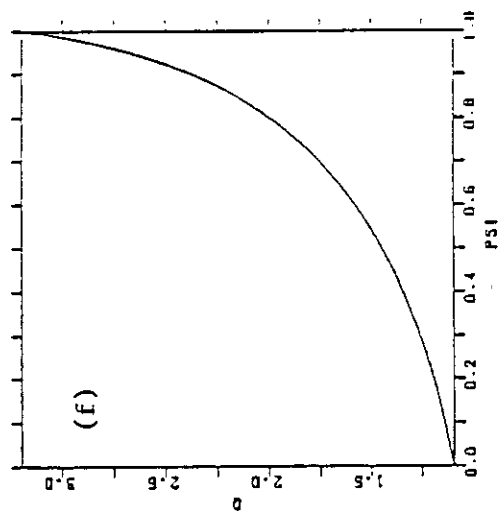
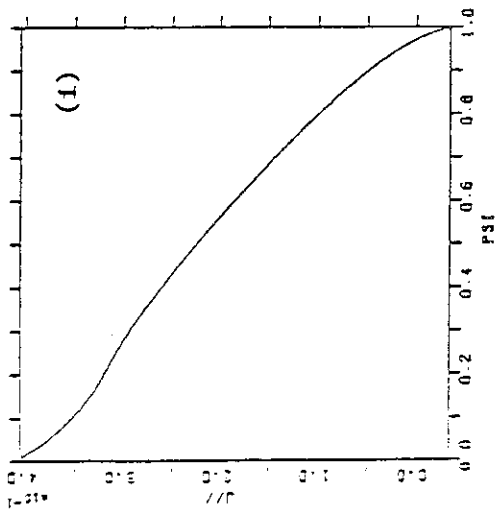
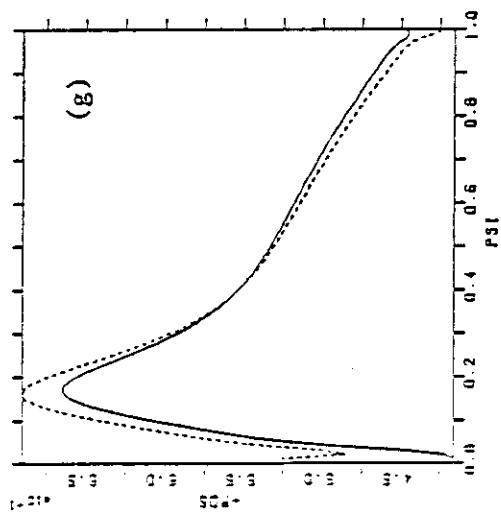


Fig.2.2.3 Profiles in equilibrium Data 3. $\beta_t=4.11\%$.

ITIME= 18
 BETA-M= 4.46297
 BETA-T= 3.52757
 BETA-J= 1.49884
 ICU = 5.28074
 BTU = 22.00000
 Q-AXIS= 1.09417
 Q-SURF= 3.19673
 TOT-PR= 52.52188
 COIL-0= 5.69106
 COIL-1= 1.79130
 COIL-2= -0.25471
 COIL-3= -0.07206
 COIL-4= -0.07976
 COIL-5= 0.0
 RMAJ = 4.00000
 R-AXIS= 4.14260
 S-AXIS= -2.77225
 VOLUME= 123.69966
 ELIP = 1.61035
 TRIG = 0.29907
 PBLMIN= 7.9210-01

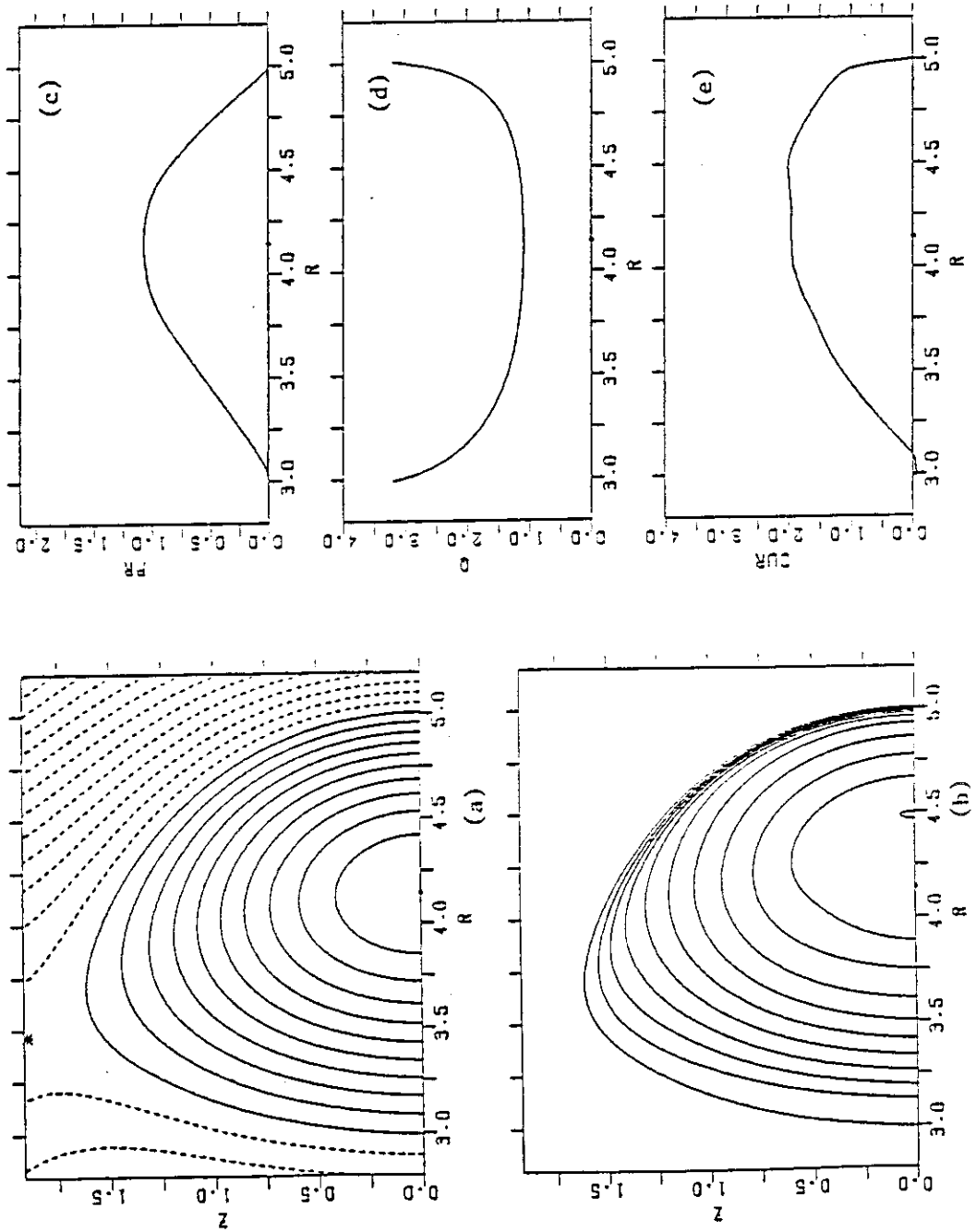


Fig.2.4 Profiles in equilibrium Data 4. $\beta_t=3.53\%$.

I TIME= 18
 BETA-M= 4.46297
 BETA-T= 3.52757
 BETA-J= 1.49884
 TCU = 5.28074
 BTU = 22.00000
 Q-AXIS= 1.09417
 Q-SURF= 3.19673
 TOT-PR= 52.52188
 COIL-0= 5.69106
 COIL-1= 1.79130
 COIL-2= -0.25471
 COIL-3= -0.07206
 COIL-4= -0.07976
 COIL-5= 0.0
 RMAJ = 4.00000
 R-AXIS= 4.14260
 S-AXIS= -2.77225
 VOLUME= 123.69966
 ELIP = 1.61035
 TRIG = 0.29907
 PBLMIN= 7.9210-01

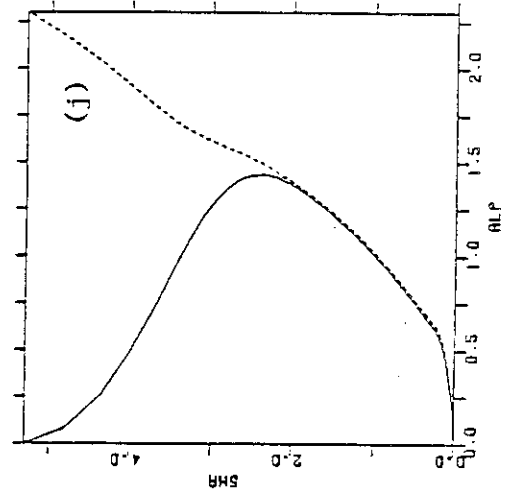
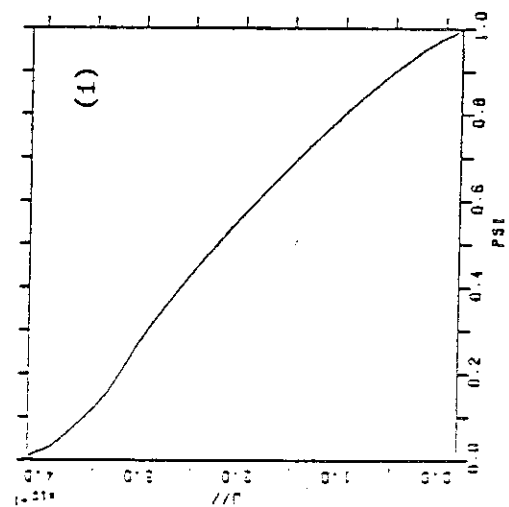
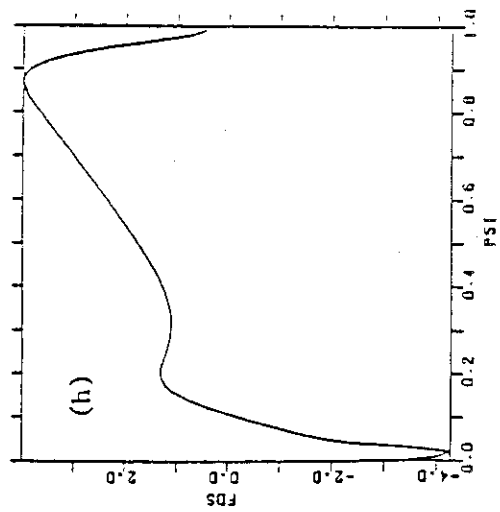
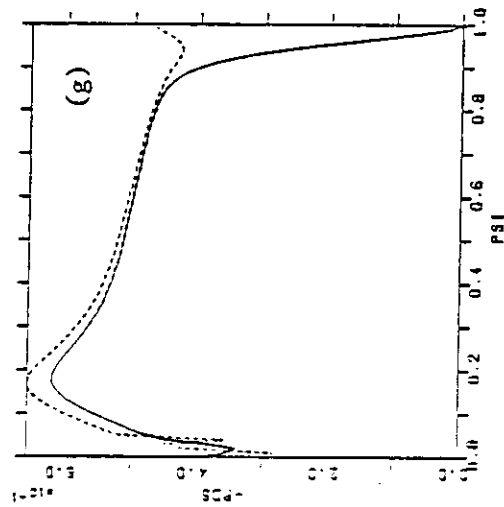
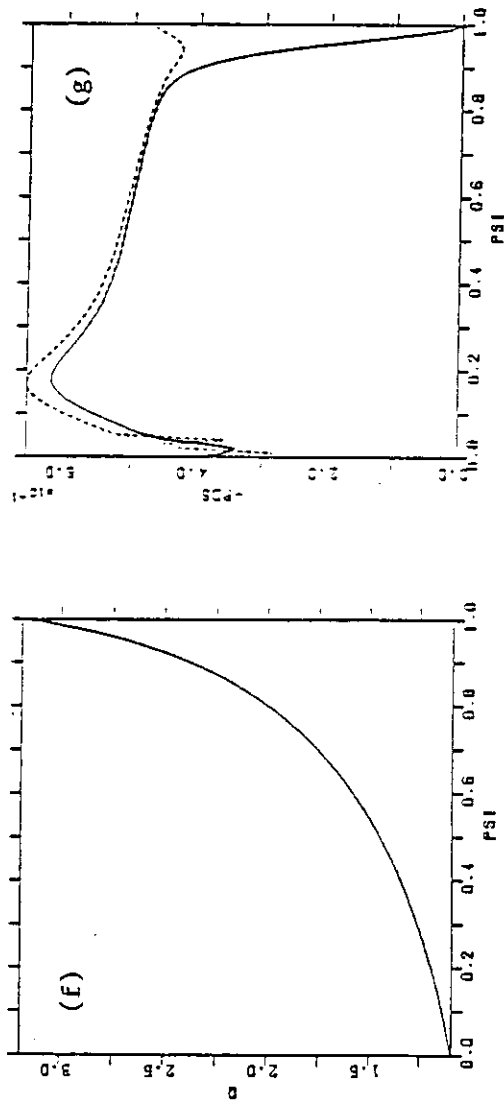


Fig.2.4 Profiles in equilibrium Data 4. $\beta_t=3.53\%$.

NUMERU= 17
 BETA-T= 3.79929
 BETA-M= 4.89458
 BETA-P= 1.96725
 Q-AXIS= 1.10098
 Q-SURF= 3.12568
 ASPECT= 3.97180
 ELLIPT= 1.60629
 TRIG= 0.30044

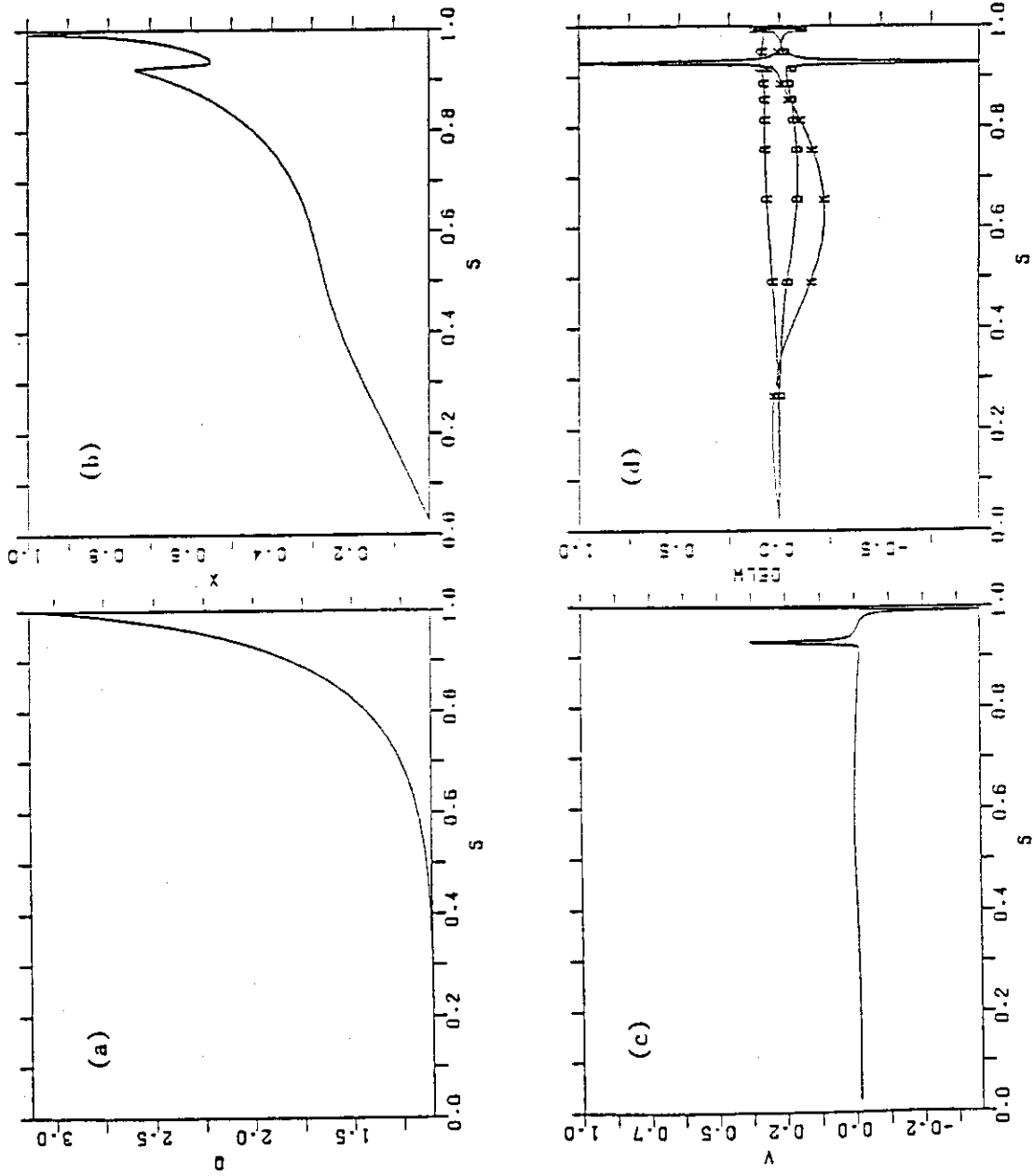


Fig. 2.5 Mode structure near beta limit for the equilibrium Data 1.
 $\beta_t = 3.80\%$ and $\gamma^2 = 1.45 \times 10^5$.

NUMEQ= 19
 BETA-T= 3.99956
 BETA-W= 5.14720
 BETA-P= 2.05459
 Q-AXIS= 1.10067
 Q-SURF= 3.12455
 ASPECT= 3.97071
 ELLIPT= 1.60613
 TRIG = 0.30025

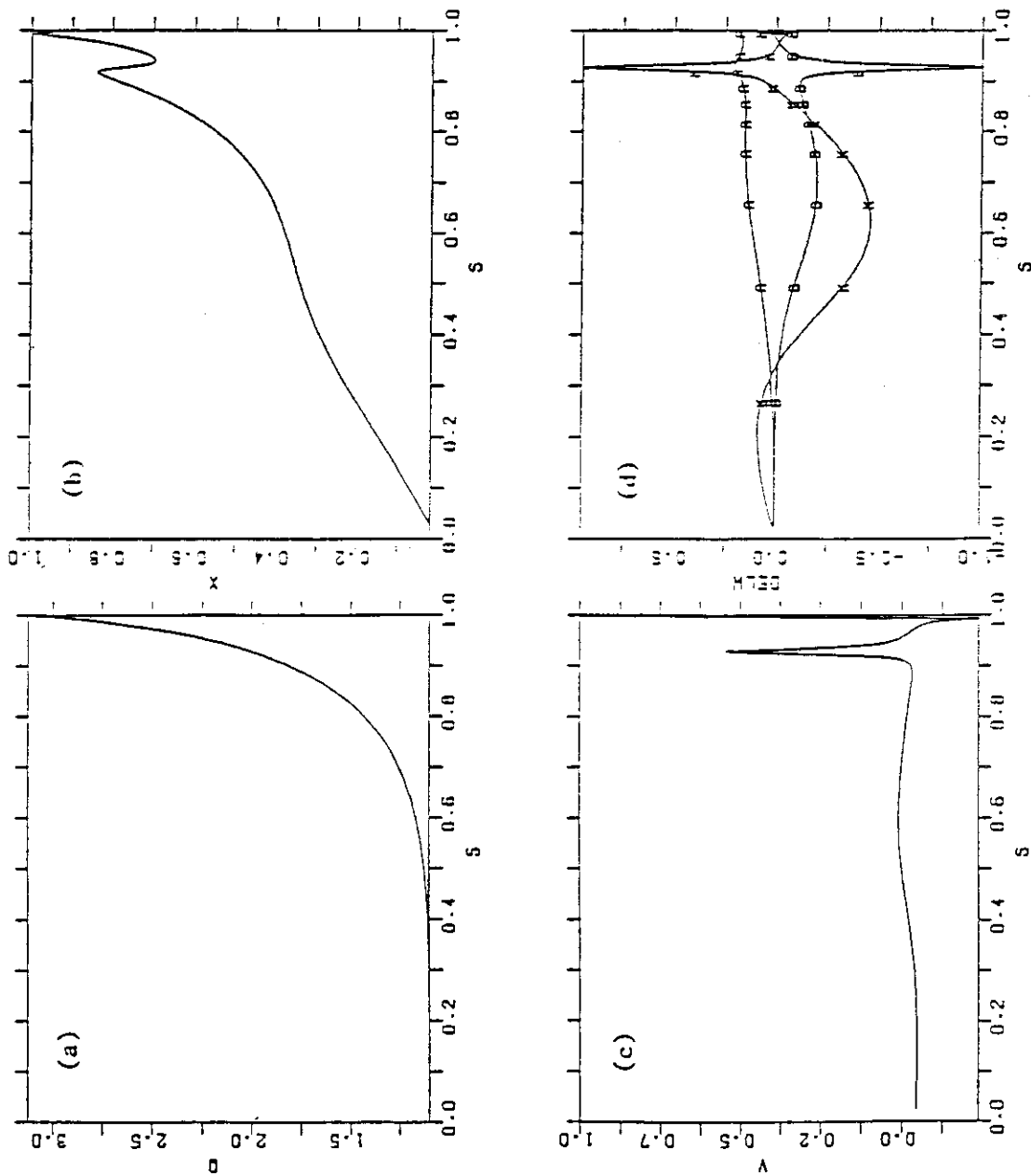


Fig. 2.6 Mode structure of a weakly unstable $n=1$ kink mode for the equilibrium Data 1. $\beta_t=4.00\%$ and $\gamma^2=1.16 \times 10^{-4}$.

NUMER= 27
 BETA-T= 4.80008
 BETA-M= 6.15306
 BETA-P= 2.39447
 O-AXIS= 1.10055
 O-SURF= 3.12404
 ASPECT= 3.96580
 ELLIPT= 1.60555
 TRIG = 0.29909

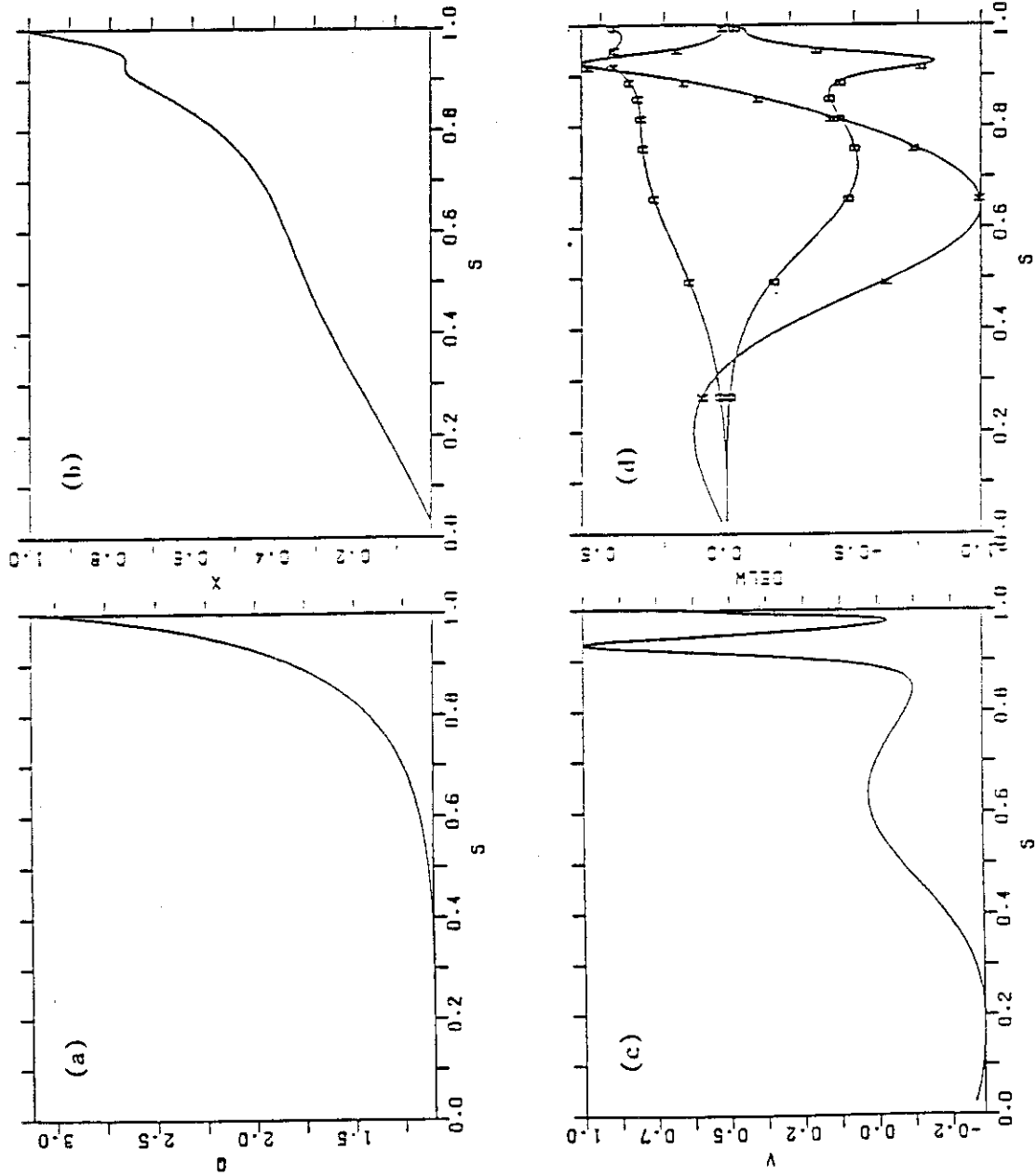


Fig. 2.7 Mode structure of an unstable $n=1$ kink mode for the equilibrium
 Data 1. $\beta_t=4.80\%$ and $\gamma^2=3.23 \times 10^{-3}$.

NUMER= 21
 BETA-T= 4.12002
 BETA-X= 4.91181
 BETA-P= 2.10580
 Q-AXIS= 1.10020
 Q-SURF= 3.12554
 ASPECT= 3.96726
 ELLIPT= 1.60586
 TRIG = 0.29821

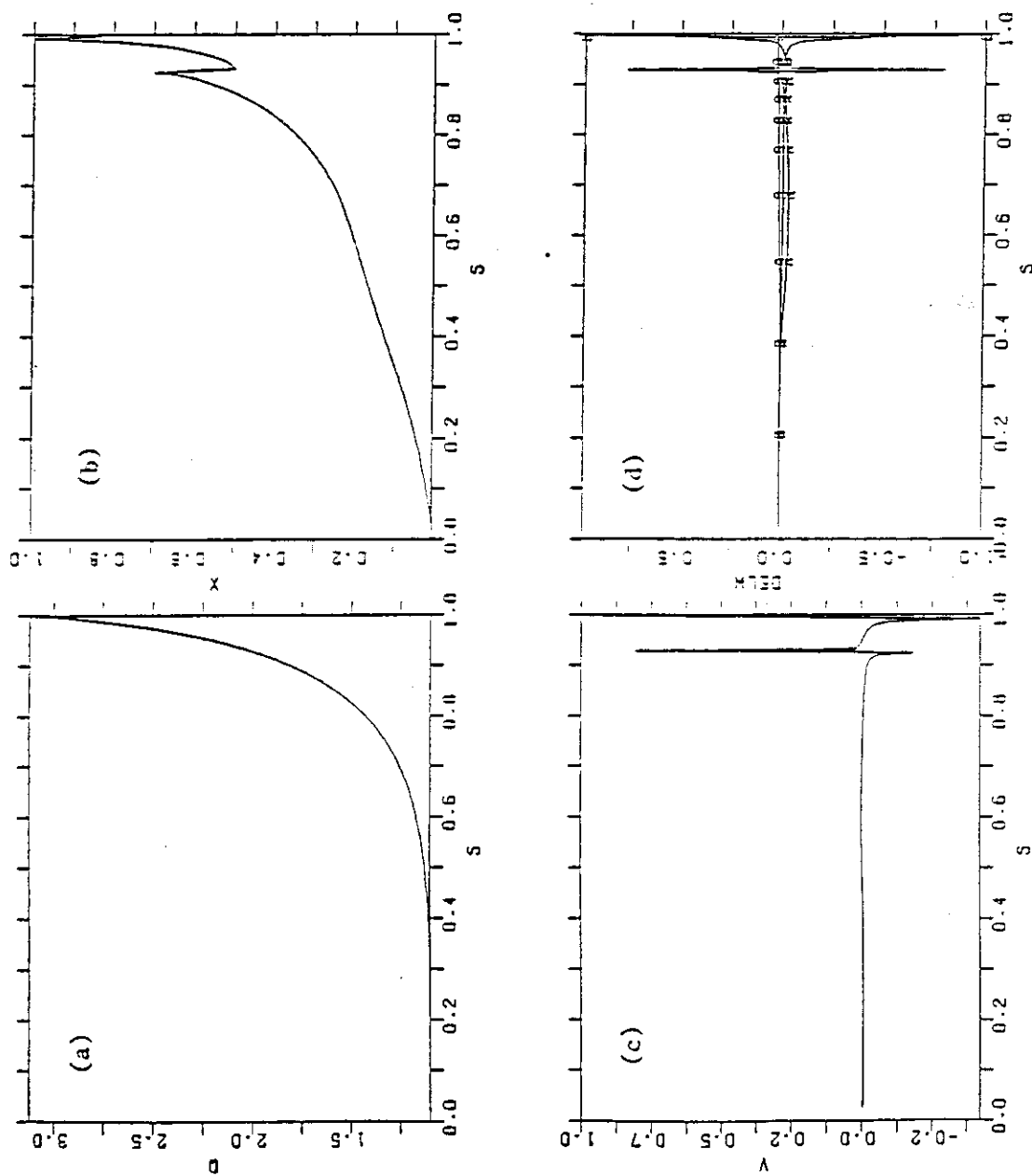


Fig. 2.8 Mode structure of a stable $n=1$ kink mode for the equilibrium
Data 2 $\beta_t=4.12\%$ and $\gamma^2=8.91 \times 10^{-6}$.

```

NUMEQU= 22
BETA-T= 4.31203
BETA-M= 5.14513
BETA-P= 2.19201
Q-AXIS= 1.10079
Q-SURF= 3.12829
ASPECT= 3.96575
ELLIPT= 1.60571
TRIG = 0.29778

```

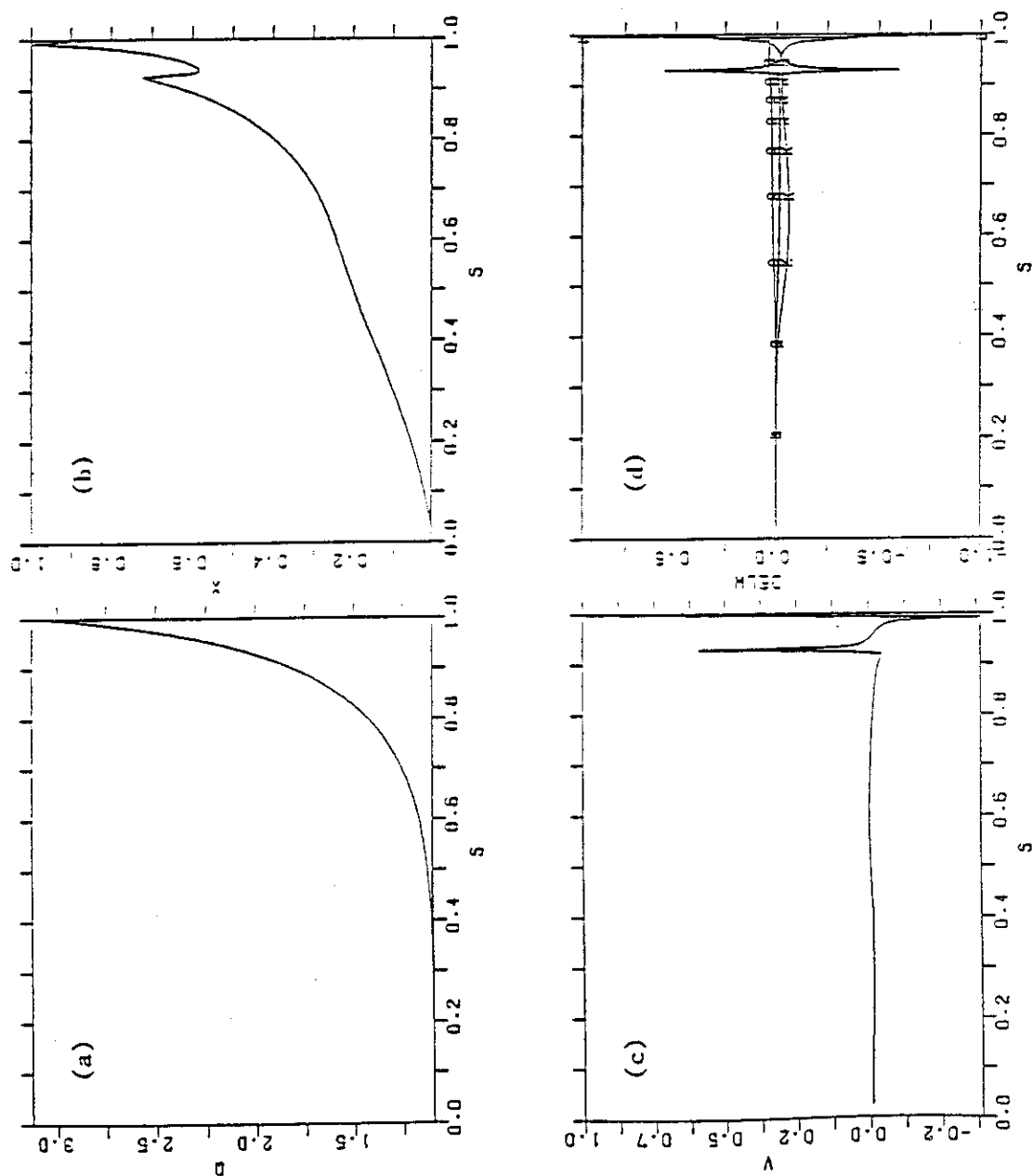


Fig.2.9 Mode structure of a weakly unstable $n=1$ kink mode (near beta limit) for the equilibrium Data 2. $\beta_1=4.31\%$ and $\gamma^2=2.24 \times 10^{-5}$

NUMERU= 17
 BETA-T= 3.34150
 BETA-X= 4.07283
 BETA-P= 1.86965
 Q-AXIS= 1.10224
 Q-SURF= 3.19984
 ASPECT= 3.97426
 ELLIPT= 1.60511
 TRIG = 0.30255

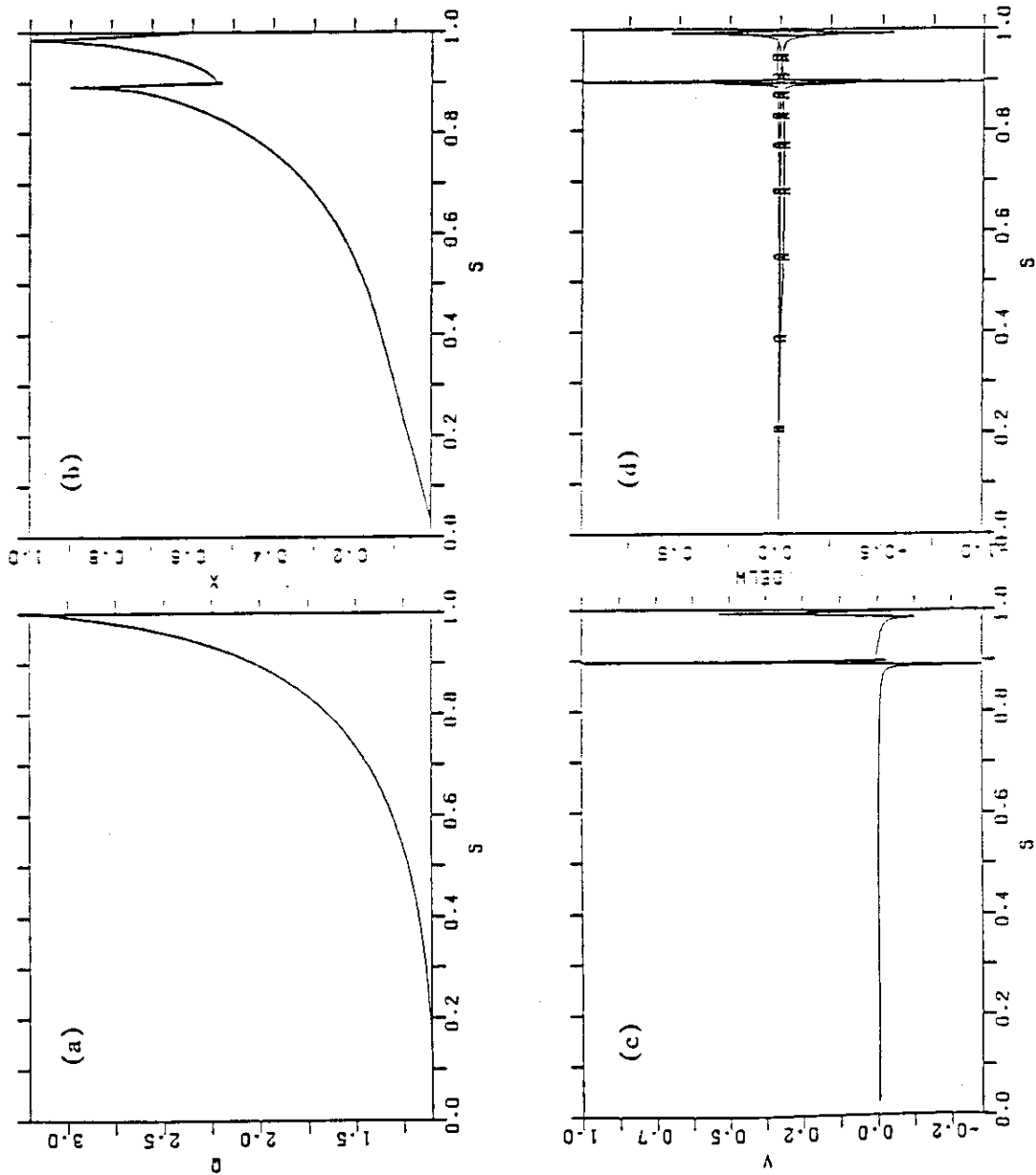


Fig. 2.10 Mode structure of a stable $n=1$ kink mode for the equilibrium Data 3, $\beta_t=3.34\%$ and $\gamma^2=4.00 \times 10^{-6}$.

```

NUMEQU= 18
BEIA-T= 3.53443
BEIH-M= 4.31132
BEIA-P= 1.96360
Q-AXIS= 1.10267
Q-SURF= 3.20155
ASPECT= 3.97288
ELLIPT= 1.60496
TRIG = 0.30222

```

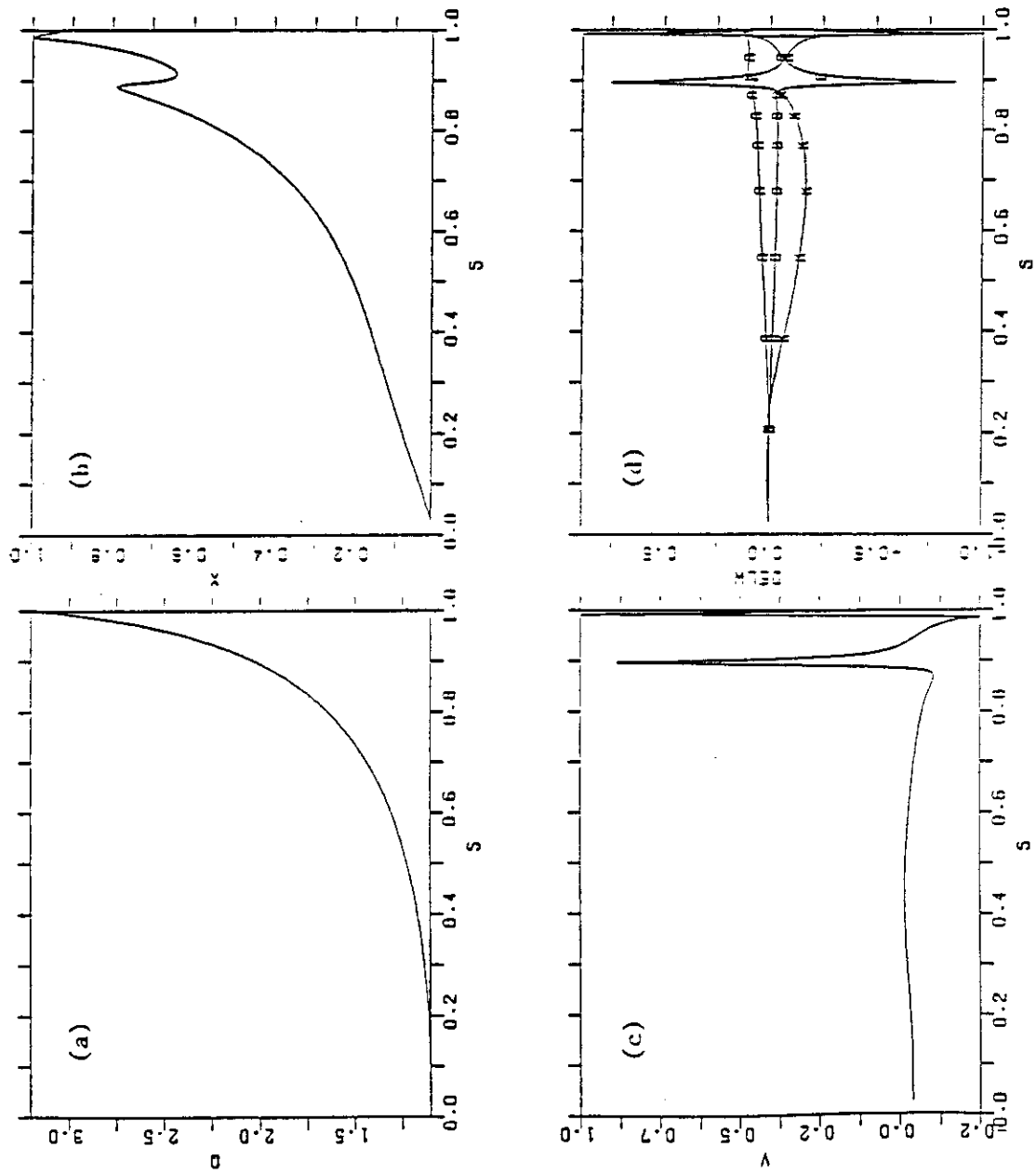


Fig. 2.11 Mode structure of a weakly unstable $n=1$ kink mode for the equilibrium data 3. $\beta_t = 3.51\%$ and $\gamma^2 = 4.24 \times 10^{-5}$.

NUMER = 16
 BETA-T = 3.14259
 BETA-W = 3.96798
 BETA-P = 1.77262
 O-AXIS = 1.10263
 O-SURF = 3.19798
 ASPECT = 3.97620
 ELLIPT = 1.60517
 TRIG = 0.30373

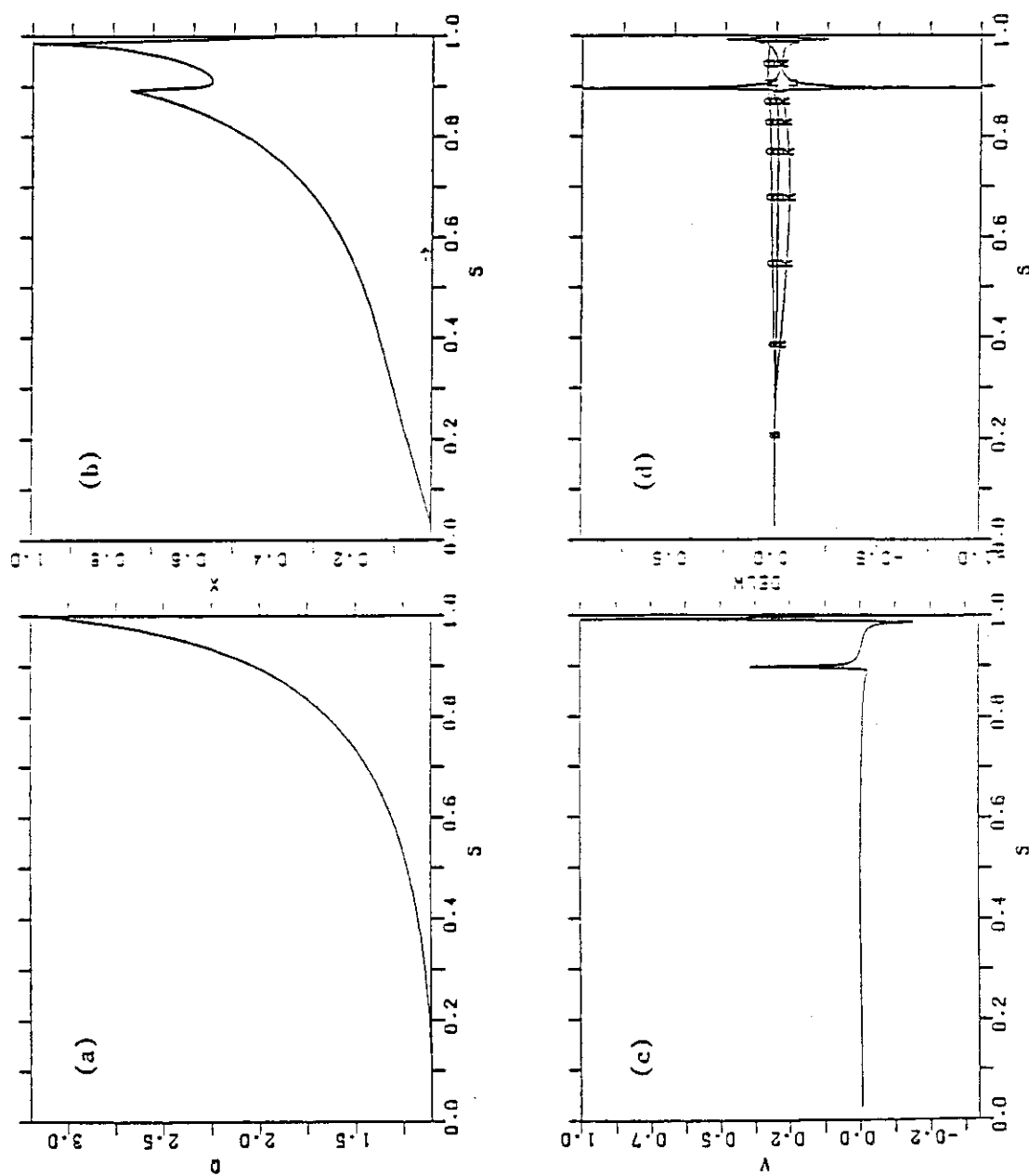


Fig.2.12 Mode structure near beta limit for the equilibrium Data 4.
 $\beta_t = 3.14\%$ and $\gamma^2 = 9.45 \times 10^{-6}$.

NUMEQU= 17
 DETR-T= 3.33570
 DETR-W= 4.21575
 DETR-P= 1.86633
 Q-AXIS= 1.10249
 Q-SURF= 3.19775
 ASPECT= 3.97516
 ELLIPT= 1.60502
 TRI0 = 0.30363

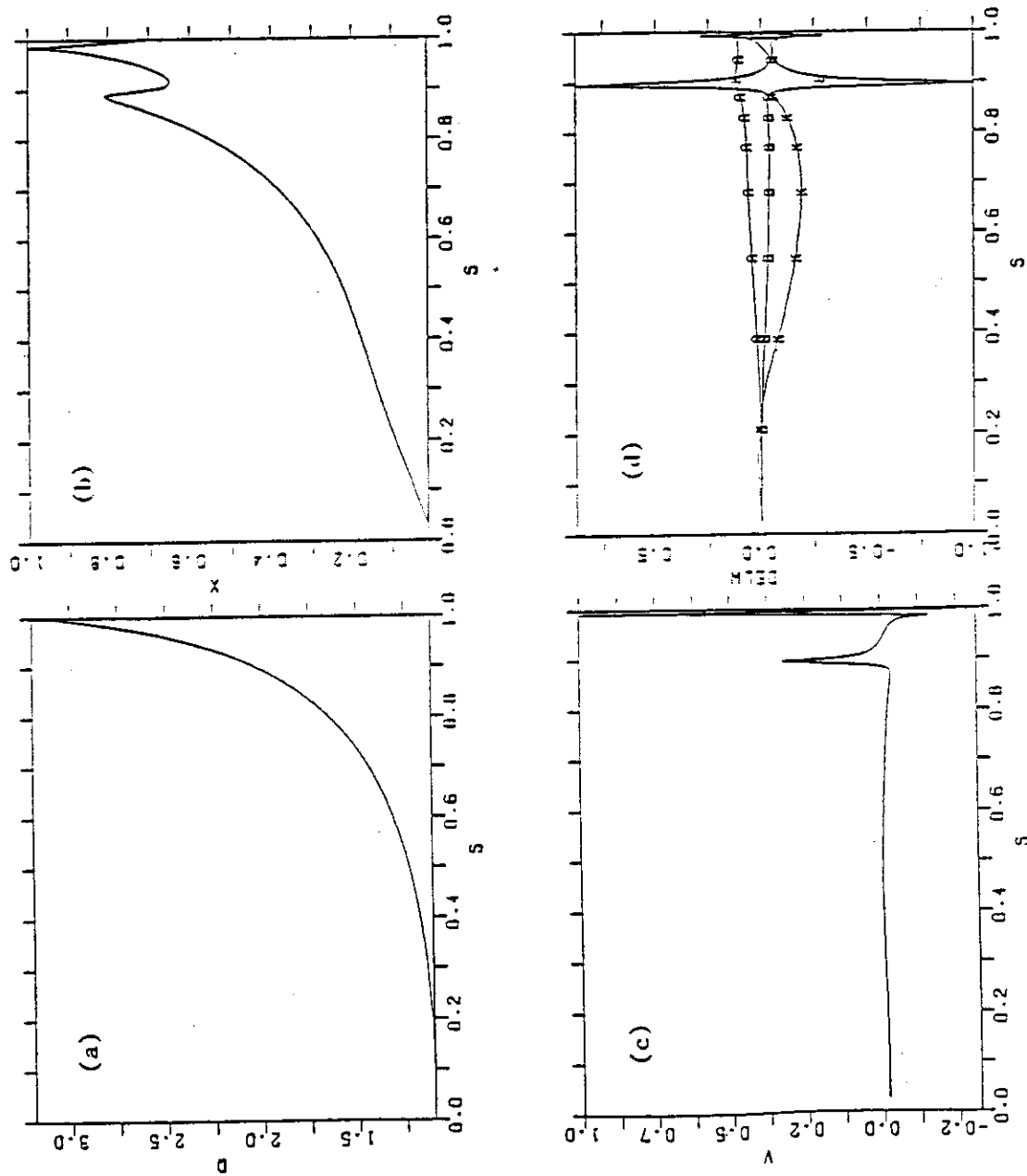


Fig.2.13 Mode structure of a weakly unstable $n=1$ kink mode for the equilibrium Data 4. $\beta_1=3.34\%$ and $\gamma^2=4.53 \times 10^{-5}$.

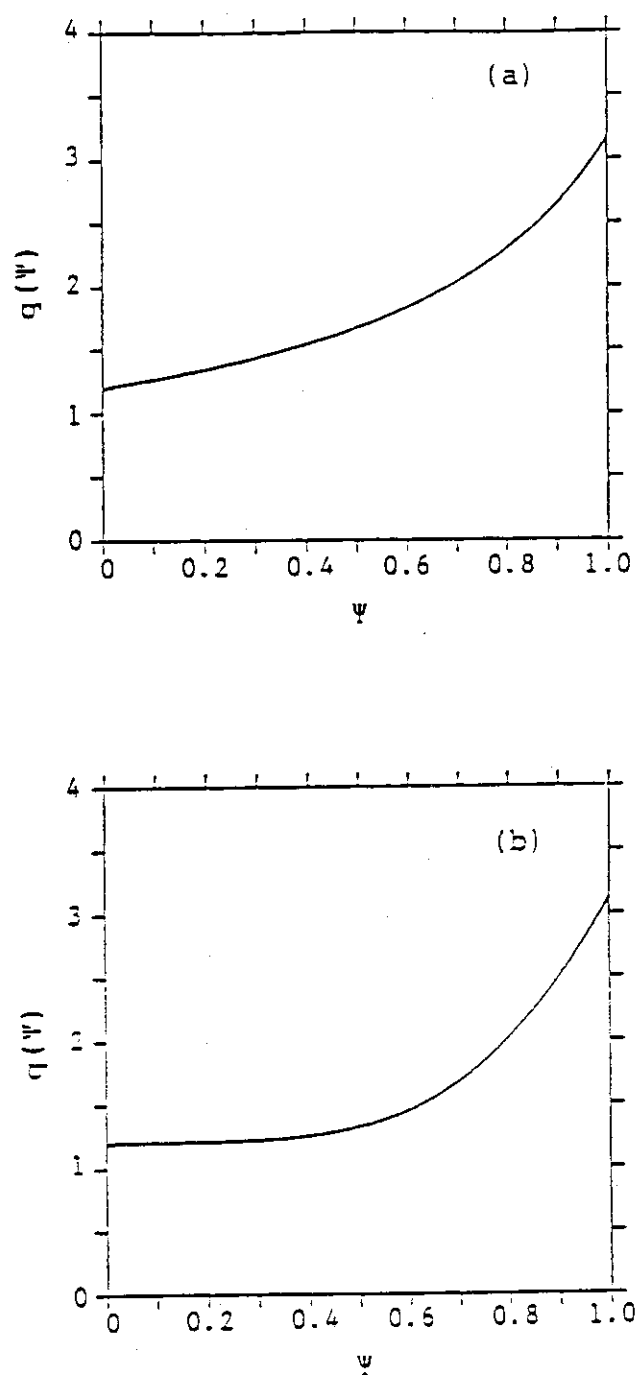


Fig.2.14 Profile of safety factor as the function of $\bar{\psi}$, for $q_0=1.2$, $q_s=3.1$, $A=3$, $\kappa=1$ and $\delta=0$. Figs.(a) and (b) correspond to the case 1 ($S_w=0.23$) and the case 2 ($S_w=0.05$), respectively, where $S_w=(q(\bar{\psi}=0.5)-q_0)/(q_s-q_0)$.

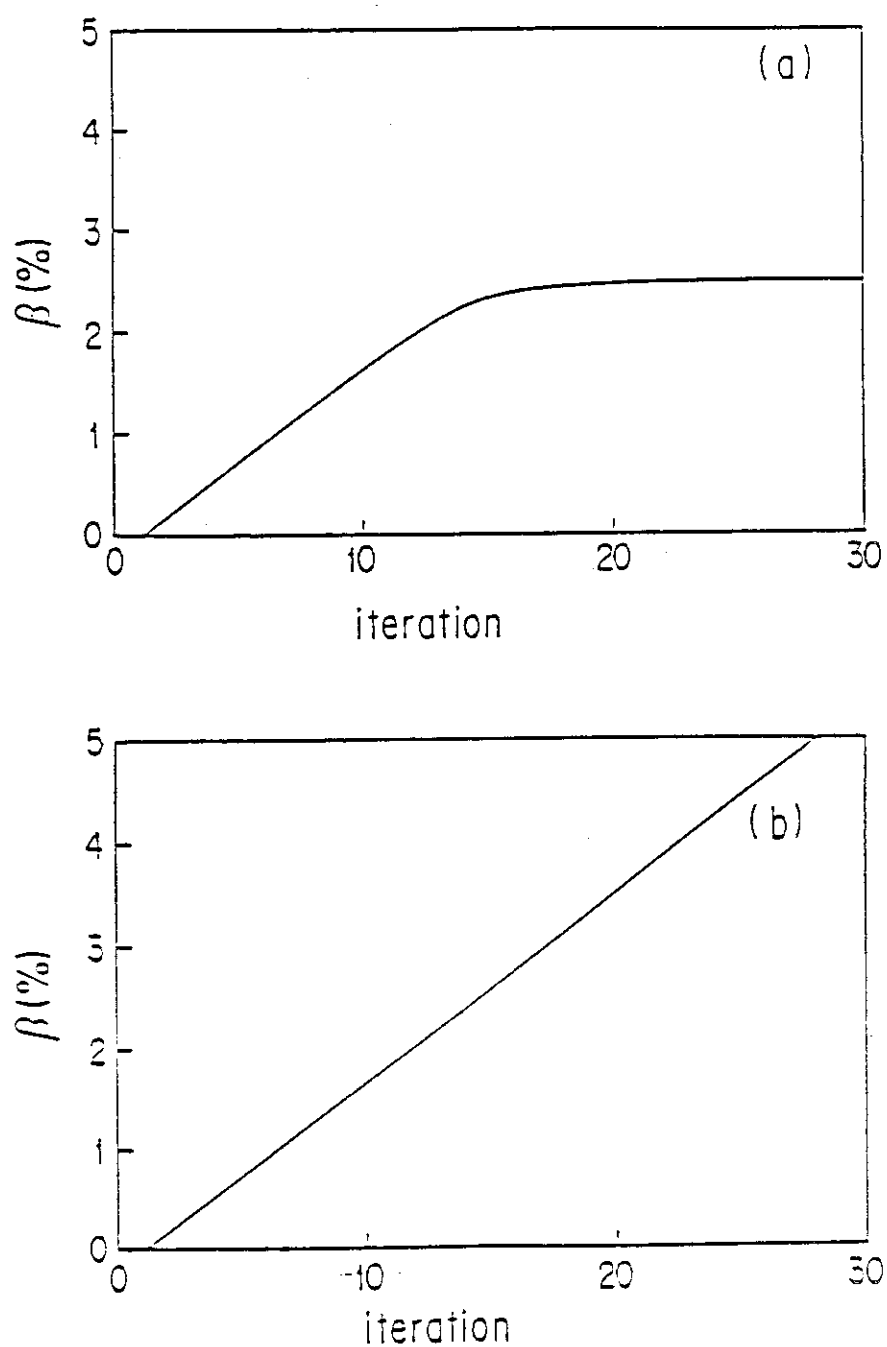


Fig.2.15

β_t vs. iteration number. Figs.(a) and (b) correspond to the case 1 ($S_o=0.23$) and the case 2 ($S_o=0.05$), respectively. For the case 1, the beta value saturates at the beta limit.

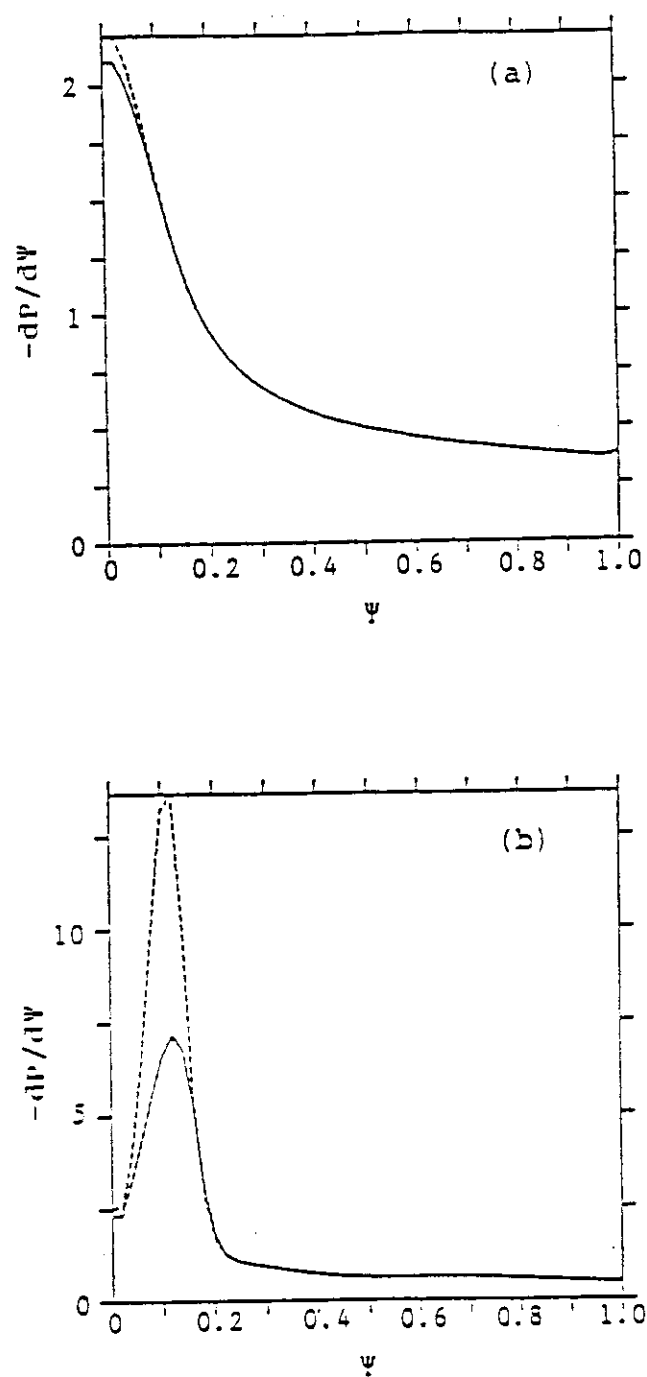
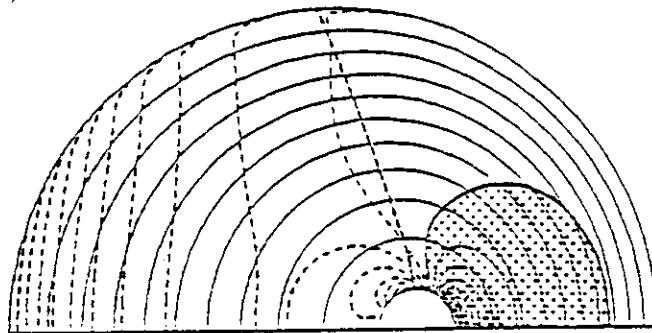


Fig.2.16

The pressure gradient as the function of $\bar{\psi}$ (a) for case 1 and (b) case 2. The broken line denotes the marginal pressure gradient to the ballooning modes.

(a)



(b)

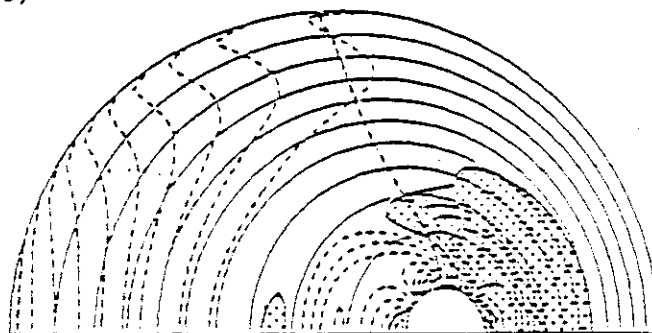


Fig.2.17

Contours of $\kappa_{\perp}=0$ (bold broken line) and local shear, S_v , (a) for case 1 and (b) case 2. In the shaded region, $S_v < 0$.

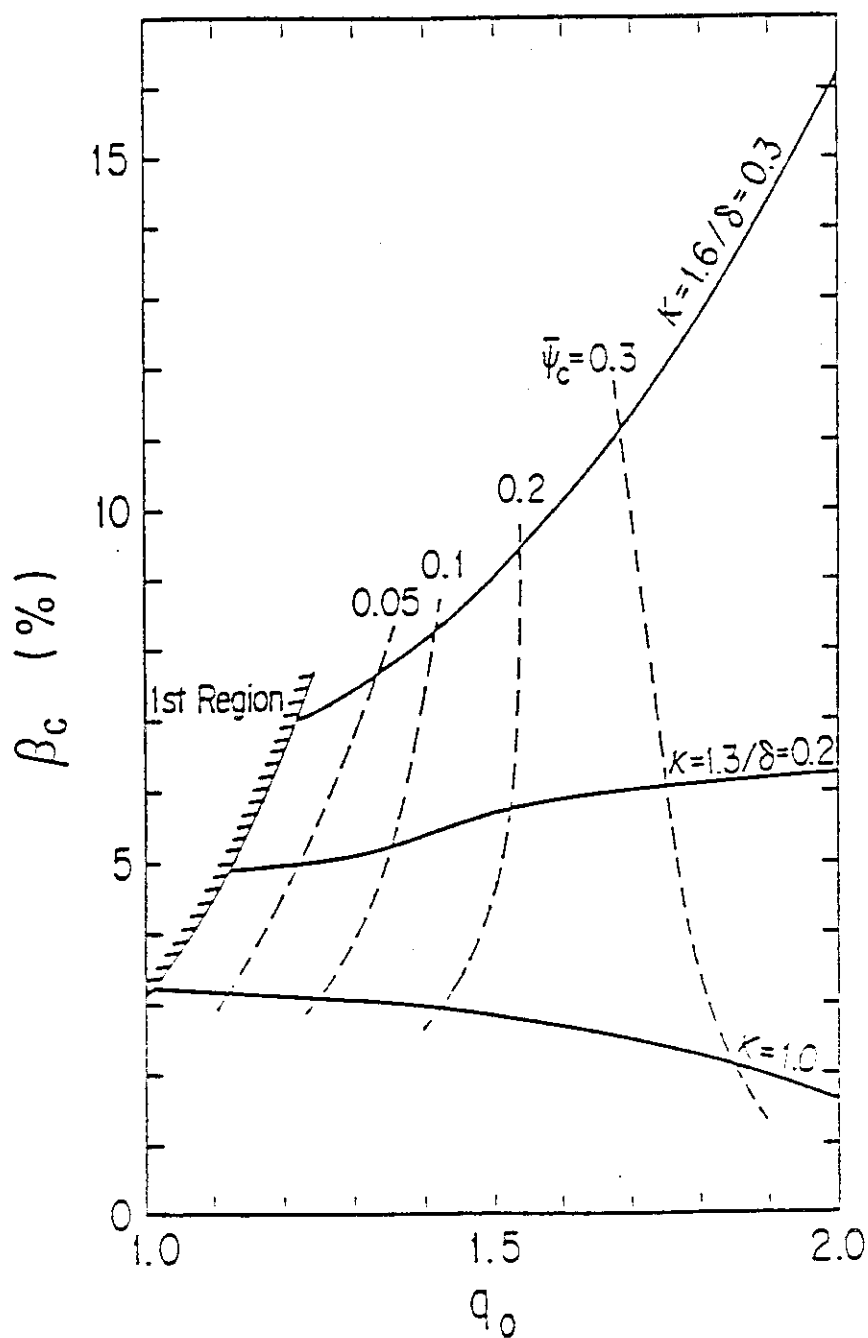


Fig.2.18

Transition beta value vs. q_0 for $\kappa/\delta = 1.0/0.0$, $1.3/0.2$ and $1.6/0.3$.

Other parameters are $q_s=3.1$, $S_w=0.15$, $A=3$. The broken lines show the boundary flux of the second stability region, $\bar{\psi}_c$, within which a plasma has the capability to maintain the unlimited pressure.

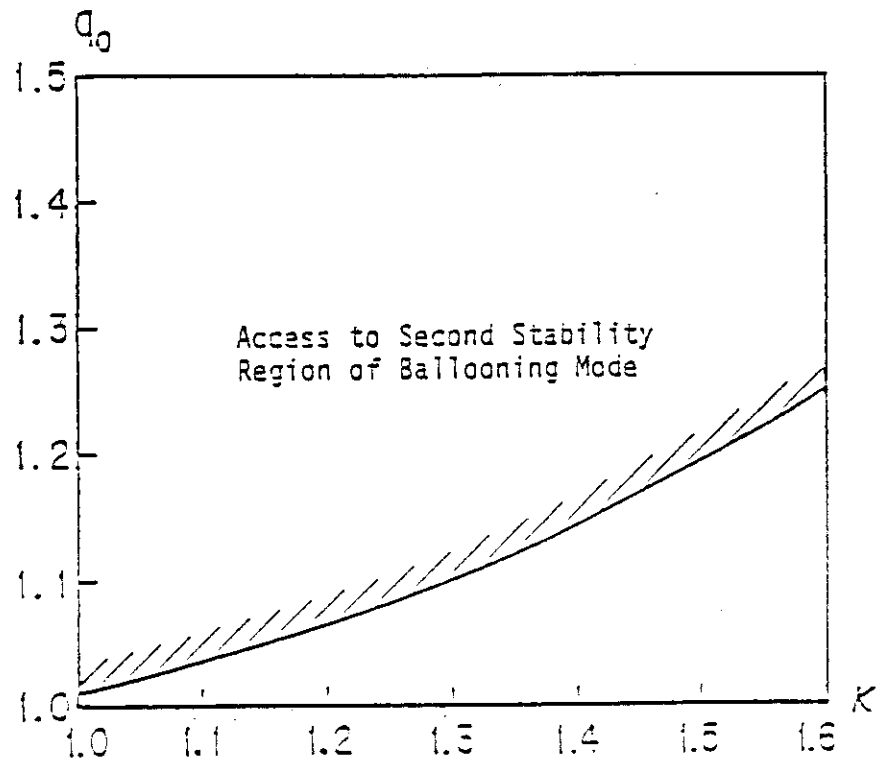


Fig.2.19

Critical q_0 vs. κ for the access to the second stability region of ballooning modes.

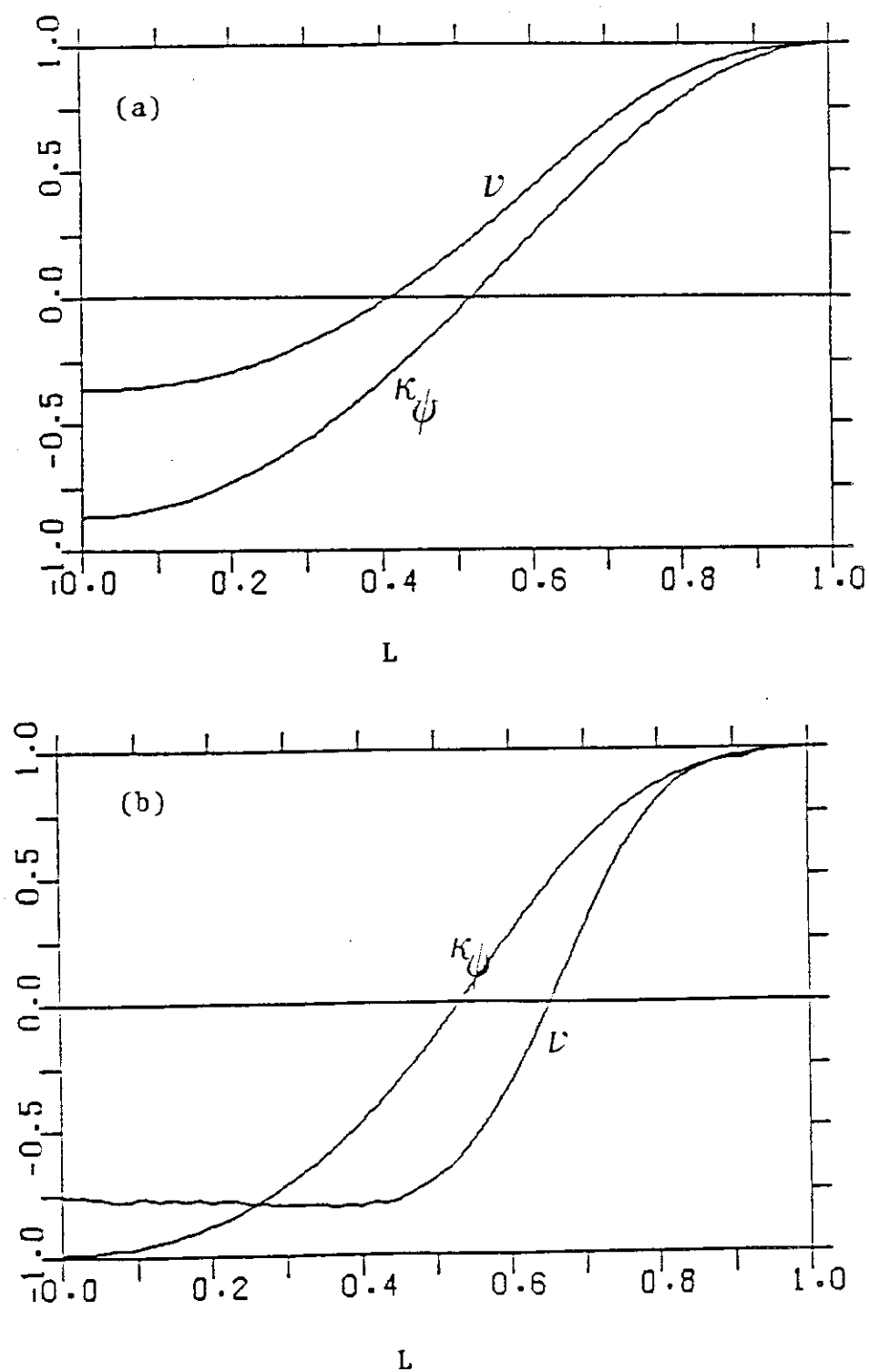


Fig.2.20 Local shear, ν , and normal curvature, κ_ψ , vs. length of field line, l on the flux surface within which second stability access is possible for (a) $\kappa=1$, $\delta=0$, $\beta_J=0.1$, $\beta=0.15\%$, (b) $\kappa=1$, $\delta=0$, $\beta_J=1.5$, $\beta=3.16\%$, (c) $\kappa=1.6$, $\delta=0.3$, $\beta_J=0.1$, $\beta=0.36\%$, and (d) $\kappa=1.6$, $\delta=0.3$, $\beta_J=1.4$, $\beta=7.4\%$. The profile of safety factor is chosen as $q_0=1.5$, $q_s=3.1$ and $S_v=0.15$.

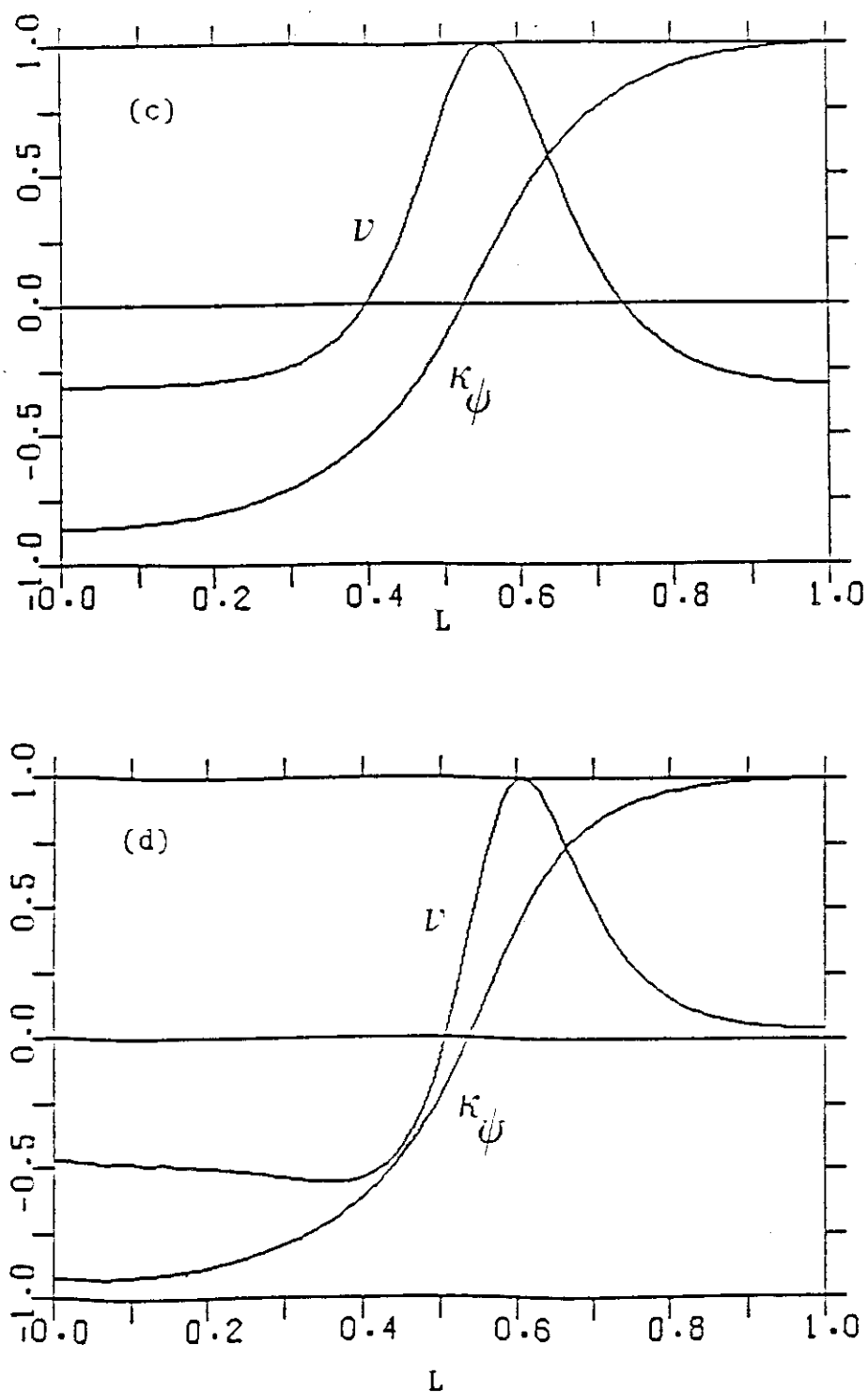


Fig.2.20 Local shear, ν , and normal curvature, κ_ψ , vs. length of field line, l on the flux surface within which second stability access is possible for (a) $\kappa=1$, $\delta=0$, $\beta_J=0.1$, $\beta=0.15\%$, (b) $\kappa=1$, $\delta=0$, $\beta_J=1.5$, $\beta=3.16\%$, (c) $\kappa=1.6$, $\delta=0.3$, $\beta_J=0.1$, $\beta=0.36\%$, and (d) $\kappa=1.6$, $\delta=0.3$, $\beta_J=1.4$, $\beta=7.4\%$. The profile of safety factor is chosen as $q_0=1.5$, $q_s=3.1$ and $S_w=0.15$.

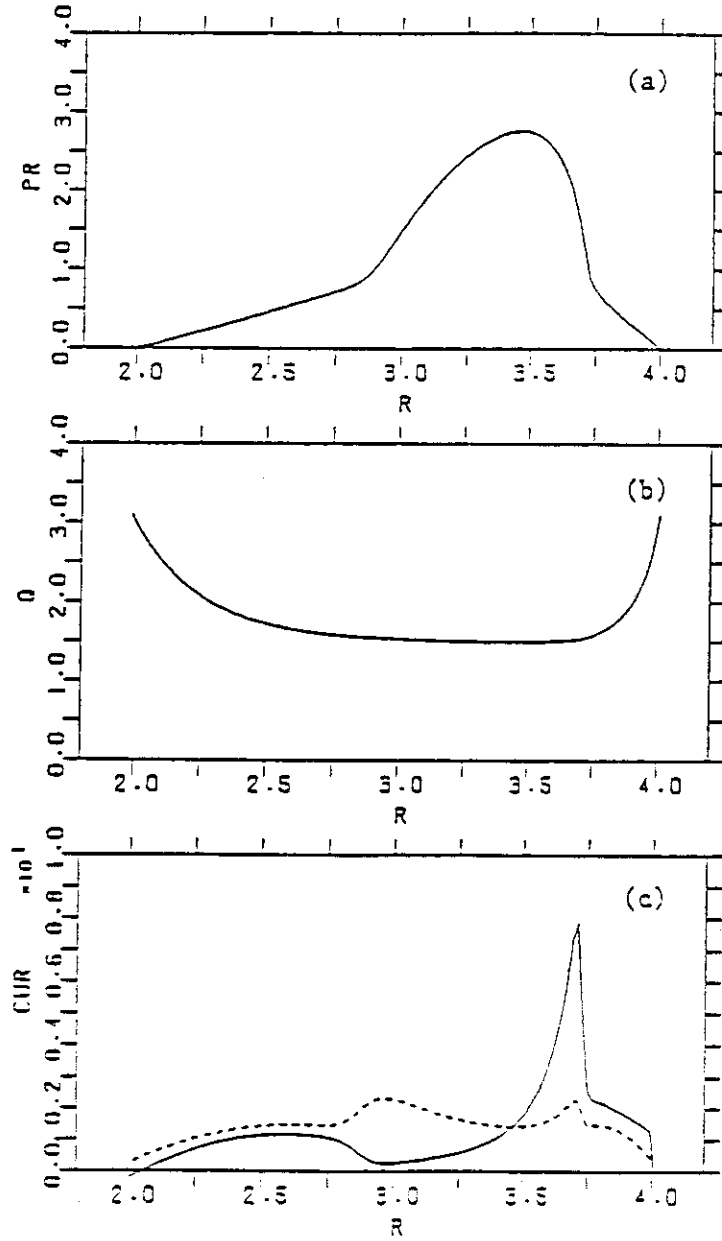


Fig.2.21

Profiles of (a) plasma pressure, (b) safety factor and (c) toroidal current in the equilibrium with $\beta_t=6.6\%$, $\kappa=1.3$, $\delta=0.2$, $A=3$, $q_0=1.5$, $q_s=3.1$ and $S_v=0.15$. The plasma is in a second stability region inside of $\bar{\psi}_c=0.2$. The broken line in Fig.6(c) shows the surface-averaged parallel current density, $j_{||}=\langle \bar{J} \cdot \bar{B} \rangle / \langle B_T \rangle$.

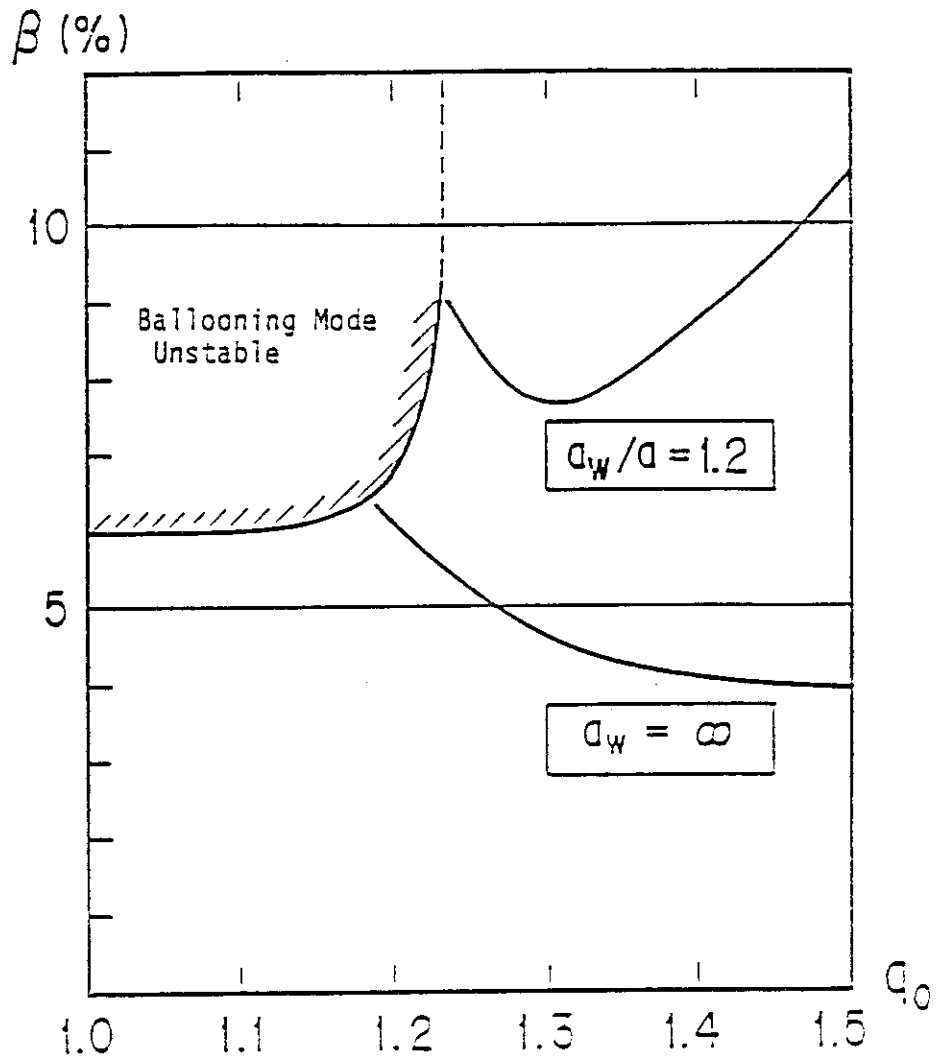


Fig.2.22

Beta limit of $n=1$ external kink modes vs. q_0 for $\kappa=1.6$, $\delta=0.3$, $A=3$ and $q_s \sim 3.1$. In the hatched region the ballooning modes are unstable.

```

NUMEQU= 23
BETA-T= 4.63120
BETA-W= 6.24785
BETA-P= 1.18509
Q-AXIS= 1.30126
Q-SURF= 3.09477
ASPECT= 2.99166
ELLIPT= 1.61216
TRIG = 0.30594
INTORE= -1.00000
REXT =1001.00000

```

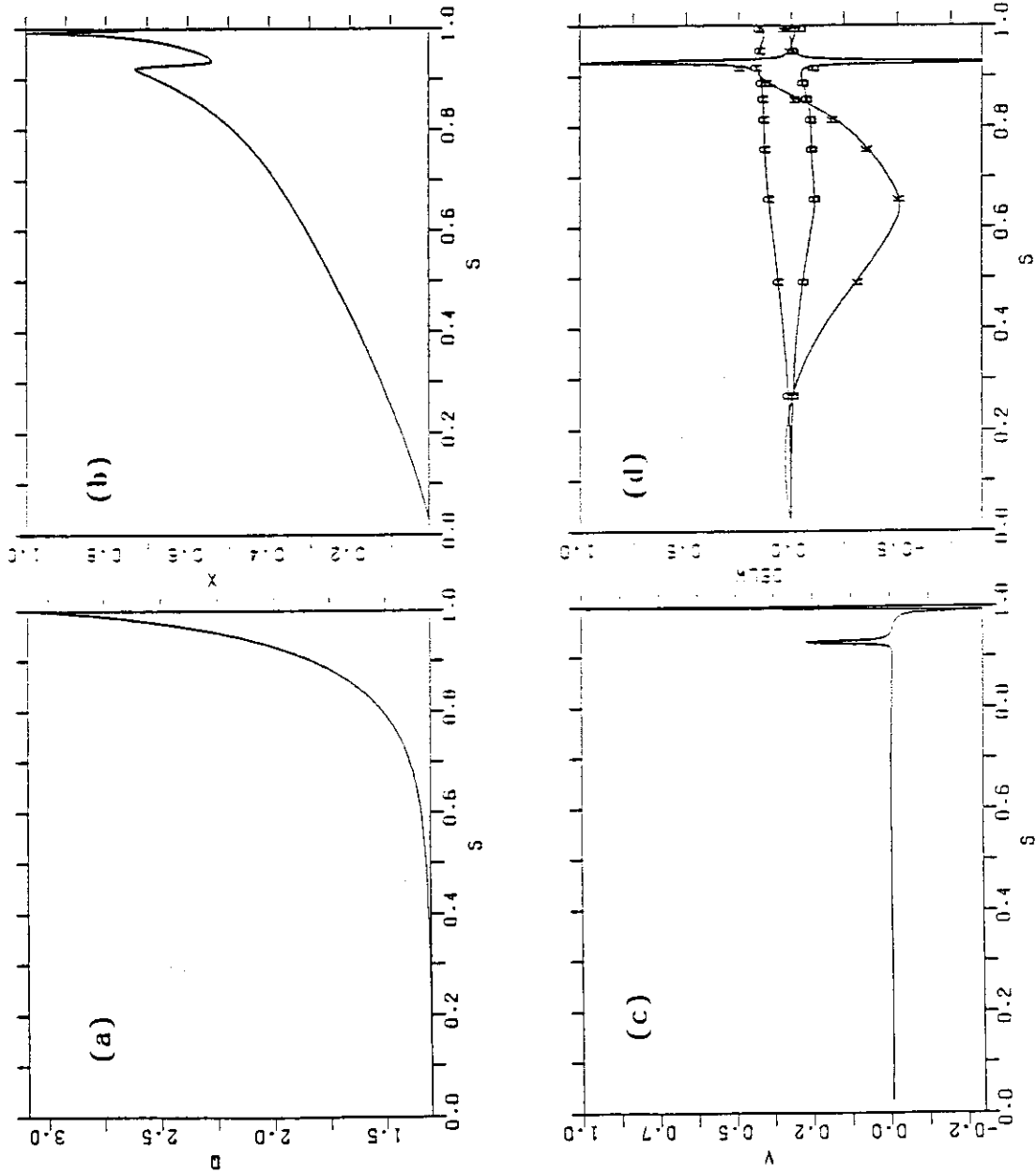


Fig.2.23 Mode structure of the unstable external kink mode for $a_w/r=0.05$, $q_0=1.3$, $q_s=3.1$, $S_w=0.05$; (a) $q(\sqrt{\psi})$, (b) radial eigenmode X , (c) poloidal eigenmode V and (d) potential energy.

```

NUMER= 20
BETA-T= 7.77326
BETA-W= 10.10161
BETA-P= 1.83315
Q-AXIS= 1.30085
Q-SURF= 3.09819
ASPECT= 2.98243
ELLIPT= 1.60923
TRIG= 0.31635
WNTORE= -1.00000
REXT= 1.20000

```

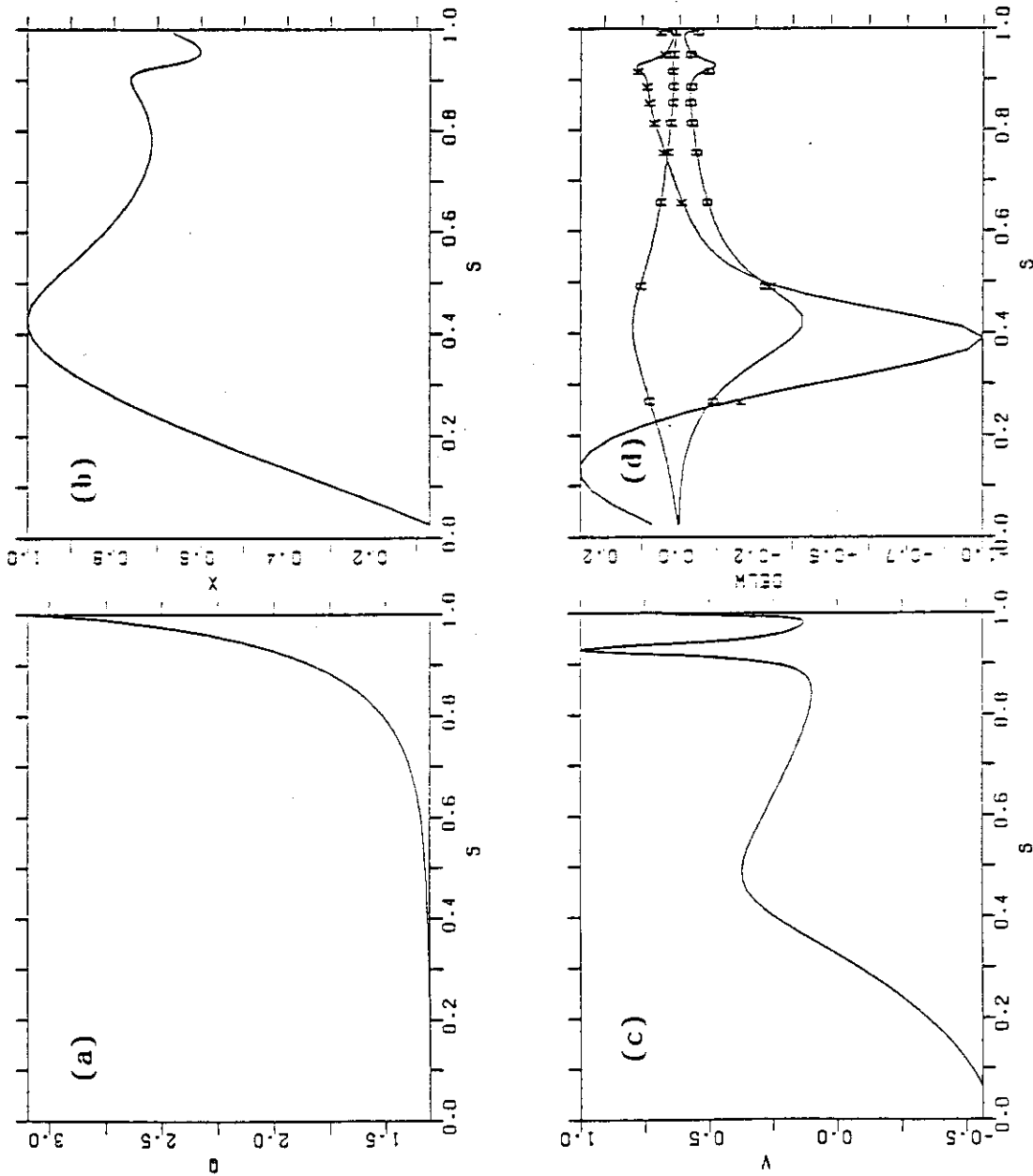


Fig.2.24 Mode structure of unstable external kink mode for $\alpha_w/\alpha=1.2$.

The dominant component is $m/n=1/1$.

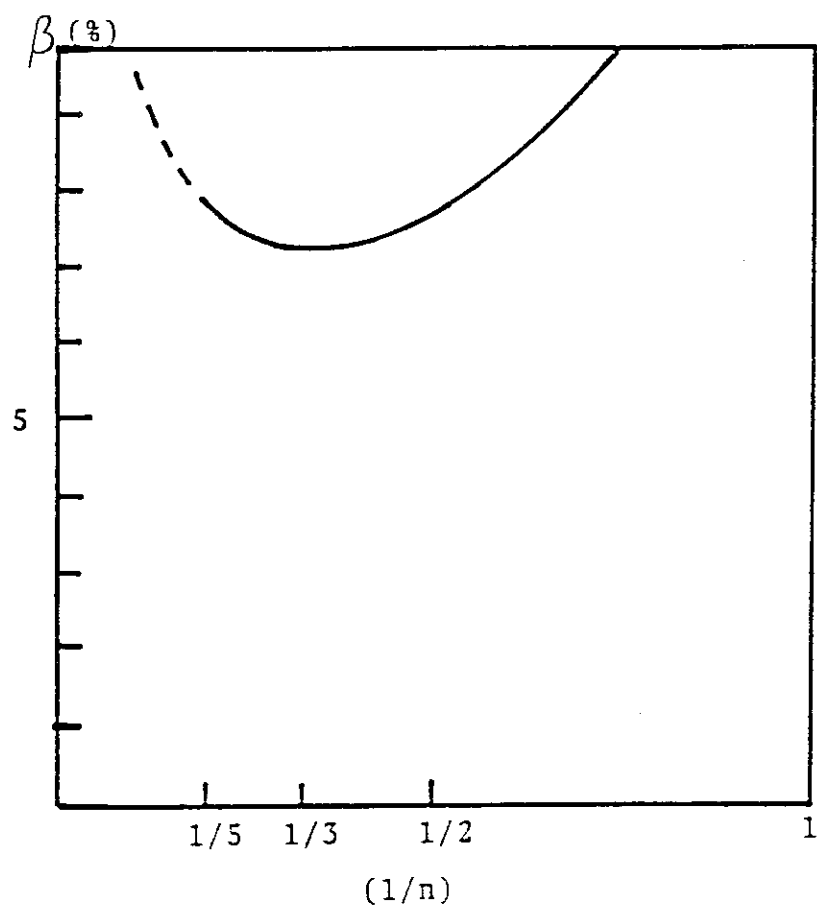


Fig.2.25 Beta limit of internal modes vs. n for $q_0=1.3$, $q_s=3.1$ and $S_p=0.05$.

```

NUMEQ= 21
BETA-T= 7.84058
BETA-W= 10.24501
BETA-P= 1.84587
O-AXIS= 1.30079
O-SURF= 3.09818
ASPECT= 2.98214
ELLIPT= 1.60920
TRI0 = 0.31612
WNIOR= -2.00000
WEXT = 0.0

```

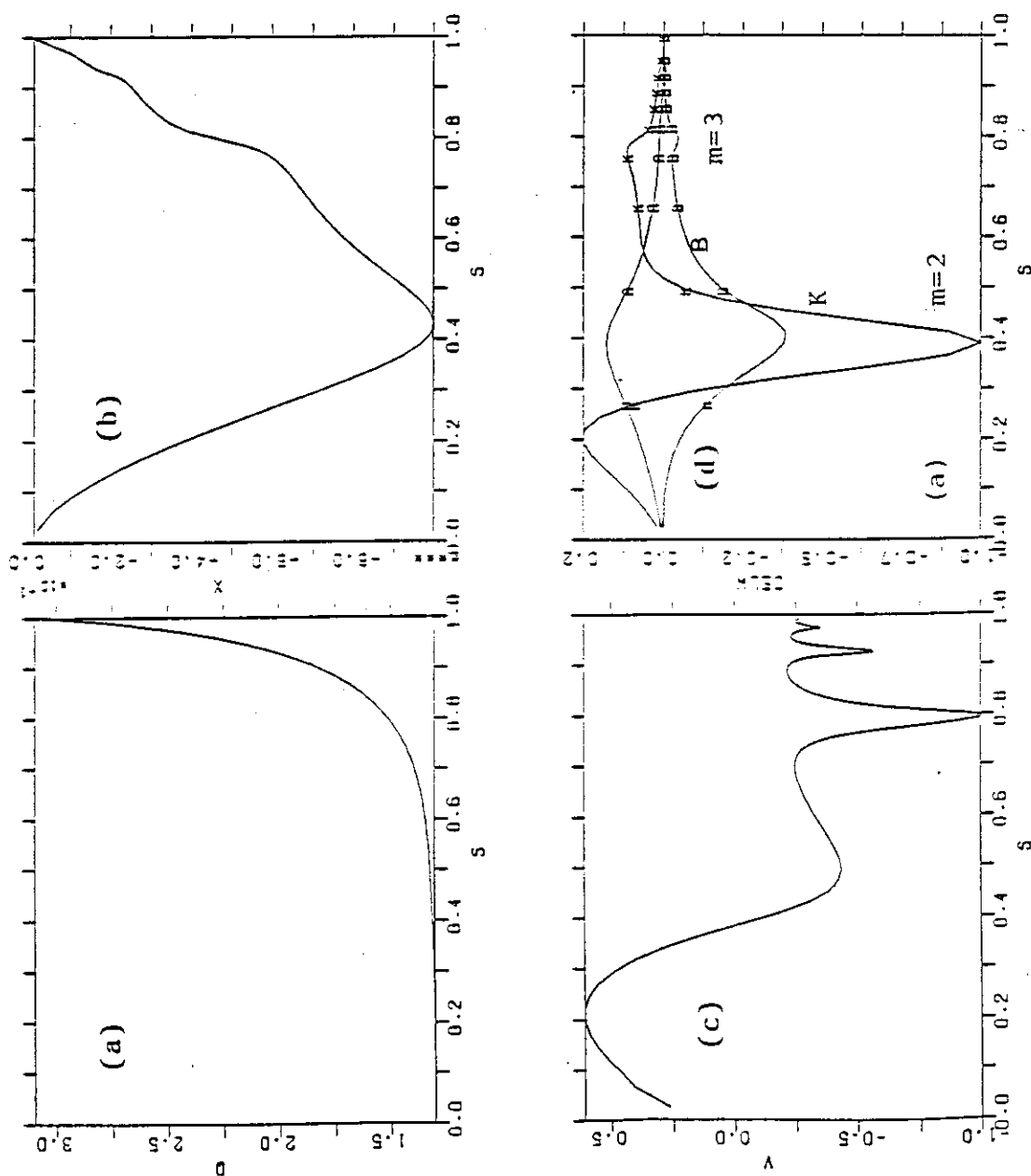


Fig.2.26 Mode structure of unstable $n=2$ internal mode.


```

NUMEQU= 16
BETA-T= 7.54847
BETA-K= 9.64838
BETA-P= 1.79058
O-AXIS= 1.30107
O-SURF= 3.09808
ASPECT= 2.98332
ELLIPT= 1.60934
TRIG = 0.29844
WNTORE= -3.00000
REXT = 0.0

```

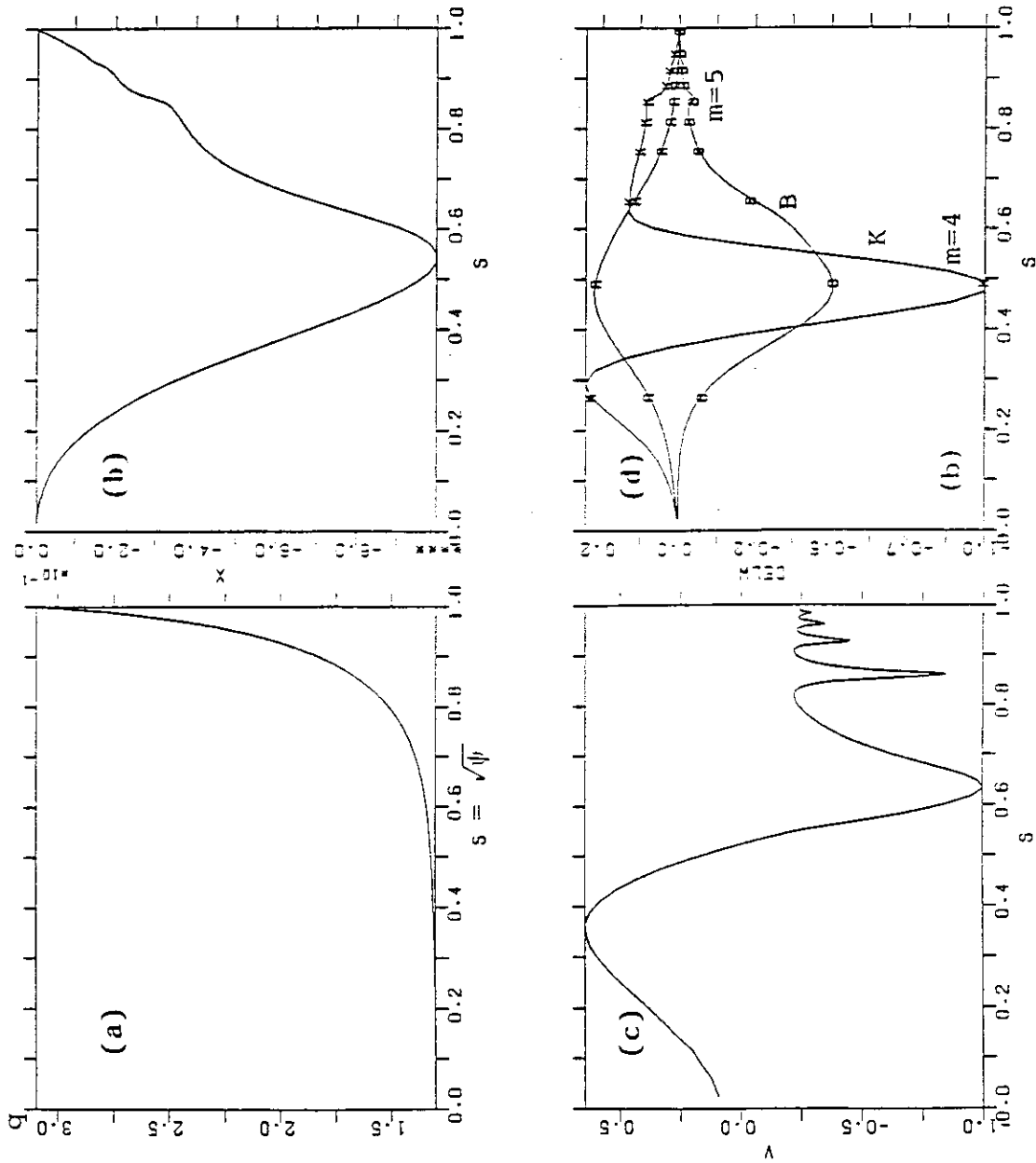


Fig.2.27 Mode structure of unstable $n=3$ internal mode.

NUMER= 20
BETA-T= 7.77326
BETA-W= 10.10161
BETA-P= 1.83315
Q-AXIS= 1.30085
Q-SURF= 3.09819
ASPECT= 2.98243
ELLIPT= 1.60923
TRIG = 0.31635

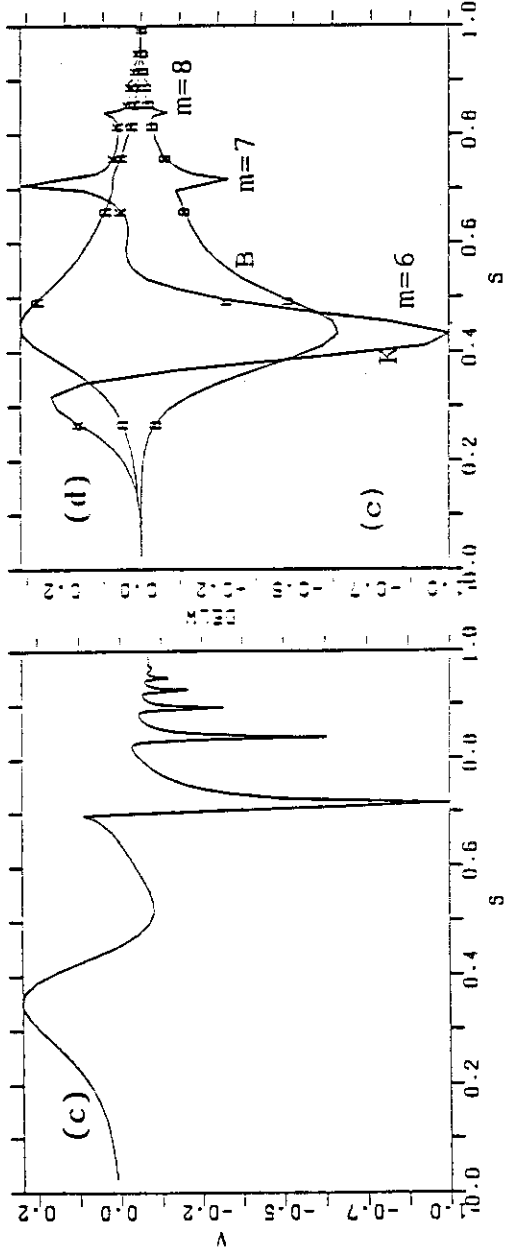
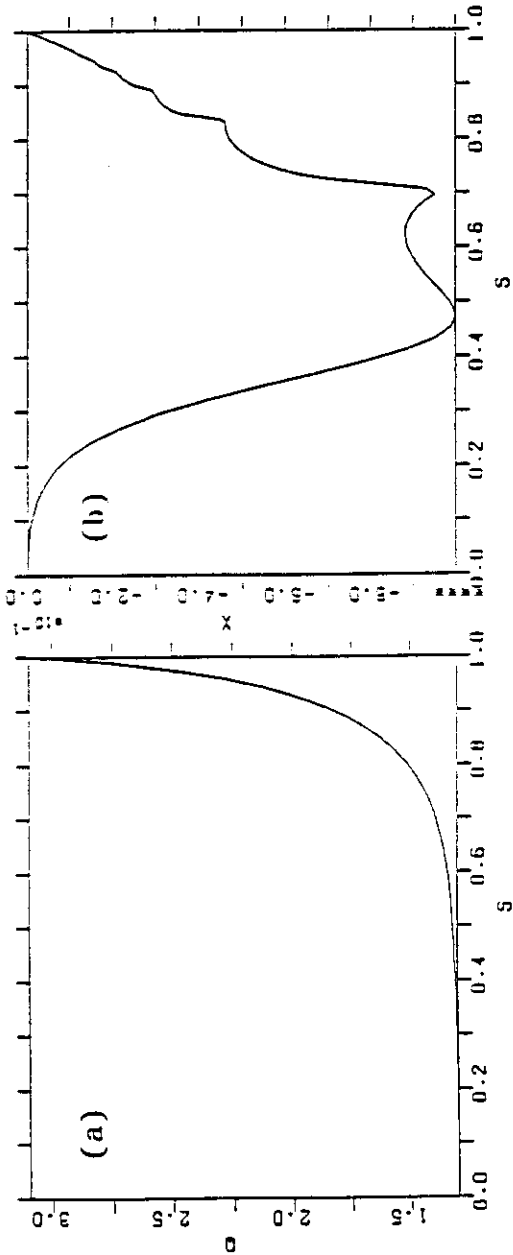


Fig.2.28 Mode structure of unstable $n=5$ internal mode.

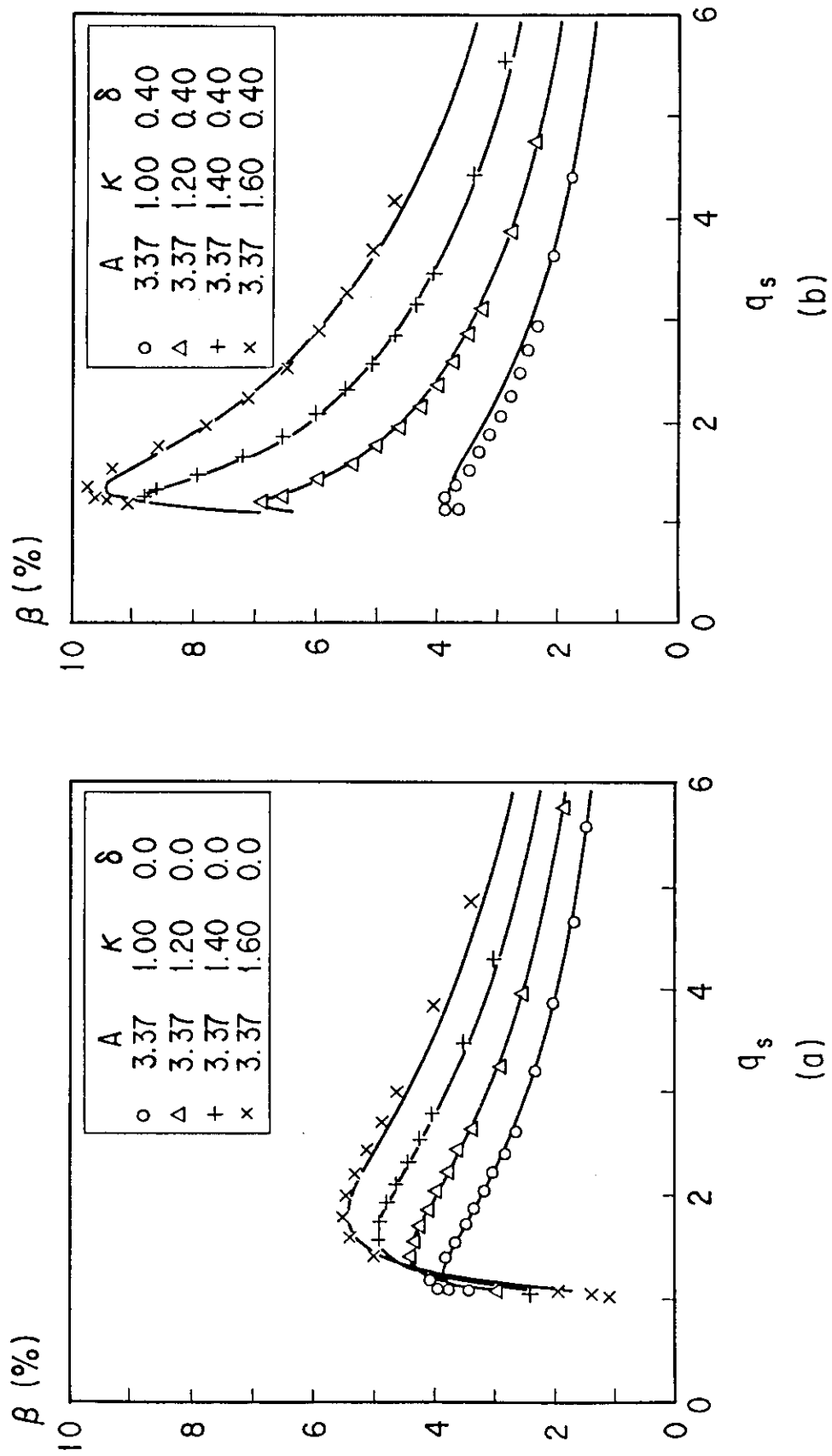


Fig.2.29 Beta limit due to ballooning mode vs. q_s for (a) $\delta=0$ and (b) 0.4 .

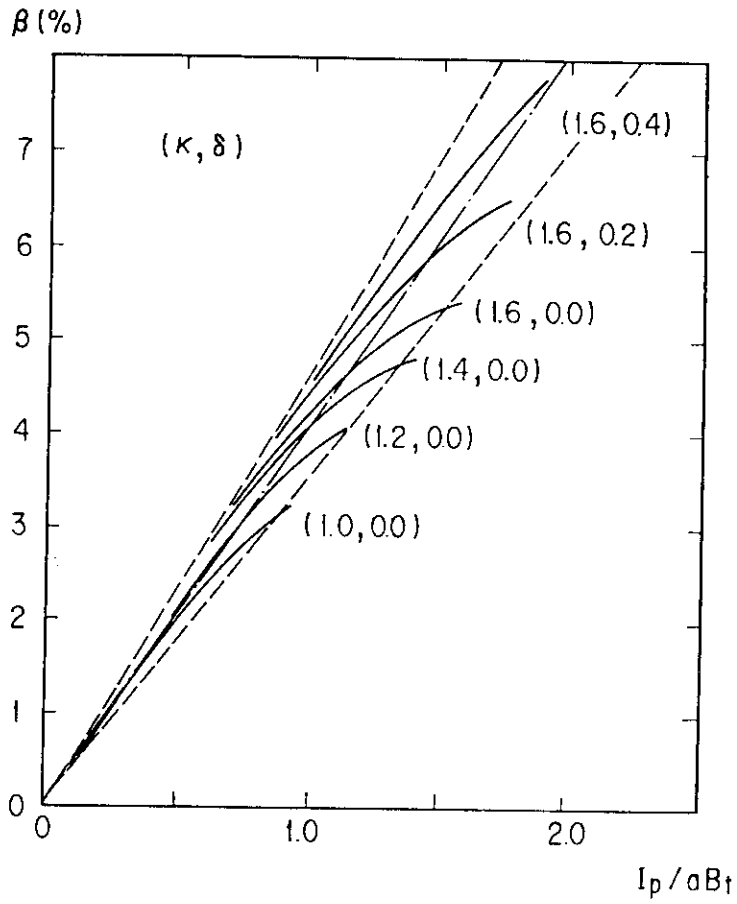


Fig.2.30 Beta limit due to ballooning mode vs. $I_N = I_p(MA) / a(m)B_T(T)$.

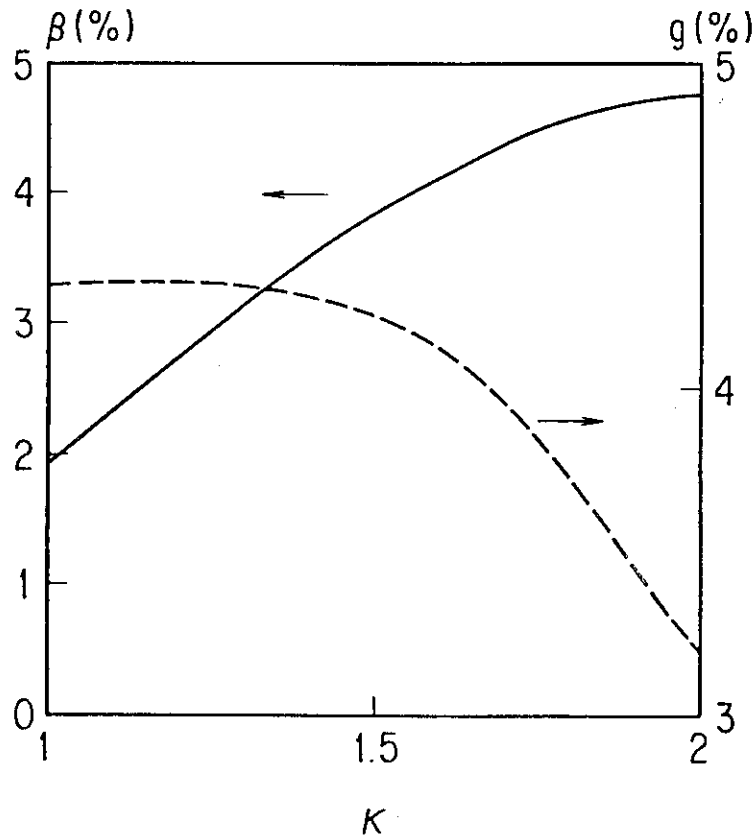


Fig.2.31 Beta limit vs. κ for $A=4$, $q_s=3$ and $\delta=0.3$.

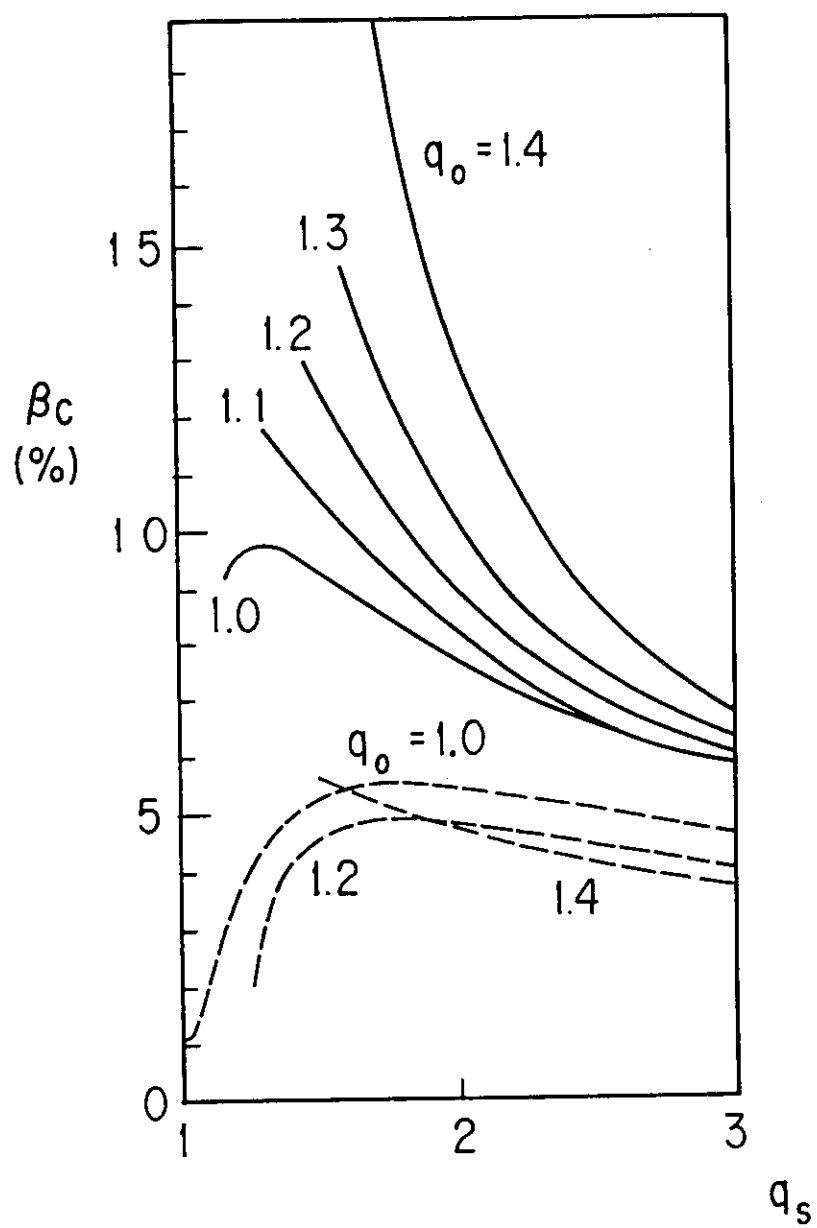


Fig.2.32 Dependence of beta limit on q_s for different value of q_0 .

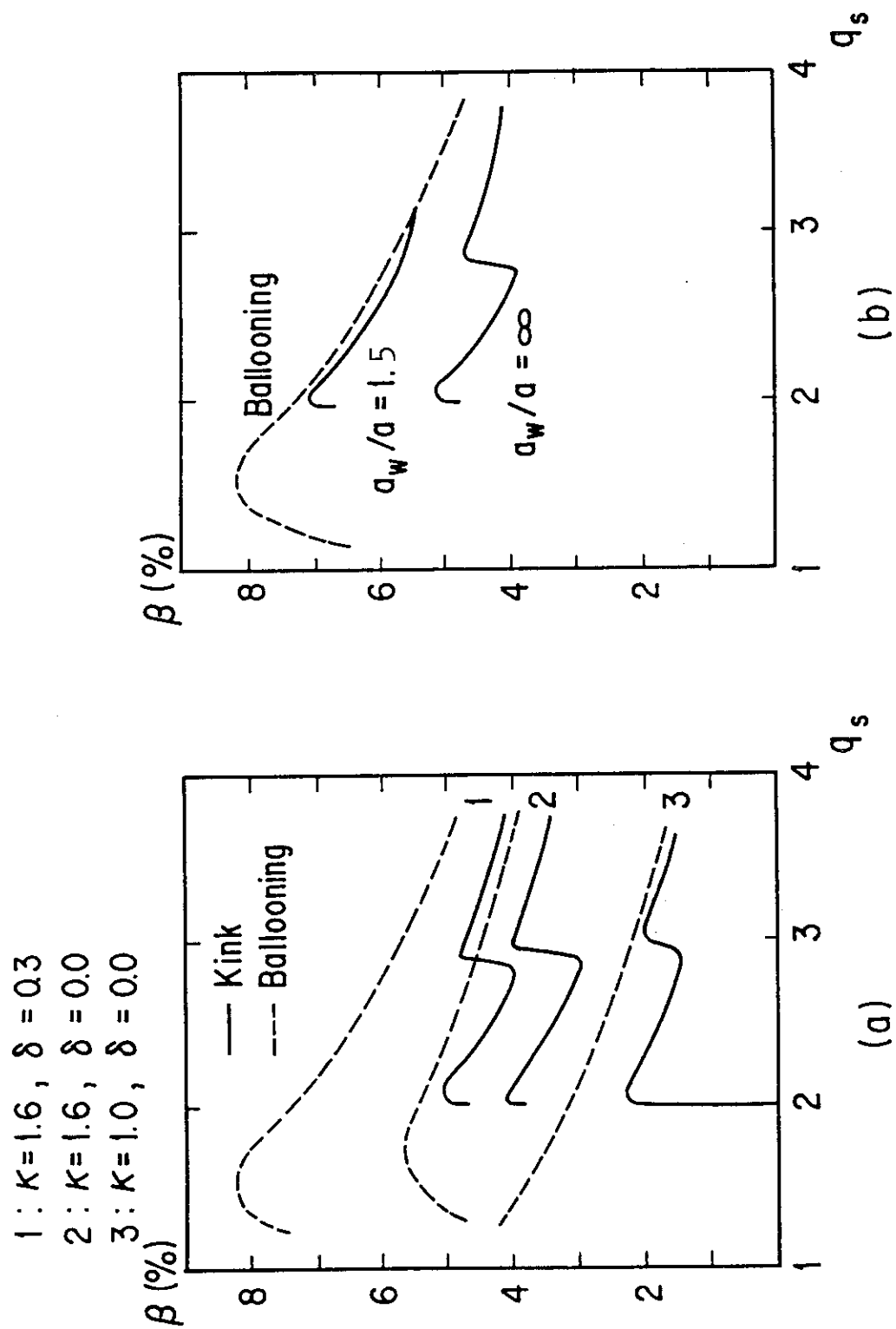


Fig.2.33 Beta limit due to $n=1$ external kink mode vs. q_s for (a) $a_w/a=\infty$ and (b) $a_w/a=1.5$, $a=3.37$ and $q_0=1$.

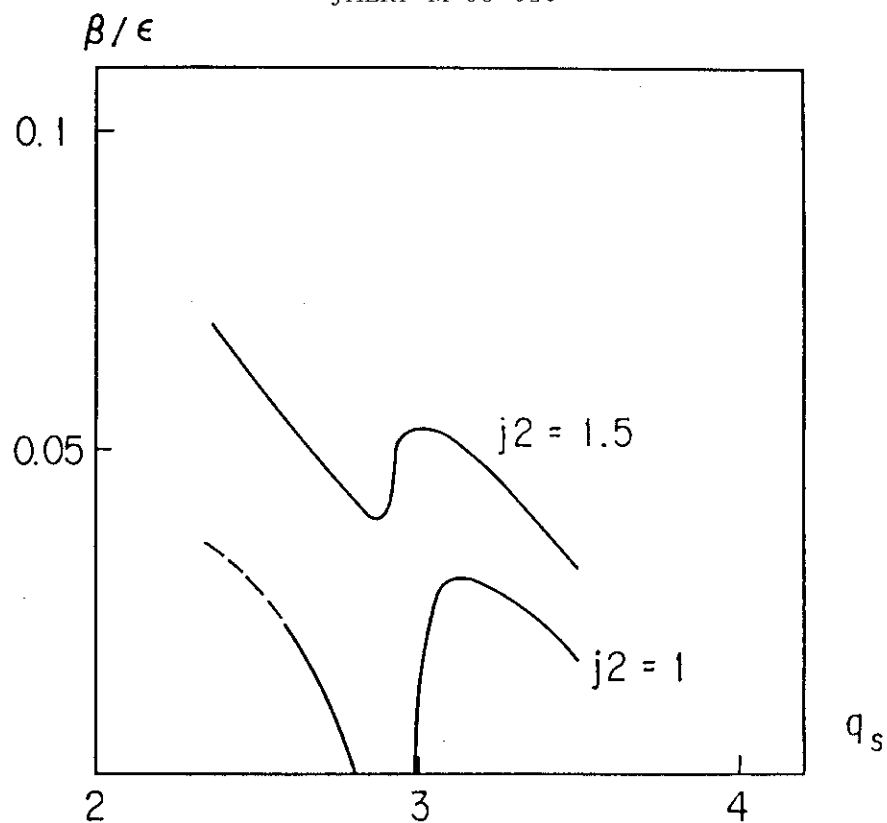


Fig.2.34 Beta limit β/ϵ ($\epsilon=1/4$), due to $n=1$ external kink mode for the averaged current density, $\langle j_z \rangle = j_0(1-\psi)^{j_2}$. The ratio, q_s/q_0 , is given by $q_s/q_0 = j_2 - 1$.

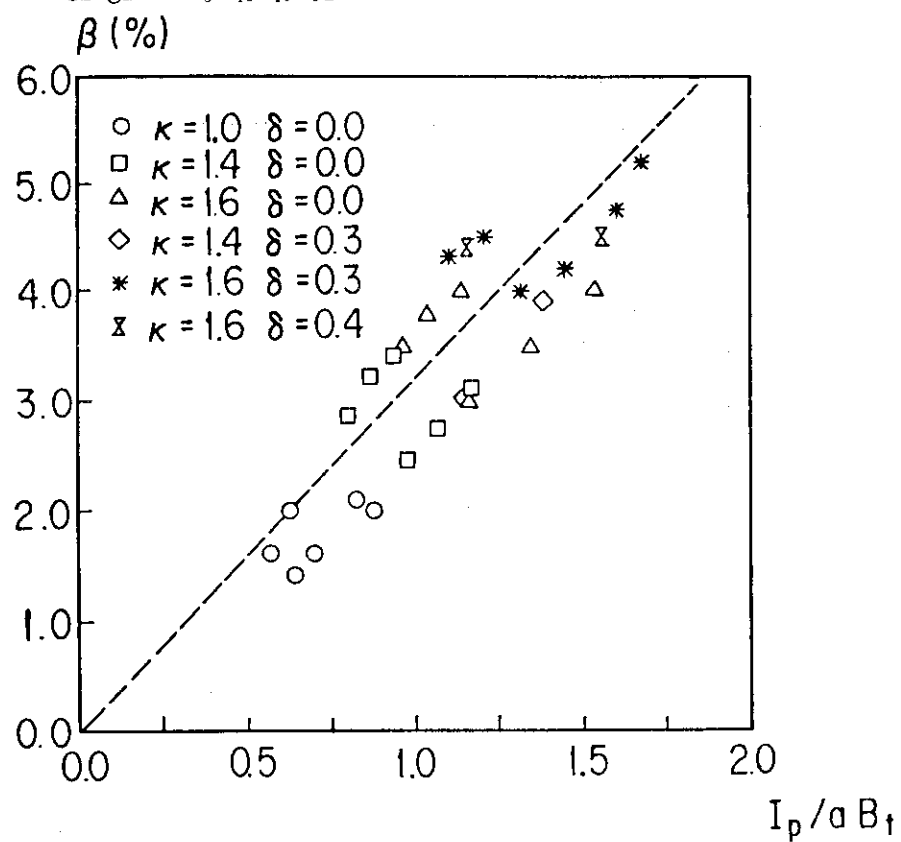


Fig.2.35 Beta limit due to $n=1$ external kink mode vs. I_N .

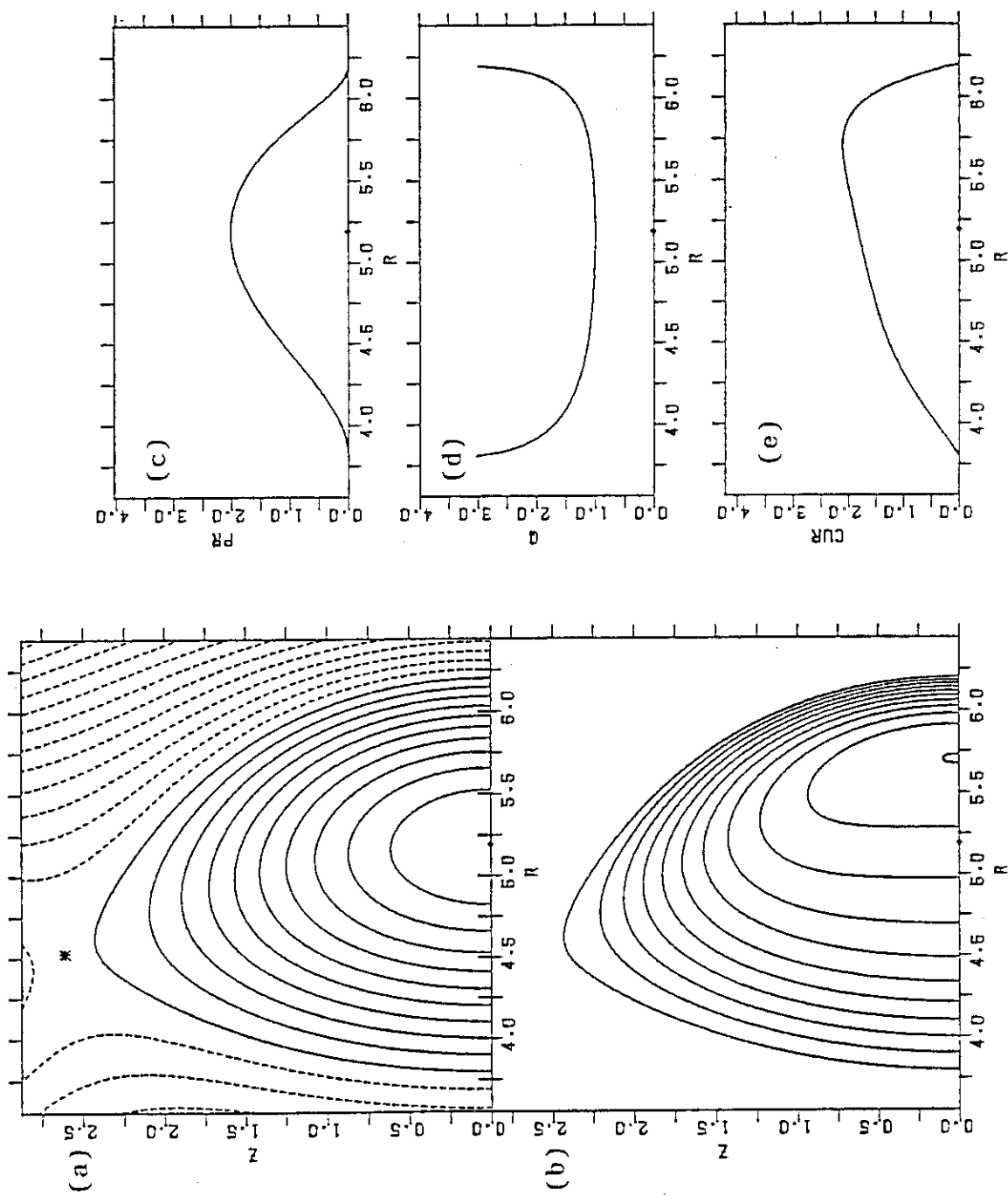


Fig. 3.1 Equilibrium for $q_0=1$, $q_s=3.0$, $A=4$, $\kappa=2.0$ and $\delta=0.3$: (a) flux surface (b) contour of toroidal current, (c) plasma pressure, (d) safety factor and (e) toroidal current density on the horizontal midplane.

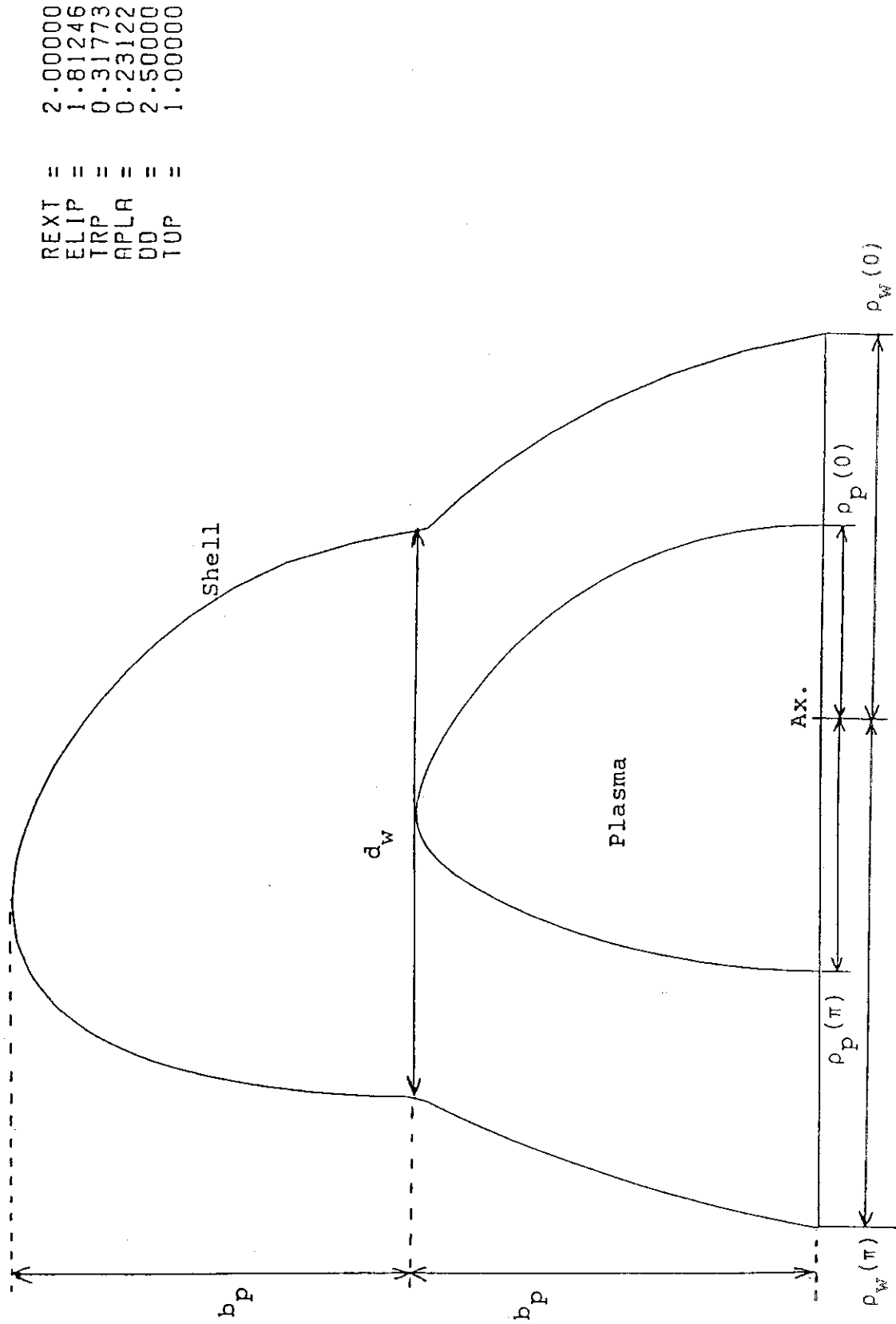
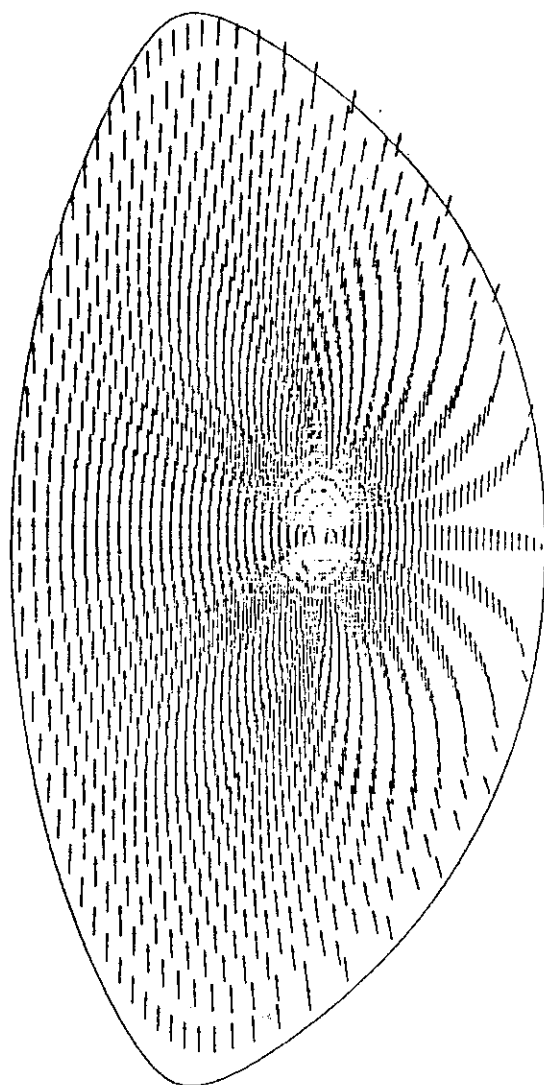


Fig. 3.2 Position of the conducting shell



JAERI TOKAI "ERATO-J" 87-04-09 PHI = 0
 N = 0.0 QAXIS = 1.0013 QSURF = 3.1936 REXT = INF
 A = 4.167 BETAP = 2.230 DISPLACEMENT

Fig. 3.3 Flow of the unstable modes for the case
 without a conducting shell

REXT	=	2.00000
ELIP	=	2.02615
TRP	=	0.31905
APLA	=	0.23113
DD	=	2.50000
TOP	=	1.00000

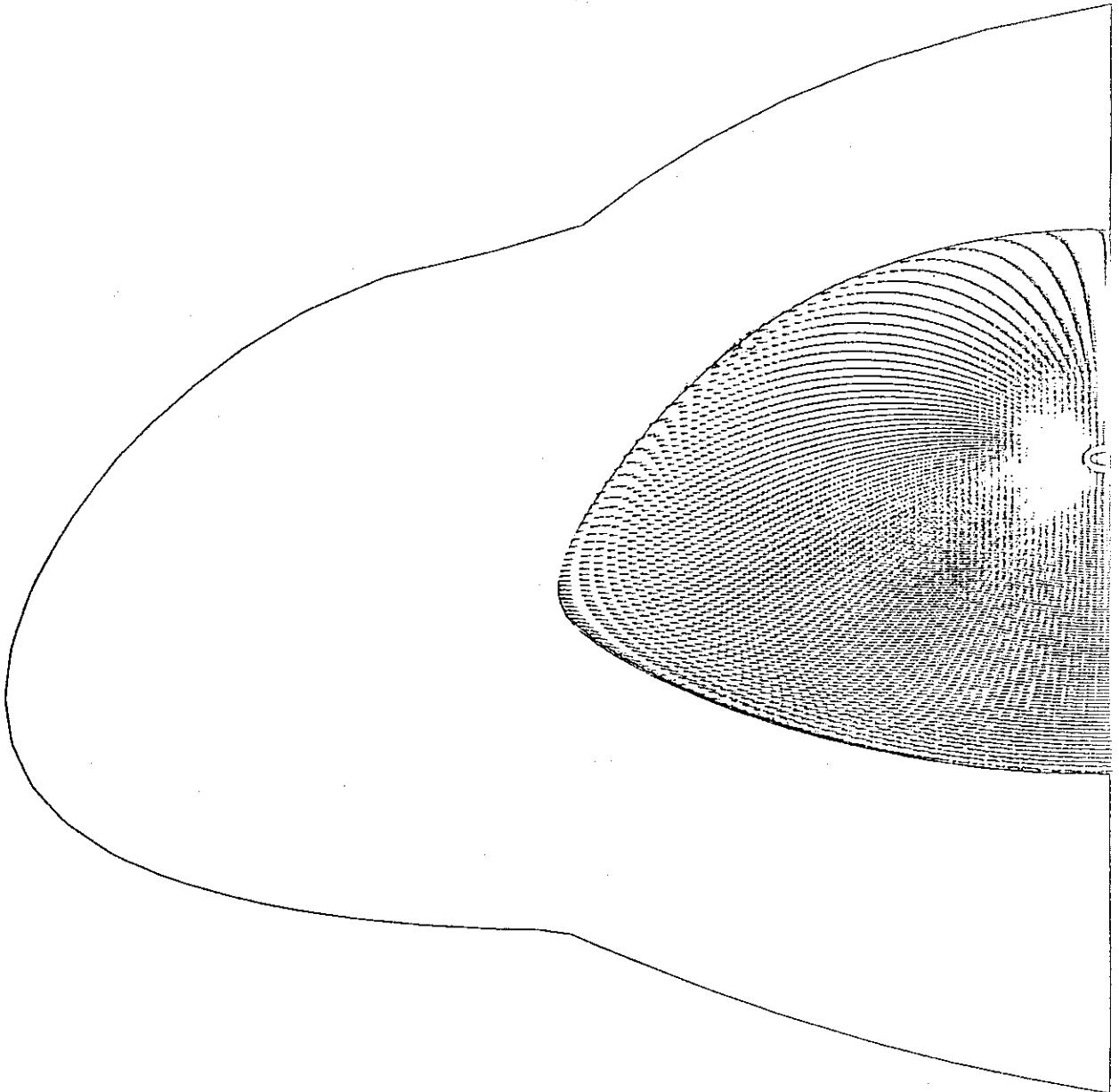


Fig. 3.4 Flow of the unstable modes for the case with conducting shell. The cut width is $d_w/a_p=2.5$.

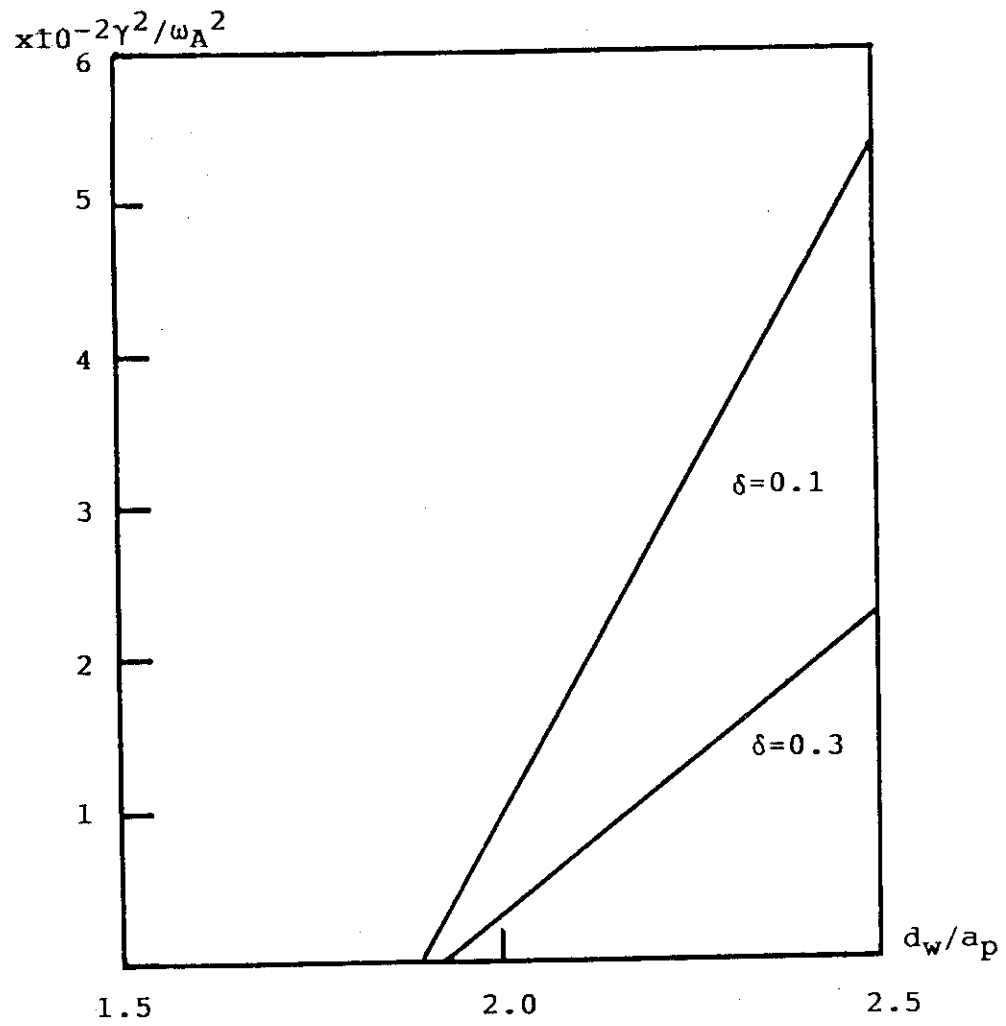


Fig. 3.5 The squared growth rate vs. d_w/a_p .